공학박사학위논문

Integrated Human Motion Sensors and Triboelectric Generator for Wearable Electronic System

사람동작 감지기들과 마찰전기 발전기를 통합해

구현한 입을 수 있는 전자기기 시스템

2015 년 1 월

서울대학교 대학원

화학생물공학부

정성묵

Abstract

Integrated Human Motion Sensors and Triboelectric Generator for Wearable Electronic System

Sungmook Jung

School of Chemical and Biological Engineering

The Graduate School

Seoul National University

Wearable electronics that can be worn on a user's body have received wide attention due to their applicable potential as a biomedical device, healthcare device, and human-machine interface. Significant progress has been made in this technology, but still, they solve three technical problems to function practically. The wearable device should be stretchable so the wearer do not feel discomfort on it and be smart so it automatically senses the various signals from the wearer then

exchanges the information through its external network. Among those signals, some are conscious signals to enter commands, and the others are unconscious signals inadvertently generated from the human body which could be used as a critical information for medical treatment. The wearable devices can figure out what the wearer needs and provide him/her with the proper service using those signals. Finally, the wearable devices should be able to continuously actuate in the extended period of time. However, it has a limit on its power capacitance because it is only permitted on the narrow area and the battery has to be thin for its wearability. In order to solve these issues, here we use the meaninglessly wasted friction energy which is generated on the human body to be converted into the electric power and then charges the battery to extend the actuation time. To prove the charged electricity is able to operate the wearable devices, we compose the integrated human motion sensors and energy devices for wearable electronic system.

This system is composed of stretchable power supply devices (triboelectric generator and supercapacitor or micro battery) interconnected with sensors, wireless units, and electronics (3-axis accelerometer, Bluetooth module, and microcontroller) through conductive carbon fibers on a jacket. Stretchable energy devices are worn on the human body (wrist or chest) and commercial devices are sewn on the chest region. The generated power from triboelectric generator during arm movements in walking or running are transferred via conductive threads to rectifiers and then energy storage unit. The charged unit supply power to pressure

sensor or fall detection sensors and electronics. The pressure sensor detects the conscious signal (press a certain buttons) and is used as human–machine interfaces for controlling machines wirelessly. The fall detection sensor detects the emergency state (the wearer's falling accident) and automatically sends the emergency signal (email) to the hospital. All of these sensors and energy devices are fabricated with fabric-like electrode, which had high stretchability and mechanical properties (e.g., stiffness) of fabrics. Thus, it could be easily stretched and worn on a wrist or integrated on clothes without causing any discomforts

Keywords: wearable electronics, pressure sensitive rubber, triboelectric generator, smart fabric, human- machine interface.

Student number: 2010-31328

Contents

List of Tables

List of Figures

Chapter 1. Introduction

1.1 Wearable technology

Technology has been developed to decrease the size of the electric devices from room size to palm size, fitting with the user's life style. They could be passive accessories and smart devices such as phone, watch and glasses.[1] We have used them as an internet access module, game player, MP3 player, or heath monitoring sensor. Recently, such technologies have become a huge part of the personal life for good or ill. Since people want smarter devices and more convenient life, wearable technology have attracted much attention as the future devices that can be worn on the user's body over an extended period of time. The term, "wearable", implies that the device is either supported directly on the human body or a piece of clothing and has an appropriate design enabling its prolonged use as a wearable accessory.[2] The features that distinguishes wearable devices from traditional portable devices are that they present closer to the user and constantly collect data from the user by sensing various signals such as mechanical inputs (pressure, strain, stretch, compression etc.), biomedical information (ECG, EMG, EEG, body temperature, heart pulse, glucose etc.), and environmental conditions (weather, humidity, UV intensity etc.). Furthermore, it can wirelessly connect to the other

electronic devices and operate them. These capabilities make the wearable devices into the essential units for the ubiquitous environment. Hence, many companies keep their eyes on the wearable technology-driven market and expect that the five categories of industries could adopt this technology.[3,4]

- **Fitness and Wellness** - Devices are used in monitoring human activity and emotions.
- **Healthcare and Medical** – Devices which had passed the FDA or equivalent approval are used in monitoring vital signs.
- **Industrial and Military** – Devices receive and transmit real-time data in military and/or industrial environments.
- **Infotainment (information + entertainment)** - Devices are used to receive and transmit real-time information for entertainment or enhanced lifestyle purposes.

As Figure 1.1 shows, many companies are interested in wearable electronics and planning to launch new projects. For example, smart glasses such as Google glass and heads up displays for gaming including Microsoft Kinect are commercialized, Samsung and Qualcomm launched new smart watches, and the continuous light-based heart rate monitoring is used in the sports market.

Figure 1.1 Five categories of wearable technology industries.[3,4]

The tremendous attention on the wearable devices constantly arises, and it is becoming blue market. An IHS research reports that the market for wearable devices have already reached a value of $10 billion in 2012 with predictions that this will quintuple by 2018.[3,4] They present the forecast with three scenarios such as downside, base and upside representing conservative, reasonable and optimistic viewpoints, respectively (Figure 1.2). The upcoming future will follow the one of the outlooks, depending on the degree of development in the wearable technology. In fact, many issues must be resolved for wearable technology to become a ubiquitous unit. The key factors that drive the market growth rate are wearability, smartness and long-term operation.[3,4]

• **Wearability** – Stretchability, flexibility, light weight, bio-compatibility, easy to put on and off, and maintaining range of motion.

• **Smartness** – The user experiences significantly enhanced continence while wear the device. Various integrated sensors with wireless connectivity and independent processing capability.

• **Long-term operation** – Optimized for low-power operation. Naturally harvest the energy and store it to the integrated wearable battery/supercapacitor.

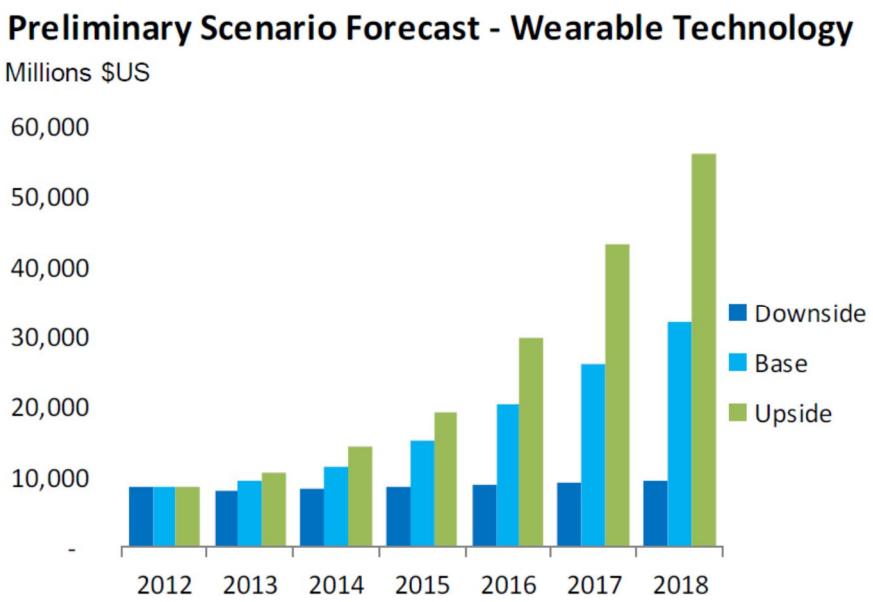

Figure 1.2 Overview of the World Market for Wearable Technology.[3]

1.2 Wearability

The human body consists of complex curvilinear surfaces where the wearable devices must cover conformally. Furthermore, skin and joints repeatedly stretch and compress. Thus, the essential properties of the wearable devices are flexibility and stretchability as clothes or skin. The research of mechanically flexible/stretchable electronics began ~ 20 years ago, and many successes have been achieved; several including displays are nearing commercial demand.[5-9] The research has dramatically developed, thus now, the devices could be bended, stretched, compressed, twisted, and deformed into complex curvilinear surfaces while maintaining their performance.[10] This success can be achieved in two different but complementary strategies. One is developing the new structural layouts of the conventional materials,[11] The other is synthesizing the new materials in the conventional layouts.[12] In elementary principles of mechanics, the flexural rigidity is $EH^3/12$, where E is the elastic modulus, and H is thickness. The former strategy is aimed to decrease the H value, and the latter is aimed specifically to decrease the E value.[13,14]

Structure for flexible/stretchable electronics

Special designs in structures and configurations are adopted to obtain flexibility and/or stretchability. As the formula shows, any material in sufficiently thin form, especially in nanoscale, is flexible. As Figure 1.3 shows, even a brittle

and rigid silicon wafer can be flexible when it have the nanoscale ribbons structure.[15] The ribbons with thicknesses of 100 nm experience the peak strains of only 0.0005% upon bending to radii of curvature of 1 cm. Furthermore, when the ribbons are mounted on the sheets of plastic with thicknesses of 20 mm, the strains (~0.1%) at the similar bend radii remain well below the fracture limits (~1%).[16] The mechanical neutral plane, which defines the position through the thickness of the structure where strains are zero for an arbitrarily small r, could improve the flexibility. As illustrate in Figure 1.4, when the electronic materials with high moduli is located on the geometric mid plane, the fracture strains of the materials are substantially lowered. The strain is less than ~ 0.1% when the silicon nanoribbons in this type of neutral mechanical plane is bended to radii of ~150 mm.[17,18,19]

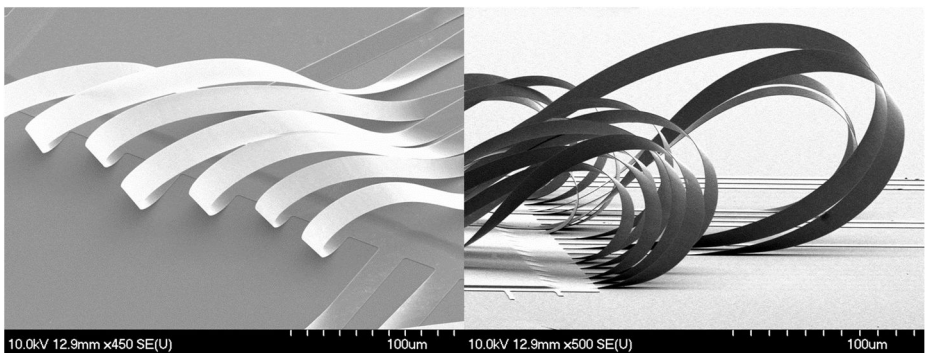

Figure 1.3 Ultra-thin nanoribbon Si.[15]

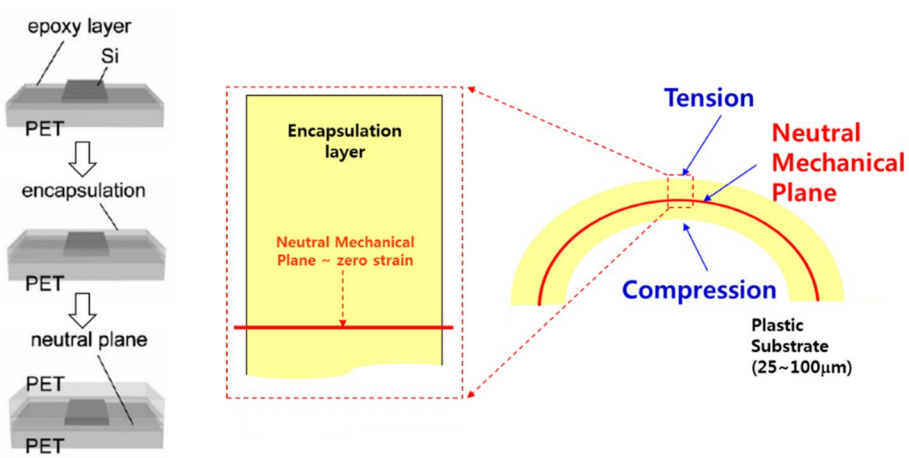

Figure 1.4 Illustration of fabrication of mechanical neutral plane.[17]

The structure design that consists of the island part and the interconnection part (micro scale arc-shaped bridge) on the elastomeric substrate makes rigid Si not only flexible but also stretchable and compressible. The interconnection part has the capacity to adsorb and withstand the strain by nonplanar movement while the island part subjects minimum harmful strain.[20] Figure 1.5 presents pairs of experimental images (left) and mechanics modeling of the associated strain distributions (right). The analytical and computational mechanics models is helpful to define the layouts that minimize strains in the semiconductors and other electronic materials.[13,14,21] Each of the structures has different components, and all of them use the elastomer (i.e., PDMS) as the substrate on which the ultrathin sheets of Si are bonded. As a result, the wavy structure shows the peak strains in the silicon can be 10 to 20 times smaller than the applied strains (Figure 1.5a). Then, such designs represent a stretchable form of silicon with the strain range of 10 to 20%, which is 10 to 20 times larger than the intrinsic fracture limits of the silicon. The island part with arc-shaped interconnection structure shows the strain in the bridge is reduced by 21 times at 10 % strain and 90 times at 100 % strain (Figure 1.5b). Under deformation, the buckled interconnection part can move to response to the applied strains (for strains less than the pre-strain), thereby providing a certain level of mechanical isolation for the islands. Also, it can move further by replacing the straight bridge interconnects with those with serpentine shapes, as in Figure 1.5c. This structure shows the most stable characteristics against the applied strains. For an applied strain $\varepsilon = 106\%$, the maximum strain in

the serpentine bridges is only 0.35% (i.e., a reduction of strain by 300x). The structure is adopted to produce wearable integrated system, and Figure 1.6 shows an example of it. Tactical sensor arrays were made at the mechanical neutral plain, thus it could be flexible and attached on three-dimensional surfaces (Figure 1.6a and b). The stretchable silicon circuit with the arc-shaped bridge is conformally integrated onto a model of a fingertip (Figure 1.6c).

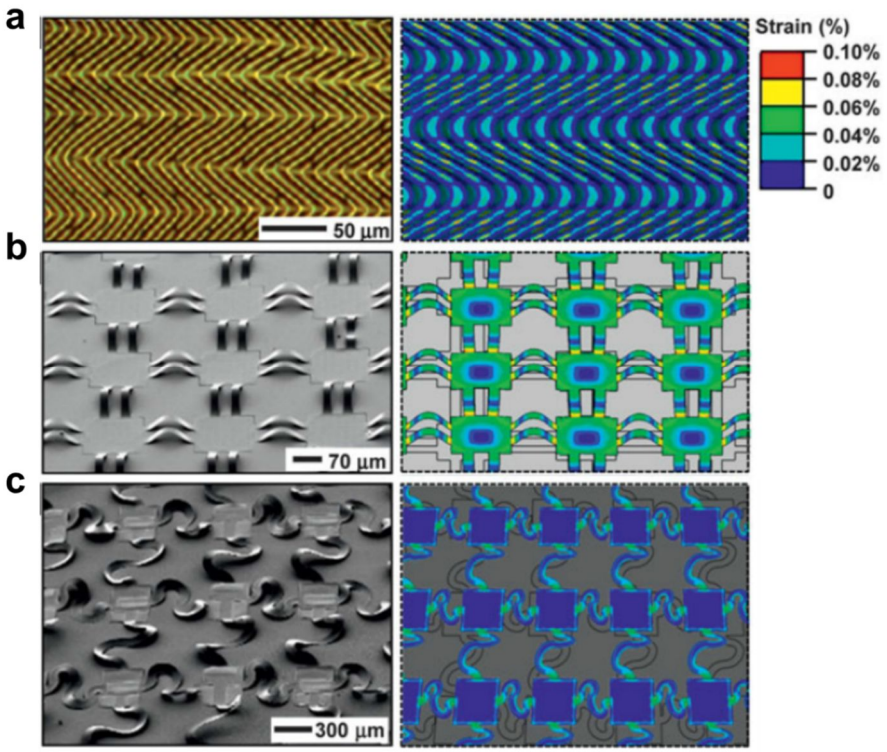

Figure 1.5 Experimental images (left) and mechanics modeling (right) of four different classes of structures with controlled buckling for high performance stretchable electronics. a) A silicon nanomembrane uniformly bonded to an elastomeric substrate adopts a "wavy," herringbone morphology. [13,14] b) A similar membrane structured into a mesh layout and selectively bonded only at the nodes takes a form that involves suspended, arc-shaped bridges (interconnects). This design offers enhanced ranges of stretchability compared to the case in (a). c) Advanced version of the structure in (b), where the interconnect bridges have non-coplanar serpentine shapes.[21]

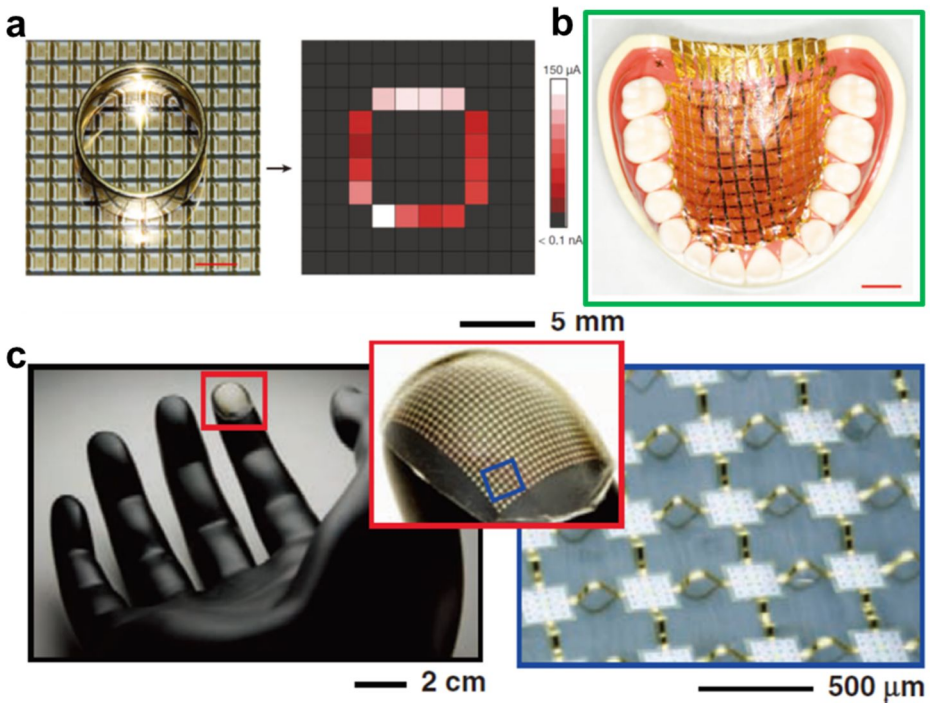

Figure 1.6 a) Top-view photograph (left) and corresponding drain current of a metallic ring placed on the sensing sheet (right). A difference of more than six orders of magnitude is observed in drain current between contacted and non-contacted pixels. Scale bar, 1 cm. b) Tactile sensor sheet tightly conforming to a model of the human upper jaw. Scale bar, 1 cm.[19] c) Stretchable silicon circuit with a mesh design, wrapped onto a model of a fingertip, shown at low (left), moderate (center) and high (right) magnification. The red (left) and blue (center) boxes indicate the regions of magnified views in the center and right, respectively. The image on the right was collected with an automated camera system that combines images at different focal depths to achieve a large depth of field.[21]

Material for stretchable electronics

An alternative strategy to obtain stretchability is to use the materials that are intrinsically stretchable. Traditionally, people have been made a composite rubber based on elastomer loaded with various fillers (carbon black, carbon nanotube (CNT), and metal nanowire).[22-24] Among the various fillers, carbon nanotubes (CNTs) have huge attention for its outstanding mechanical and electric properties. CNT is a nanometer-sized tube which has extremely high aspect ratio ($>10^6$), Young's modulus (0.2~1 TPa), tensile strength (13~126 GPa), electric current density (4×10^9 A/cm^2), and thermal conductivity (3,500 W/mK).[25-28] By virtue of the small size, hydrophobicity, and 1D structure, CNTs are easily dispersed in elastomer and make connection with each other.

A CNT-contained elastomer could be used as a stretchable interconnector and electrode. As shown in Figure 1.7, single wall CNTs (SWNTs) are grinded with an ionic liquid and a fluorinated copolymer to yield a black, paste-like conductive material.[23] Individual SWNTs form the tangled hair-like shape in these gels which could preserve highly conductive pathways for charge transport by reconfiguration responsible to the applied strain. This stretchable conductive rubber can be printed onto the sheets of PDMS and stretched biaxially by 70% without mechanical or electrical damages. Thus, it allows to construct electronic integrated circuits, which can be mounted anywhere including arbitrary curved surfaces and movable parts such as the joints of a robot's arm. (Figure 1.7).

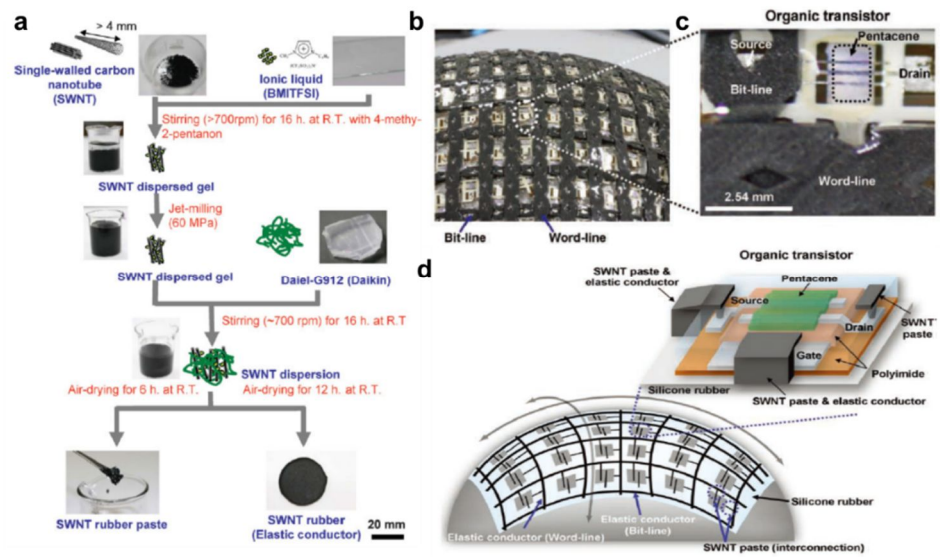

Figure 1.7 a) The manufacturing process for printable elastic conductors and pictures of the materials. Images of large-area stretchable active matrix comprising 19-by-37 printed organic transistors and wiring using the SWNT elastic conductor. The printed organic transistors function as active components, and the SWNT elastic conductor functions as word lines and bit lines for interconnection among the transistors. b) Image of the curved surface covered with the stretchable active matrix. c) Magnified image of one cell. A SWNT elastic conductor having a net-shaped structure was formed with a mechanical punching system and then coated with silicone rubbers. d) Schematic illustrations of the stretchable active matrix.[23]

Also, by adjusting the mixing ratio and component, the filler-contained elastomer could be used as a mechanical sensor for the change of pressure or strain (Figure 1.8).[22,24,29] The electrical behaviors of the filler-contained elastomer such as its conductivity and piezoresistance depend strongly on the filler concentration and morphology (e.g., particle size and structure) as well as the filler–filler and filler–matrix interactions.[22] The piezoresistive effect is foamed by the different compressibility between the filler and the elastomer, and the compressibility is strongly affected by the Young's modulus of each components. In other words, at a certain degree of the applied pressure, the elastomer with lower modulus are highly compressed than the filler, and their different deformation generates the stress between the individual filler units, cracking the electrical path of it. The further modulus gap between the filler and elastomer is the key issue of the sensitivity. Accordingly, we use CNTs and PDMS which has relatively low modulus. In Chapter 2, we mixed these components with the reverse-micelle solution to make the porous-structured pressure sensor which overcomes the limitation of modulus of solid structure. This resistive type sensor has advantages on its easy fabrication method, potential to mass production, high sensitivity, and stretchability. Furthermore, the printing method can be applied to fabricate the patterned sensor devices.

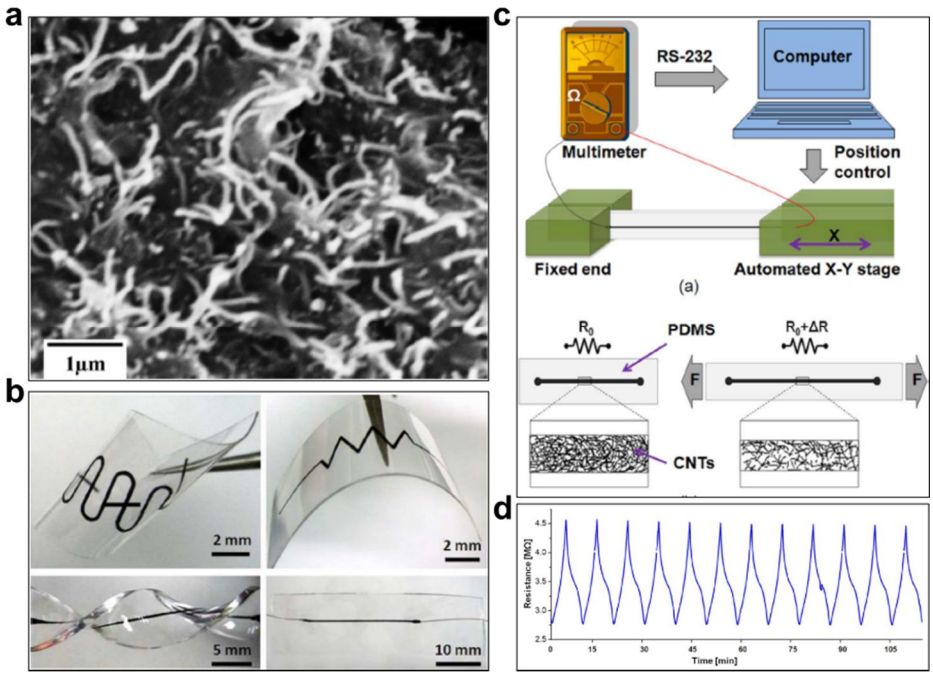

Figure 1.8 a) SEM image of a PDMS–MWCNTs composite. The cross section was obtained by fracturing sample in liquid nitrogen. b) PDMS–MWCNTs composite strain-sensing samples with different microstructure designs including serpentine, zigzag, and single-line patterns. Illustrated embedded nanocomposite patterns are around 250 μm wide, 50 μm thick, and a few centimeters in length. PDMS thin films were generally a few hundred micrometers in total thickness. c) Illustrations of strain-testing experiments. (top) Experimental setup that allows simultaneous recording of strain and resistance values on PC. (bottom) Schematic diagram showing the interconnection and spacing change of CNTs when nanocomposite is stretched under tensile strain. d) Measured electrical resistance of nanocomposite (sample B) over time under cyclic loadings of tensile strain. During each cycle, strain increases linearly from 0% to 42% in 4.5 min, and 12 testing cycles are extracted to reveal the repeatability of resistive response.[29]

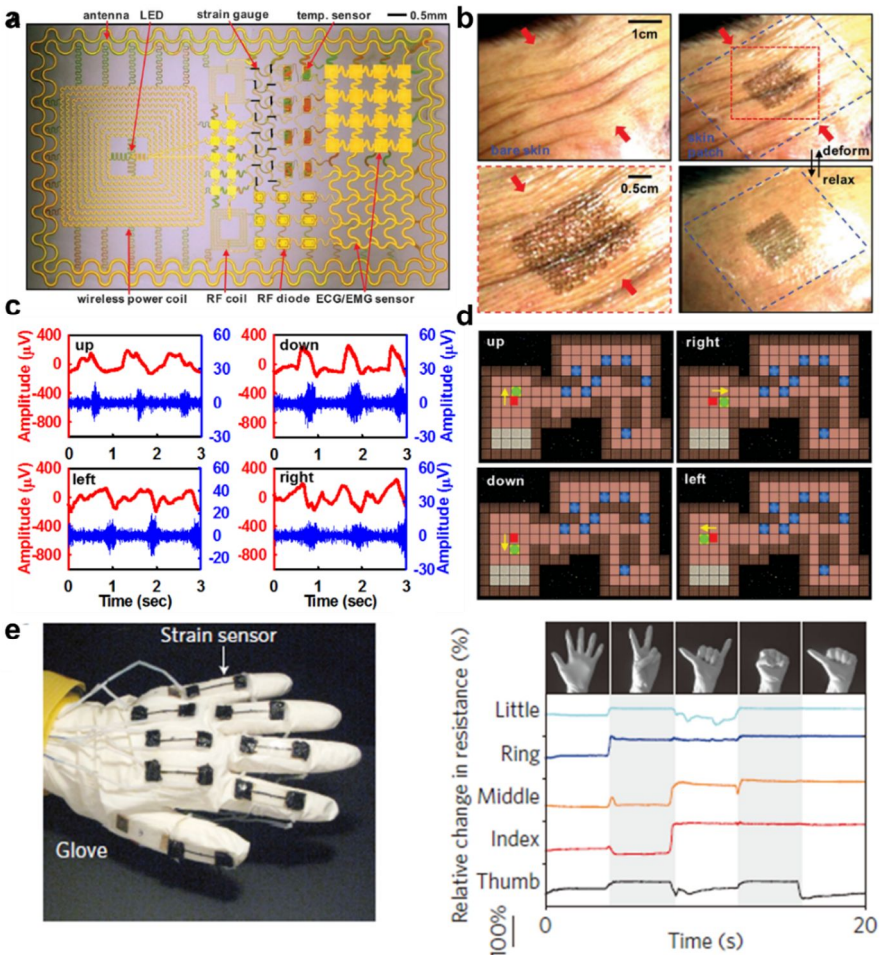

Figure 1.9 a) Image of a demonstration platform for multifunctional electronics with physical properties matched to the epidermis. b) Skin of the forehead before (top left) and after the mounting of a representative FS-EES, at various magnifications and states of deformation. c) EES EMG measurement from the neck for four different words, "up", "down", "left" and "right". Red and blue plots correspond to raw and high-pass filtered data, respectively.[30] d) Simulated video game control by pattern recognition on EMG data. e) Photographs of a bandage strain sensor (left). Relative changes in resistance versus time for data glove configurations.[31]

1.3 Smartness

The reason people try to make the wearable devices is to enhance the quality of life or the convenience of life.[1-3] Accordingly, the wearable devices have to be smart, thereby they provide proper supports to the wearers in various situations. For examples, the device could automatically call the ambulance when the wearer gets an accident, control the external devices such as an air conditioner, TV, and car from the wearer's voice or pushing the button of the wearing device. For these supports, the device should have a outstanding sensitivity for various signals, independent data processing capability, and wireless connectivity.[3] The thing that determine the value of the wearable devices and distinguish the wearable devices from other smart devices is the sensing part which is conformally attached on the body, thus it could get the information accessible only from the human body.[1] The information is collected from both the conscious signals and the unconscious signals.

The conscious signals are generated by the will of the wearer. He/she recognizes the existence of the device and makes signals to enter commands to it by speaking or pushing the buttons. Furthermore, the movement of vocal cords can be used for a spokesmachine to help the wearer, who is unable to speak, communicate with other people. Likewise, the movement of fingers can be used as a manipulator for augmented reality-based programs (Figure 1.9).[30,31] Those various signals are detected by the sensors; the pressure and the strain sensors. In chapter 2, we fabricated the wearable pressure sensor and strain sensor for human-

machine interface. These sensors are the resistive type and have a simple working principle, i.e. the resistance increases when the pressure was applied, and it can be measured by simple read-out unit.[22] Thereby, the proposed wearable sensors fulfill the wearable purpose and are used as the human–machine interfaces for controlling machines wirelessly.

The unconscious signals are the outputs that naturally generated by daily activities. There are three kinds of information including the mechanical information (pressure, strain, stretching, compression, walking distance, the degree of human activity, etc.), bio-medical information (ECG, EMG, EEG, body temperature, heart pulse, blood sugar level, etc.), and environmental conditions (weather, humidity, UV intensity etc.). Those information received wide attentions due to their strong applicability in the biomedical device field. Numerous applications have been reported including wireless contact-lens type tear glucose sensor[32], wireless sweat sensor[33], and integrated epidermal electronic systems composed of sensors for electrophysiological signals, electrocardiograms and electromyograms along with temperature and mechanical strain sensors[34]. Due to the special properties, i.e. operational and interactional constancy, of the wearable sensor, it could collect the long-term internal biomedical signals and notice the real-time conditions of the patient to the doctor (Figure 1.10).[35] In this research, we measured the degree of human activity by a newly attempted method (Chapter 3) and demonstrated the wearable fall detection system by adding the 3-axis accelerometer and the wireless communication module that has the independent

processing capability. The electricity generated from the TEG charges the battery while the battery simultaneously powers the accelerometer detecting the falling of the wearer (e.g., the senior citizen or patient). When the detected signal is identified as the fall of the patient, it automatically sends the e-mail to the doctor. (Chapter 4)

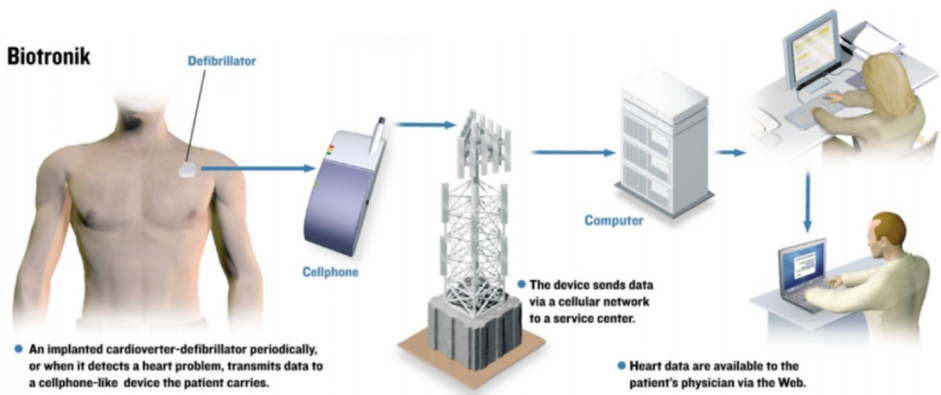

Figure 1.10 Schematic illustration of smart health care system.[35]

1.4 Long-term operation: Power source.

Electronic devices have been progressed to accomplish their small size, light weight and flexibility for their application to wearable mobile devices. As early mentioned, wearable devices have been developed and investigated by many research groups, and their meaningful measurements and significant demonstrations for the future wearable system were achieved. However, most of current studies were conducted in the setting with conventional power sources providing the electrical power to the wearable system through the electrical cords. Autonomous power generation within the wearable electronics possibly releases the system from its restraint of being wired with its external power sources. To be wearable, however, battery should be small and thin, which is critical to its capacity. Thus it would have short actuation time. Continuous charging of the battery by integrating it with the energy harvesting devices can be one of the solutions for this issue[36,37].

Triboelectric Generator (TEG) chosen for the internal materials of the systems can be a strong candidate for the autonomous power generation due to its light weight, flexibility and biocompatibility. TEG generates electrical energy from friction. An average-sized human body stores as much energy as a 1000-kg battery, and about 25% of the energy can be converted into the mechanical energy[38-41], which can make friction. This unlabored energy from the unconscious daily activity of human body is enough to generate ample electricity to operate the

wearable devices through the TEG. Wang et al. demonstrated that TEGs convert the energy of mechanical friction to electrical one.[42] Many types of mechanical motions were investigated for the power generation such as contact/releasing, sliding and rotation. Basically, electrical power generation in TEG is caused by the coupling effect of the contact electrification and the electrostatic induction.

The contact electrification, also known as triboelectric charging, is a process that occurs when two different materials are in contact. The material with the stronger electron affinity steals electrons, and the surface will be negatively charged after they are separated while the surface of other material will have an equal amount of positive charge. Figure 1.11 represents the mechanisms of the triboelectric charging.[43,44] The potential of electrons expressed as the workfunction (WF) have a strong influence on the polarity. As shown in Figure 1.12, the polarity has been described empirically as the triboelectric series, and the order of the series matches well with the order of WF. Additionally, there are many other factors to determine the polarity (e.g. electronic properties, hydrophility, surface roughness, surface stress/strain, impurities and other properties). When a material near the bottom of the series touches a material near the opposite side of the series, it will gain more negative charges. The further they are apart, the more charges are taken.[42] In this study, we used the surface modifier (polyethylenimine ethoxylated) to reduce the workfunction of a material near the top of the series. Thereby, two materials of the triboelectric generator could obtain further gap between them and show improved electric power generation performance.

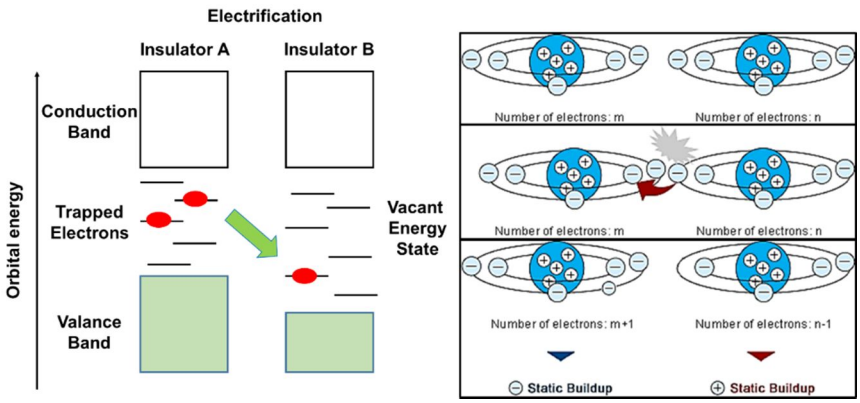

Figure 1.11 Mechanism of tribo electrification.[43,44]

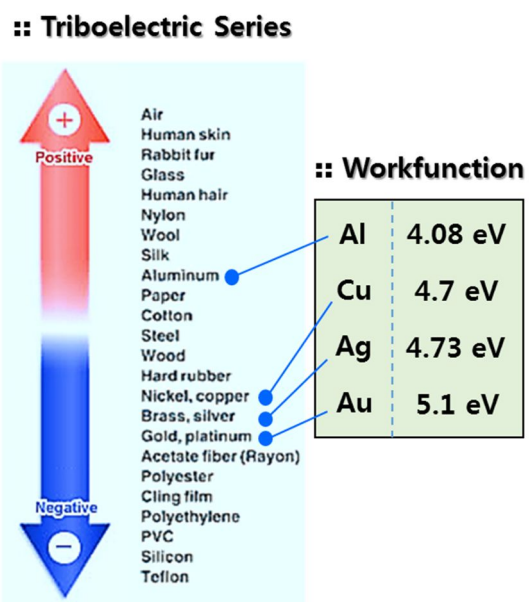

Figure 1.12 Triboelectric series (left) and workfunction series (right).[42]

TEG uses the electrified insulating materials which maintain its charges after friction. By repetitive contact/separation of two charged surfaces, the periodic change of the potential difference is induced on the inner layers of the materials (electrodes) which connect each other. Figure 1.13 schematically depicts the sequence of the operation in relation to the vertical friction. In the initial state, no charge has yet been induced, and so there is zero electric potential (EP) difference between the top and the bottom TEG surface. The two TEGs are then brought to contact with each other, and their surface charges are transferred due to the triboelectric effect. At this state, the net EP change ($-\sigma + +\sigma$) is zero, but when the TEGs are separated, the mechanical contact between the surfaces is effectively eliminated, and it creates an EP difference between the two electrodes. This causes an electrical current to flow until each layer reaches the electrical equilibrium. Finally, the TEGs are again brought to contact with others, generating an EP difference between the two electrodes and creating a current flow until a new electrical equilibrium is reached (i.e., the return to the initial state).[45-48] To use the TEG as a wearable electrical generator, researchers integrated the existing TEGs which consists with metals and polymers on the cloth.[49] Those materials have different mechanical properties than clothes, so it is not comfortable while wearing.

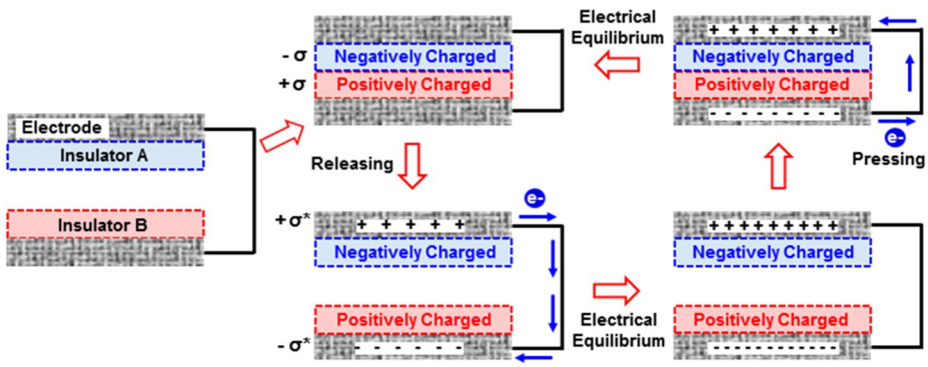

Figure 1.13 The working process of TEG through contact/release.[48]

Here, we present a fully-integrated and wearable energy supply system loaded with a triboelectric power generator and a battery/supercapacitor. They are fabricated on the conductive nylon or the carbon fabric which is compatible with other commercial fabrics. The fabric-based devices maintain the mechanical properties (e.g., stiffness, low modulus and stretchability) of the fabric, so they fully function on clothes without disharmony. In chapter 3, we modified the structure of TEG that can generate electrical charge from not only the vertical friction (contact/separation) but also the horizontal friction (rubbing). In chapter 4, we fabricated the TEG with improved performance by using surface modification which reduces the WF of the material. The removal of electrical cords by integrating a wearable power supply in the wearable devices suggests a possible application of this wearable and self-sustainable monitoring system in biomedicine.

References

[1] M. Billinghurst, T. Starner, *IEEE* **1999**, Jan, 57

[2] C. Glaros, D. I. Fotiadis, *StudFuzz* **2005**, 184, 237-264.

[3] IHS whitepaper, "Wearable technology – Market Assessment", *IHS electronics & Media* **1999**, Sep

[4] 김대건, "웨어러블 디바이스 동향과 시사점", 25 1-26, *방송통신정책* **2013**, 25, 1-26

[5] F. Garnier, R. Hajlaoui, A. Yassar, P. Srivastava, *Science* **1994**, 265, 1684

[6] Z. N. Bao, Y. Feng, A. Dodabalapur, V. R. Raju, A. J. Lovinger, *Chem. Mater.* **1998**, 9, 1299

[7] G. H. Gelinck, H. E. A. Huitema, E. V. Veenendaal, *Nat. Mat.* **2004**, 3, 106

[8] P. F. Baude, D. A. Ender, M. A. Haase, T. W. Kelley, D. V. Muyres, S. D. Theiss, *Appl. Phys. Lett* **2003**, 82, 3964.

[9] Cantatore, T. C. T. Geuns, G. H. Gelinck, E. Veenendaal, A. F. A. Gruijthuijsen, L. Schrijnemakers, S. Drews, D. M. Leeuw, *IEEE J. Solid-State Circuits* **2007**, 42, 84.

[10] J. A. Rogers, T. Someya, Y. Huang, *Science* **2010**, 327, 1603

[11] D.-H. Kim, J. Xiao, J. Song, Y. Huang, J. A. Rogers, *Adv. Mat* **2010**, 22, 2108

[12] T. Sekitani, T. Someya, *Adv. Mat* **2010**, 22, 2228

[13] H. Jiang, D.-Y. Khang, J. Song, Y. Sun, Y. Huang, J.A. Rogers, *PNAS. Mat* **2007**, 104, 15607

[14] J, Song, J. Jiang, W.M. Choi, D.Y. Khang, Y. Huang, J.A Rogers, *J. Appl. Phys*. **2008**, 103, 014303.

[15] D.-H. Kim, N. Lu, Y. Huang, J.A Rogers, *MRS. Bull* **2012**, 37, 226

[16] A. J. Baca, J.-H. Ahn, Y. Sun, M. A. Meitl, E. Menard, H.-S. Kim, W. M. Choi, D.-H. Kim, Y. Huang, J. A. Rogers, *Angew. Chem. Int. Ed.* **2008**, 47, 2

[17] S.-I. Parket, J.-H. Ahn, X. Feng, S. Wang, Y. Huang, J.A. Rogers, *Adv. Funct. Mater.* **2008**, 18, 2673.

[18] D.-H. Kim, J.-H. Ahn, W.M. Choi, H.-S. Kim, T.-H. Kim, J. Song, Y.Y. Huang, Z. Liu, J. A. Rogers, *Science* **2008**, 320, 507

[19] M. Kaltenbrunner, T. Sekitani, J. Reeder, T. Yokota, K. Kuribara, T.Tokuhara1, M. Drack, R. Schwodiauer, I. Graz, S. Bauer-Gogonea, S. Bauer, T. Someya, *Nature* **2013**, 499, 458

[20] D.-Y. Khang, H. Jiang, Y. Huang, J. A. Rogers, *Science* **2006**, 311, 208

[21] D-H. Kim, Y-S. Kim, J. Wu, Z. Liu, J. Song, H-S. Kim, Y.Y. Huang, K-C. Hwang, J.A. Rogers, *Adv. Mat.* **2009**, 21, 3703

[22] N. Lu, C. Lu, S. Yang, J. A. Rogers, *Adv. Funct. Mater.* **2012**, 22, 4044

[23] T. Sekitani, Y. Noguchi, K. Hata, T. Fukushima, T. Aida, T. Someya, *Science* **2008**, 321, 1468

[24] S. Gong, W. Schwalb, Y. Wang, Y. Chen, Y. Tang, J. Si, B. Shirinzadeh, W. Cheng, *Nat. Commun* **2013**, 5, 3132

[25] M.F.L.D. Volder, S.H. Tawfick, R.H. Baughman, A.J. Hart, *Science* **2013**, 339, 535

[26] B. Peng, M. Locascio, P. Zapol, S. Li, S.L. Mielke, G.C. SCHATZ, H.D. Espinosa, *Nat. Nanotech.* **2008**, 3, 626

[27] B.Q. Wei, R. Vajtai, P.M. Ajayan, *Appl. Phys. Lett* **2001**, 79, 1172

[28] E. Pop, D. Mann, Q. Wang, K. Goodson, H. Dai, *Nano Lett.* **2006**, 6, 96

[29] C.-X. Liu, J.-W. Choi, *IEEE Trans.Nanotechnol* **2010**, 9, 590

[30] D.-H. Kim, N. Lu, R. Ma, Y.-S. Kim, R.-H. Kim, S. Wang, J. Wu, S. M. Won, H. Tao, A. Islam, K. J. Yu, T. Kim, R. Chowdhury, M. Ying, L. Xu, M. Li, H.-J. Chung, H. Keum, M. McCormick, P. Liu, Y.-W. Zhang, F. G. Omenetto, Y. Huang, T. Coleman, J. A. Rogers, *Science* **2011**, 333, 838.

[31] T. Yamada, Y. Hayamizu, Y. Yamamoto, Y. Yomogida, A. Izadi-Najafabadi, D. N. Futaba, K. Hata, *Nat. Nanotech* **2011**, 6, 296.

[32] L.Y. Chen, B.C. Tee, A.L. Chortos, G. Schwartz, V. Tse, J.L. D, H.S. Wong, M.V. McConnell, Z. Bao, *Nat Commun* **2014**, 5, 5028;

[33] X. Huang, Y. Liu, K. Chen, W.J. Shin, C.J. Lu, G.W. Kong, D. Patnaik, S.H. Lee, J.F. Cortes, J.A. Rogers, *Small* **2014**, 10, 3083.

[34] W.H. Yeo, Y.S. Kim, J. Lee, A. Ameen, L. Shi, M. Li, S. Wang, R. Ma, S.H. Jin, Z. Kang, Y. Huang, J.A. Rogers, *Adv Mater* **2013**, 25, 2773.

[35] P.H. Ross, *IEEE Spectrum* **2004**, Dec, 26

[36] X. Xue, P. Deng, B. He, Y. Nie, L. Xing, Y. Zhang, Z.L. Wang, *Advanced Energy Materials* **2014**, 4, 1301329.

[37] S. Wang, Z.-H. Lin, S. Niu, L. Lin, Y. Xie, K.C. Pradel, Z.L. Wang, *ACS Nano* **2013**, 7, 11263.

[38] G.A. Brooks, T.D. Fahey, K.M. Baldwin, "Exercise Physiology: Human Bioenergetics and Its Applications", *McGraw-Hill*, **2005**, 4

[39] T. Starner, *IBM Syst. J.* **1996**, 35, 618

[40] R. Margaria, *Int. Z. Angew. Physiol*. **1968**, 25, 339

[41] J.M. Donelan, Q.Li, V. Naing, J.A. Hoffer, D.J. Weber, A.D. Kuo, *Science* **2008**, 319, 807

[42] Z.L. Wang, *ACS Nano* **2013**, 7, 9533

[43] http://www.csupomona.edu/~kmforward/research.html

[44] http://www.keyence.com/ss/products/static/resource/feature/index.jsp

[45] C. Zhang, W. Tang, C. Han, F. Fan, Z. L. Wang, *Adv. Mater.* **2014**, 26, 3580

[46] J. Chen, G. Zhu, W. Yang, Q. Jing, P. Bai, Y. Yang, T.-C. Hou, Z.L. Wang, *Adv. Mater.* **2013**, 25, 6094.

[47] G. Zhu, C. Pan, W. Guo, C.-Y. Chen, Y. Zhou, R. Yu, Z.L. Wang, *Nano Lett.* **2013**, 12, 4960.

[48] S. Jung, J. Lee, T. Hyeon, M. Lee, D.-H. Kim, *Adv. Mater.* **2014**, 26, 6329

[49] H. Zhang, Y. Yang, T-C. Hou, Y. Su, C. Hu, Z.L. Wang, *Nano energy* **2013**, 2, 1019

Chapter 2. Reverse-micelle-induced porous pressure sensitive rubber for wearable human-machine interface

2.1 Introduction

Electronic devices responsive to external mechanical deformations, i.e. mechanical sensors, have attracted much attention for applications to replicating the human skin,[1-7] and monitoring human body motions through wearable forms of electronics.[8-15] The sensitivity of mechanical sensors (e.g. pressure sensors and strain gauges) is one of the most important performance factors for better emulating human skin and more precisely capturing human motions. Using transistors to amplify signals is an effective method of doing these.[4] Another approach for achieving high sensitivity is to measure changes in the capacitance[1,2] instead of changes in the resistance[5-12] or to use specially designed inter-locking structures.[13] However, these approaches generally require complicated micro-fabrications and micro-structures.

Resistive-type mechanical sensors work based on a simple principle; i.e. measuring the change in the resistance of materials. Pressure-sensitive rubbers (PSRs), typically composites of elastomers and conductive fillers, such as carbon black and carbon nanotubes, are materials widely used to fabricate flexible resistive-type mechanical sensors.[5-12] Since they only require two components (i.e. a piezoresistive material and an electrode) to detect mechanical deformation, the device structure and fabrication process are relatively simple. Owing to their elastomeric property, PSRs are compatible with flexible and stretchable substrates and can be easily integrated with soft curvilinear surfaces including human bodies[8,10-12] and deformable surgical tools.[16,17] However, conventional PSR-based sensors often show poor sensitivity.

One approach to increasing the sensitivity is to introduce porous structures into piezoresistive materials. The change in the resistance of PSR-based mechanical sensors with a specific applied force depends on the deformability of the PSR, which is related to its Young's modulus. Sponge-like structures can be used to increase the deformability (or decrease the modulus).[18-21] For example, conductive polymers containing hollow-spheres,[18] porous carbon nanotube sponges,[19] metal-polymer hybrid nanocable sponges,[20] and gold film-polyurethane sponges[21] show enhanced sensitivity for detecting mechanical deformation. However, difficulties and complexities in controlling pore morphology and in designing patterned arrays of devices still remain. Hence, we used reverse micelles to develop a simple method of introducing pores into

conventional PSRs. The all-solution-based method is compatible with low-cost, large-scale manufacturing. Furthermore, the morphology, pore characteristics, and system modulus of PSRs can be readily controlled. The porous structure can be formed in the nozzle-jet-printed PSR line pattern and in the large-area PSR film. The wearable porous PSR (PPSR) pressure sensors and strain gauges can be conformally integrated with the skin owing to the low modulus of the PPSR. The proposed wearable sensors were used as human-machine interfaces (HMIs) for controlling machines wirelessly.

* The contents of this chapter was published on Advanced materials (2014, 26, 4825-4830)

2.2 Experimental Section

Preparation of black gel-like mixture: RMS was prepared by stirring 20 mL octane (98%, Sigma Aldrich, USA), 2 g emulsifier (Polyoxyethylene 5 nonylphenylether, branched, Igepal CO-520, Mn: 441, Sigma Aldrich, USA) and 10 µl DI water over 30 min.[22] Then, 0.1 g MWNTs (HANOS CM-250, Hanwha Nanotech, South Korea) and 9 g PDMS (30:1 mixture of prepolymer:curing agent; Sylgard 184, Dow Corning, USA) were mixed with 0~8 mL RMS. The blended black gel-like mixture was subjected to the ultra-sonication and stirring for 30 min each.

Film formation and patterning methods: For the pressure sensitive film formation, the black gel-like PPSR was poured into and filled a flat shallow enclosed template. Then the filled template was covered by a glass. By covering the black gel-like PPSR during the heat treatment, the uniformity of pores could be increased. For the patterning of PPSR, a 6 mL syringe was filled with well-mixed black gel-like PPSR and was installed to the nozzle jet printing system (eNano Printer, Enjet, South Korea). The gel-like PPSR was ejected from a nozzle on the target substrate. The custom-made software controled the movement of nozzle by following pre-loaded computer-aided designs (CADs). Patterned gel-like PPSR surrounded by dams and silicone oil (Shin-Etsu silicone, Japan) was poured into dams to cover the pattern. Finally, the heat treatment was conducted in the oven

and the silicone oil was removed. Then, the sample was repeatedly washed with organic solvents (isopropyl alcohol, Samchun, South Korea) and DI water.

Preparation of the pressure sensitive fabric and the skin-mountable PPSR sensors: For the pressure sensitive fabric, the PPSR film was sandwiched by two commercial conductive carbon fabrics (W0S1002, CeTech, Japan). To make conformal contact between the PPSR film and carbon fabric, a custom-made binder (conductive rubber paste) was used. The good adhesion between the PPSR film and carbon fabric electrode avoided mechanical failure at the junction even under multiple deformations of fabricated pressure sensitive fabric. The binder was prepared by mixing 9 g PDMS (30:1 composition) and 0.2 g MWNTs (Figure 4a). For the skin-mountable sensors, PPSR was patterned on a commercial elastomeric patch (Medifoam, Ildong, South Korea) by using the nozzle jet printing. Carbon fibers (Panex30, Zoltek, USA) were used to wire devices to external data acquisition circuits (Figures 4a and b).

Detailed procedures of the heat treatment and its effect on the porous structure: The primary purpose of the heat treatment is to solidify PDMS. Reverse micelles also gain certain thermal energy during the heat treatment, which makes reverse micelles migrate in the media. During the migration, reverse micelles have the higher probability of collision with other micelles as the moving distance increases. And the frequent collisions makes micelles merge into larger micelles (or bubbles). In the heat treatment process, the temperature was raised step by step. At each step, enough time was given for PDMS to become viscous enough before the

next temperature step. The heat treatment can be classified into three temperature ranges; low (55°C), near the boiling point (BP), and over the BP of the solvent. First, black gel-like solution was heated at 55°C for 12 hrs for the soft curing at the oven. In this step, the thermal energy makes the reverse micelles migrate and merge, while PDMS is slowly cross-linked, therefore PDMS becomes highly viscous liquid with bubbles which are filled with RMS. During the PDMS solidification, the size of the bubbles grows up (Figure 1e, bottom). After this step, the temperature was raised slowly until it reached 5 degree below the BP of the solvent. At this step, PDMS solidification ends, while the water and the solvent still remain in the bubbles. Additional heating over the BP of the solvent completely vaporizes the remaining water and the solvent to form empty pores (see Figure 2.1)

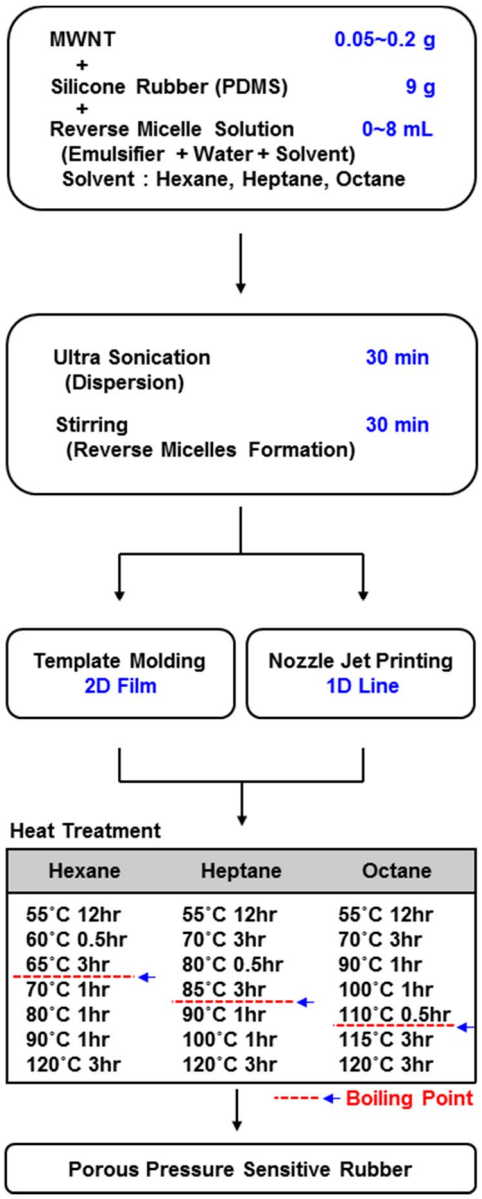

Figure 2.1 a) Detailed flow chart of the fabrication process of reverse micelle-induced PPSR.

Mechanical and electrical characterizations methods: The morphologies of the products were characterized by using a digital single-lens reflex camera (Cannon EOS 600D, Japan), a μ-CT (Skyscan, Bruker, Belgium), and an optical microscope (BX41M-LED, Olympus, Japan). Pressure measurements were performed with a custom-made mechanized z axis stage and a force gauge (BCA-100L, CAS, South Korea), which were used to apply and measure the pressure, respectively. The mechanical properties of materials were characterized after bringing the z axis stage into a slight contact with the top surface of PPSR. Then the stage moves downward at the speed of 10 mm/s. In the cyclic fatigue test, the baseline was stabilized by several pre-cycles. The electrical measurements were performed with a digital multimeter (NI USB-4065, National Instrument, USA) while tensile/compressive deformations were imposed. The performance of the motion detector was evaluated on a manual bending stage and the human wrist. The resistance change was measured between both ends of the patterned line which were connected by electrode leads (carbon fiber or commercial copper line).

2.3 Result and Discussion

Figure 2.1 shows the overall process of fabricating PPSR. It begins by mixing multi-walled carbon nanotubes (MWNTs), silicone rubber (poly(dimethylsiloxane); PDMS), and reverse micelle solution (RMS). RMS is comprised of an emulsifier (polyoxyethylene nonylphenyl ether, branched; IGEPAL® CO-520, Sigma Aldrich, USA), deionized (DI) water, and an organic solvent (i.e. hexane, heptane, or octane, Sigma Aldrich, USA). The mixed solution was ultrasonicated for 30 min and subsequently stirred for another 30 min until it became a homogeneous black gel-like solution (Figure 2.2a). This method evenly distributes the MWNTs in the viscous media and forms uniform reverse micelles, which are water droplets surrounded by the emulsifiers[22], while the PDMS/organic solvent/MWNT mixture is located outside the reverse micelle (Figure 2.2a, right bottom). The resulting black gel-like solution was poured into a flat, shallow, enclosed template to form the film (Figure 2.2b), while line patterns were produced using nozzle-jet-printing on the target substrates (Figure 2.2c). They were subsequently heated to solidify the PDMS and form the porous structures. Covering the surface of the solution helped to uniformly distribute the pores throughout the rubber. Figure 2.2d shows schematic illustrations and high-resolution images of the process. The temperature was increased step-by-step following the heat treatment process (Figure 2.1, bottom). The reverse micelles had migrated, merged together, and evaporated

during the process, producing the porous structure (See Experimental section for the detailed heating procedures and their effect on the porous structure).

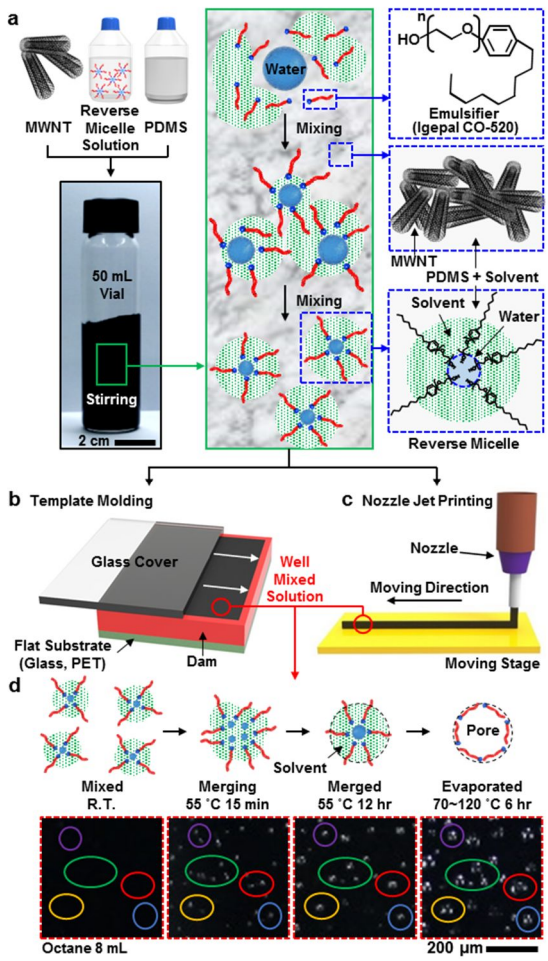

Figure 2.2 a) Schematic diagram of mixing procedure. MWNTs, RMS, and PDMS were mixed, dispersed under the ultra-sonication and stirred. The molecular structure of the emulsifier and the schematic illustration of the reverse micelle are shown in the right top and bottom insets, respectively. b) Schematic illustration of the template molding method for the PPSR film formation. c) Schematic illustration of the nozzle jet printing method for the PPSR pattern formation. d)

Schematic illustration of the behaviors of reverse micelles during the heat treatment procedure (top). High resolution images at each heat treatment step (bottom). As the heat treatment proceeded, the reverse micelles merged together and the size of bubbles (white dots) increased. After the evaporation, the bubbles became the pores.

The micro-computed tomography (μ-CT) images in Figure 2.3a show the pore characteristics of the PPSR fabricated using hexane-, heptane-, and octane-based RMS (4, 6, and 8 mL). As the boiling point of the solvents decreased, the resulting PPSR exhibited larger pores and higher porosity. A similar trend was observed when the amount of RMS was increased. Figure 2.3b shows 0-, 0.5-, 1.0-, and 1.5-mm-deep three-dimensional tomographic images and their combined images (top) of the PPSR fabricated using hexane and octane.

As shown in Figure 2.4, the amount of conducting filler also affected the pore size. During the heat treatment, MWNTs hinder the migration of reverse micelles. Therefore, the more MWNTs were mixed, the smaller pores were formed. Figure 2.4a shows a photograph of the porous rubber containing 0 g, 0.01 g, and 0.1 g of MWNTs. Transmitted light images clearly reveal the morphology of pores (Figures 2.4b-d). As the composition of MWNTs increased, the size of pores decreased.

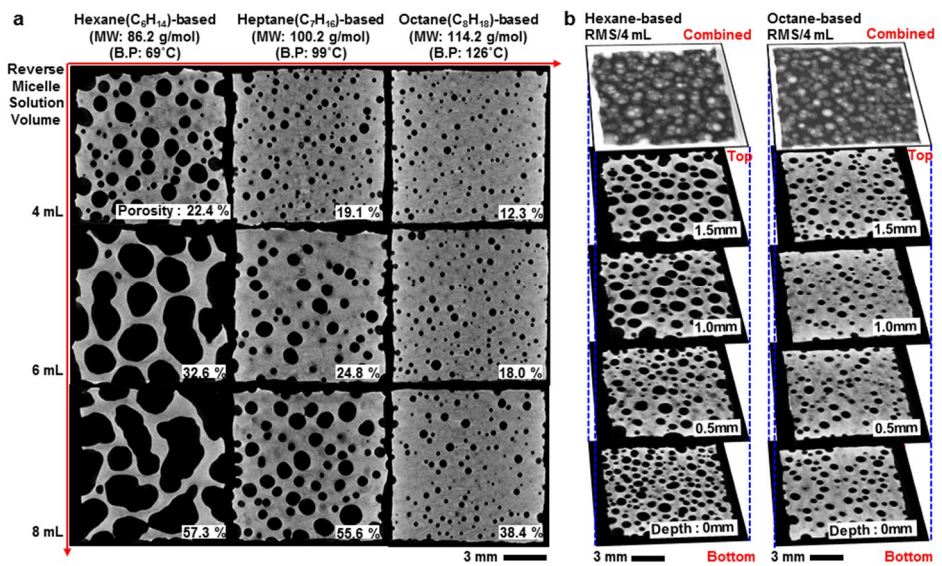

Figure 2.3 a) Micro-computed tomography (μ-CT) images at different RMS volumes (4 mL, 6 mL and 8 mL) and molecular weights (86.2 g/mol, 100.2 g/mol, 114.2 g/mol for hexane, heptane, octane, respectively). Porosity was calculated by the software of μ-CT and written at the right bottom of each frame. b) Three dimensional stacked μ-CT images of PPSR made of hexane-based RMS/4 mL (left) and octane-based RMS/4 mL (right) at different depth. The top frame shows the combined image of all μ-CT images.

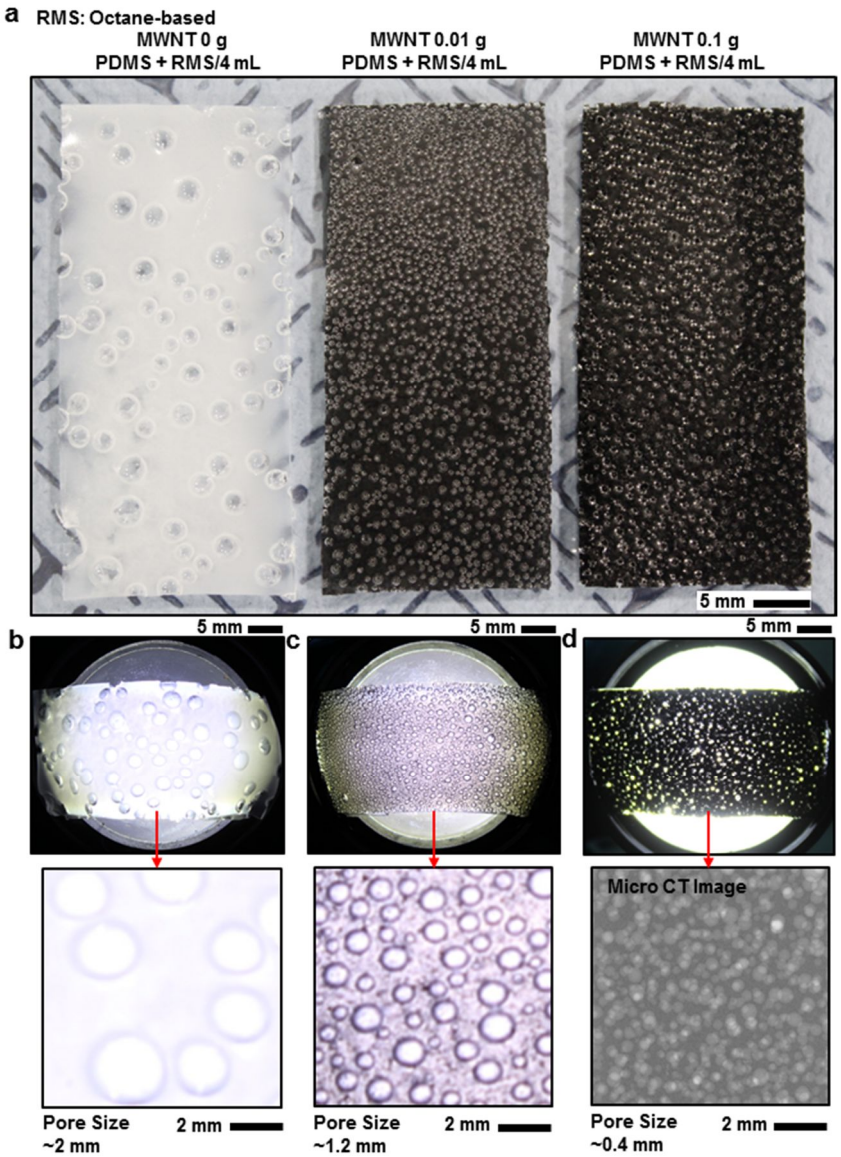

Figure 2.4 (a) Image of porous rubbers (9 g PDMS + octane-based RMS/4 mL) containing 0 g, 0.01 g and 0.1 g of MWNTs, respectively. (b-d) Transmitted light images of porous rubbers containing 0 g (b), 0.01 g (c) and 0.1 g (d) MWNTs and corresponding high magnification images (bottom).

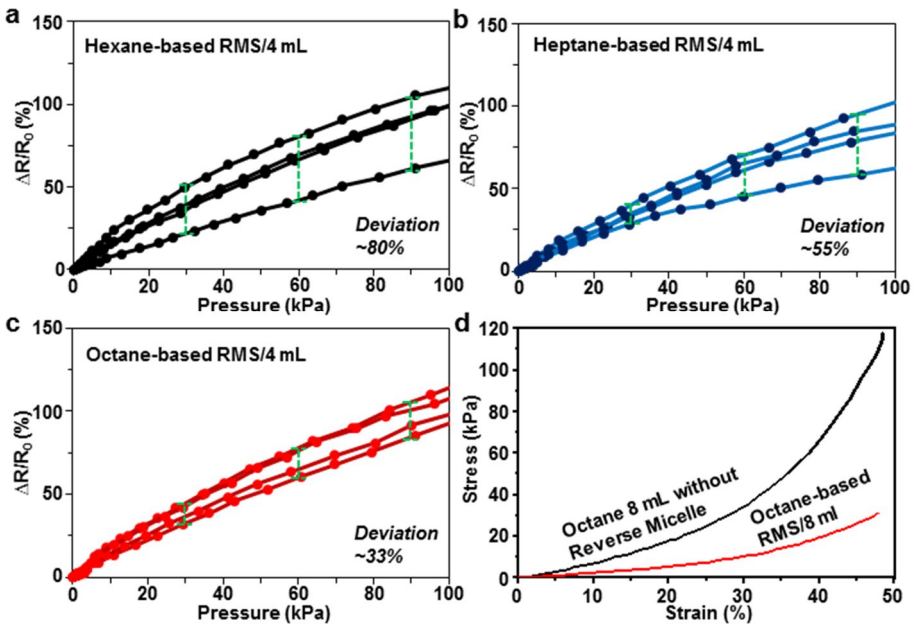

Figure 2.5 a-c) The sample-to-sample percent resistance change deviation of hexane-based RMS/4 mL a), heptane-based RMS/4 mL (b), and octane-based RMS/4 mL PPSR (c). (d) The stress-strain curves of PPSR made of octane 8 mL, or octane-based RMS/8 mL.

Smaller pores led to more uniform piezoresistive characteristics. Figure 2.5 shows percent resistance changes and their sample-to-sample deviation for the hexane-, heptane- and octane-based RMS/4 mL PPSR (Figures 2.5a, b and c, respectively). According to the results (Figure 2.3), the octane-based RMS/4 mL PPSR with 0.1 g MWNT had the smallest pores and the most uniform distribution of pores, and therefore the most uniform sensitivity was achieved. Additionally, when pores were made by an organic solvent without reverse micelles, pores were hardly formed and thereby the PPSR showed poor sensitivity (Figure 2.5d).

The three-dimensional finite element models for the PPSRs (Figure 2.6) were consistent with the experimental data (Figure 2.3). The finite element method (FEM) was used to estimate the PPSR deformation at given external applied pressures and to theoretically analyze the increase in porous structure sensitivity. Figures 2.7a and b show the electrical characterization ($\Delta R/R_0 = (R-R_0)/R_0$, where R_0 represents the initial resistance, see Table 1) and the strain-stress curves (whose slopes represent the Young's moduli) for various PSRs and PPSRs, respectively. The percentage change in the resistance linearly increases with increasing pressure (Figures 2b): the steeper the slope, the higher the sensitivity. The modulus of the PDMS depends on the ratio of the amounts of prepolymer to curing agent used. In addition, the pores decrease the modulus (Figure 2.7b). Consequently, solid PSR (10:1 composition) showed the highest modulus, while RMS/8 mL PPSR (30:1 composition) showed the lowest modulus. As the modulus decreased, going from the solid PSR (10:1 composition) to the RMS/8 mL PPSR (30:1 composition, RMS was octane based), the sensitivity increased, which is related to the increased deformation (ΔZ, Figure 2.7c).

Figure 2.8 shows the strain distributions calculated for the solid PSR (30:1 composition), RMS/4 mL PPSR (30:1 composition), and RMS/8 mL PPSR (30:1 composition) at an applied pressure of 25 kPa. Because of the difference in the modulus, the RMS/8 mL PPSR showed the largest deformation, while the solid PSR showed the smallest. In addition, much stronger localized strain was generated inside the PPSRs (in particular, near the wall between the pores), which was the

result of the structural inhomogeneity originating from the embedded pores. The larger overall deformation caused by the smaller modulus and the higher strain in the localized area resulted in a larger change in resistance, i.e. higher sensitivity, for the PPSR.

Finite element simulations were performed to analyze the deformation in the PPSR microstructure under compression (Figure 2.8) using the commercial finite element software Abaqus (V6.13, Dassault Systèmes, France) was used. The finite element models of the PPSR microstructure (dimension: 2 x 2 x 2 mm^3) were reconstructed from the μ-CT images using the image processing software Mimics (Materialise, Belgium). Ten-node quadratic tetrahedral three dimensional solid elements were used. The neo-Hookean model (strain energy $W = C_1(I_1 - 3)$ where $I_1 = \lambda_1^2 + \lambda_2^2 + \lambda_3^2$ and λ_i are the principal stretches) was used to represent the dense elastomers with the parameter C_1 = 61.08 kPa, 24.42 kPa, and 8.0 kPa for 30:1 solid PSR, RMS/4 mL PPSR, and RMS/8 mL PPSR, respectively.

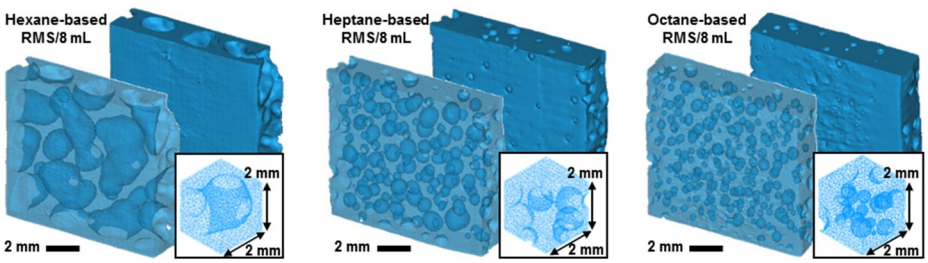

Figure 2.6 Three dimensional finite element models of PPSRs by using the transparent mode (front) and the solid mode (back) for hexane-based RMS/8 mL (left), heptane-based RMS/8 mL (center), and octane-based RMS/8 mL (right). The inset shows the magnified view.

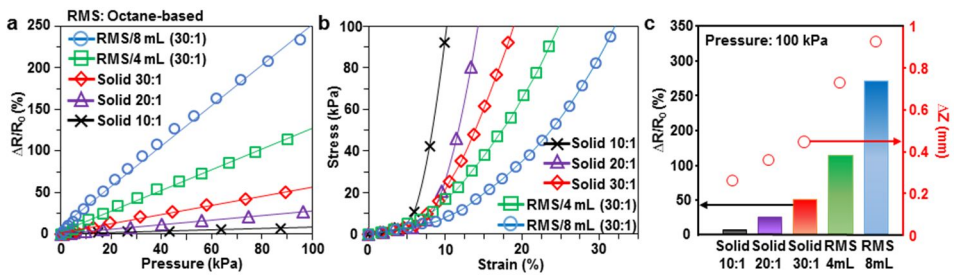

Figure 2.7 a) The percent resistance change of deformed PSRs and PPSRs at different applied pressures. b) The stress-strain curves of PSRs and PPSRs. The Young's modulus can be estimated from the slope at the linear region of each curve. c) The percent resistance change (y axis on the left) and the amount of deformation (y axis on the right) for different PSRs and PPSRs under the pressure of 100 kPa.

Sample	R_0 (Ω)	Sample	R_0 (Ω)
Solid 0.025 g	3765.0	RMS/4 mL	131.9
Solid 0.05 g	135.8	RMS/8 mL	219.6
Solid 0.1 g	28.7	RMS: Octane-based	
Solid 0.15 g	15.4		
Solid 0.2 g	11.5		

Table 1 Initial resistances of the samples. Note: Resistance was measured by digital multimeter operated at the voltage of 0.1 V and the current of 0.001 A ~ 0.1 A

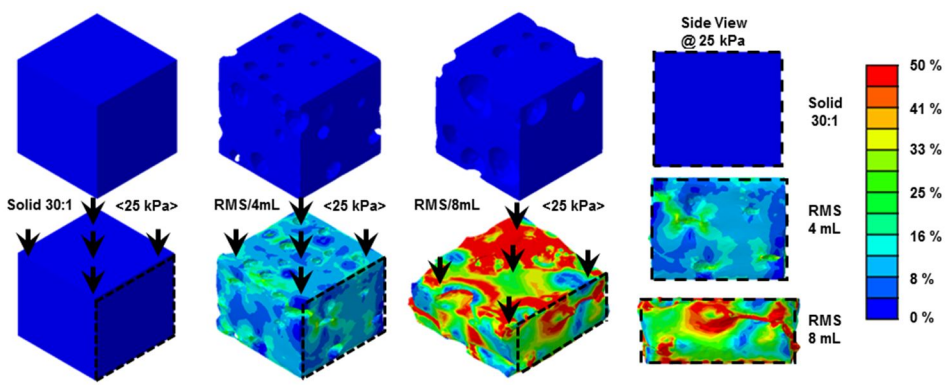

Figure 2.8 The FEM analysis of deformed PSR and PPSRs. The strain distribution was mapped for the solid 30:1 PSR (1st column), the RMS/4 mL PPSR (2nd column) and the RMS/8 mL PPSR (3rd column) with the applied pressure of 25 kPa. The strain distributions of the side view for each case are shown in the 4th column.

For the detailed mechanism of the piezoresistivity of the MWNT-filled elastomer, three dimensional resistor network analysis was proceeded. The MWNTs dispersed in the elastomer form electric conductive paths by tunneling conduction across the elastomer when the MWNT loading exceeds a critical value, called the percolation threshold.[23] When the MWNT-filled elastomer is subject to an external load, the resistance of the elastomer changes. The two mechanisms responsible for the piezoresistivity of the MWNT-filled elastomer are as follows:[24] 1) the destruction of conduction network, and 2) the piezoresistivity of MWNTs. The piezoresistive responses of the MWNT-filled PDMS with various MWNT loadings are shown in Figure 2.9a. In all five cases, the resistance increased with the increasing pressure. In addition, PDMS with low CNT loading showed higher sensitivity. This was because the PDMS with low CNT loading had lower modulus, thus underwent more deformation upon a given pressure. Moreover, the PDMS with lower CNT loading had fewer conductive paths than that with higher loading, and therefore the resistance was affected more by the destruction of conductive paths (Figures 2.9b, c, d and e).

To predict the resistance of the MWNT-filled PDMS, a three dimensional resistor network model was used.[25] MWNTs were represented by the randomly distributed conductive wires (length: 200 nm, diameter: 20 nm) in a three dimensional unit cell (1 x 1 x 1 μm3). The MWNT conductivity of 104 S/m was used. When two MWNTs were within a distance less than the diameter, a conducting path between the two was formed with a resistance of 100 kΩ. Upon an

applied pressure, the elastic deformation of PDMS changed the locations of MWNTs. It was assumed that the center and direction of a wire follows the deformation of the PDMS, but 10% of the total strain on PDMS was applied to the wire considering the difference in modulus and the poor contact between MWNT and PDMS.[26] The piezoresistivity of 200 was used for MWNT.[27] Figure 2.9f shows the three dimensional resistor networks equivalent to 0.1 g MWNT loading and the current density for various applied pressures. The current density was normalized by that of a straight MWNT aligned in the pressure loading direction. As the pressure increases, the conductive contacts are destroyed and the resistance of MWNTs increases, thus the overall resistance increases. Figure 2.9g shows the calculated resistance change for various MWNT loadings. The three dimensional resistor model reproduced the resistance increase under pressure as well as the higher sensitivity of PDMS with lower MWNT loading.

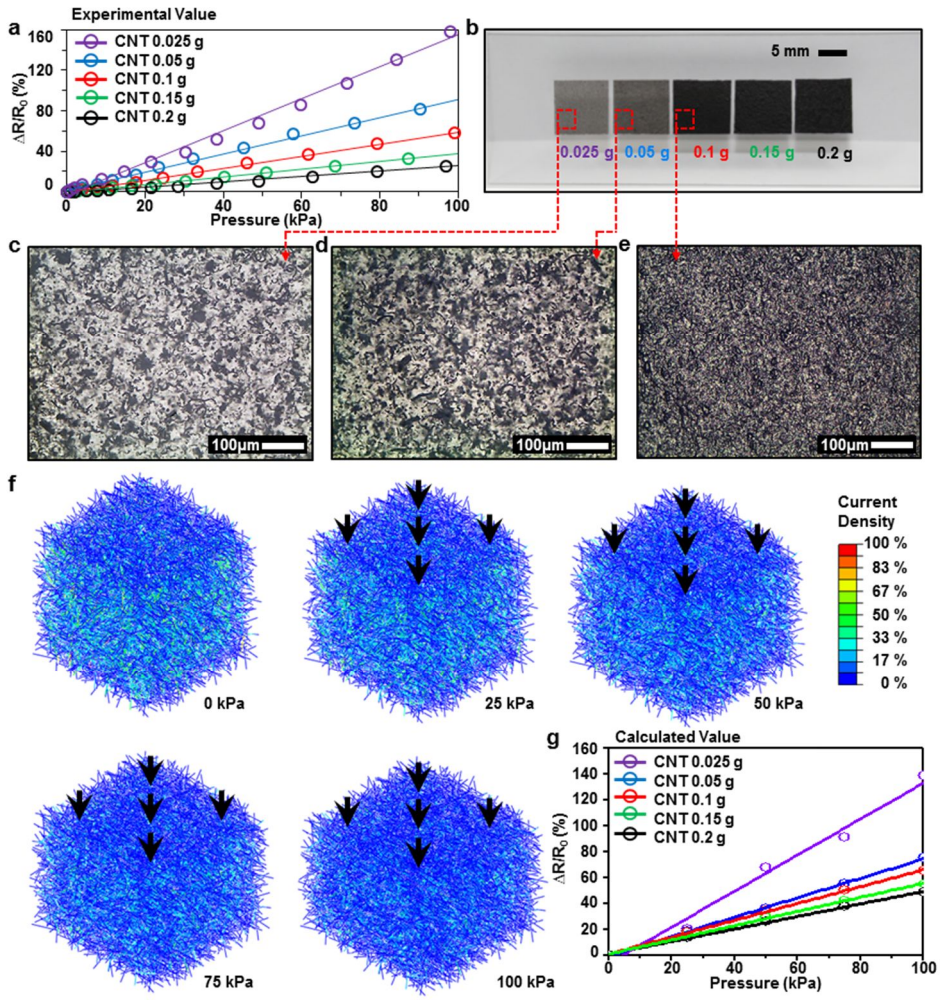

Figure 2.9. a) The percent resistance change of deformed solid PSRs at applied pressures. b) Images of solid PSRs made by 0.025 g, 0.05 g, 0.1 g, 0.15 g and 0.2 g MWNT, respectively. c-e) The corresponding optic microscope images of solid PSR made by 0.025 g c), 0.05 g d) and 0.1 g e) MWNT. f) The current density distribution of the 3D resistor network model for various applied pressures. The current density is normalized by that of a straight MWNT aligned in the pressure loading direction. g) The calculated percent resistance change of deformed solid PSRs at different applied pressure using 3D resistor network analysis.

The current method is easily scalable (Figure 2.10a). The low viscosity of the RMS/8 mL sample (Figure 2.10b) enabled the large-scale production and fabrication of large-area (23 cm × 16 cm, Figure 2.10c) PPSR films. Pressure-sensitive fabric, which was produced by sandwiching the PPSR film with conductive carbon fabric (Figure 2.10c), is a potential application of PPSR film. Stretchable conductive rubber was used as a binder (inset of Figure 2.10c). Different degrees of deformation in the stacked PPSR film are displayed in Figure 2.11a. The PPSR was compressed and easily reverted to its original shape when the applied pressure was released. Cycle tests were performed to further evaluate the mechanical reliability of the pressure-sensitive fabric (Figures 2.11b and c). The PPSR showed identical changes in the modulus and resistance in response to repeated compressions (~30% strain, ~10 kPa pressure). As shown in Figure 2.11d, the pressure-sensitive fabric discriminates among 50, 130, and 260 kPa several times, indicating that it is suitable for the application to smart wearable products, such as pressure-sensitive clothing that monitors external impacts and falls.

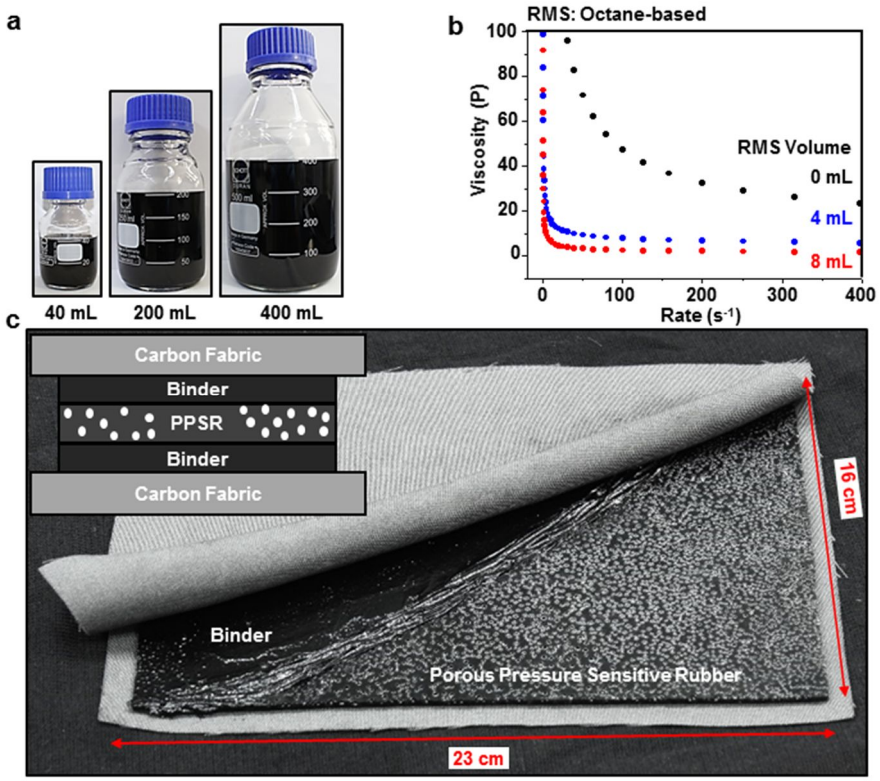

Figure 2.10. a) Images of mixed black gel-like solutions (40 mL, 200 mL and 400 mL). (b) The viscosity of black gel-like solutions made of different volume of RMS/0 mL, /4 mL and /8 mL. c) Image of a large-area PPSR-based pressure sensitive fabric. The PPSR film was sandwiched by conductive carbon fabrics. A custom-made conductive binder was used to assemble the PPSR film and carbon fabrics. The inset shows the cross-section cartoon of the assembled pressure sensitive fabric.

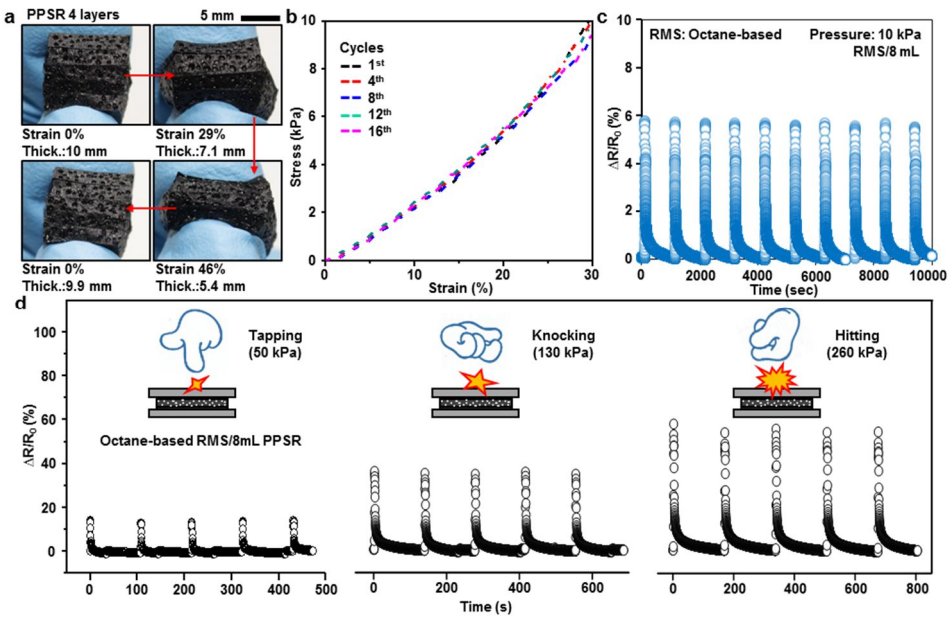

Figure 2.11. a) Images showing the reversible compressibility of stacked PPSR films. b) The strain-stress curves of PPSR. The slope shows almost identical characteristics for the repeated applied pressures. c) The percent resistance change of RMS/8 mL PPSR with 10 kPa applied pressure. d) Resistance change response of the pressure sensitive fabric to external applied pressure. Insets show illustrations of each mode: tapping (left), knocking (center), and hitting (right).

Computer-aided-design-(CAD)-based nozzle jet printing was used to produce various line patterns (Figures 2.12 and 2.13). The schematic illustration of nozzle jet printing is shown in Figure 2.12a. After the PPSR was patterned by moderating the flow rates and the nozzle movement speeds, the patterned PPSR was covered with the silicone oil, which facilitated uniform pore distribution. Since silicone oil is immiscible with RMS, it did not damage the PPSR pattern. The heated patterned PPSR adhered well to the plastic substrate (polyethylene terephthalate) even after numerous deformations (Figures 2.12b and c). The magnified view shows uniformly distributed pores (Figure 2.12c, bottom). The PPSR was also printed on the stretchable elastomeric substrate (polyurethane foam, Figure 2.13c). Figure 2.14a shows that the percentage change in the resistance of the patterned PPSR depends on the applied tensile strain. The patterned PPSR has a good sensitivity over the wide range of induced strain and thereby can be applied for both bare skins (maximum induced strain < 20%) and joints (maximum induced strain > 30%). Figure 2.14b shows the strain distributions calculated for stretching (left frame) and bending (right frame) the PPSR patterns on the elastomeric substrate. For stretching, the region aligned with the stretching direction showed almost the same amount of induced strain with the applied strain (~30% strain), while the other region exhibited the weaker strain. For bending, the patterned PPSR was under bending-induced strain. The change in the local strain in the patterned PPSR during both stretching and bending changed the resistance (Figure 2.14c). Since the skin deformation is due to a combination of stretching and bending, the PPSR

printed on the commercial elastomeric patch (Medifoam, Ildong, South Korea) could be used as a skin-mountable strain gauge to monitor human body motion (Figures 2.15a, b and c). Conformally integrating the device with the skin is important to minimize movement artefacts.[8-10] The low modulus of the PPSR enabled wearable sensors to be intimately integrated with the moving wrist (Figure 2.15a, inset). The repetitive bending motions of a human wrist were monitored at two different frequencies (Figures 2.15b and c). The repetitive stretching test of the PPSR-based sensor didn't induce any significant signal and material degradations.

Finite element simulations were used to analyze the deformation and resistance change in the patterned PPSR during stretching and bending, shown in Figure 2.14. The finite element model for the patterned PPSR was generated by extruding a half disk (radius: 0.5 mm) along the patterned line, while the substrate (size: 90 x 40 mm^2) was modeled as a thin sheet. Eight-node hexahedral three dimensional solid elements and four-node shell elements were used for PPSR and the substrate, respectively. The patterned PPSR was placed on the substrate and was tied to the surface of the substrate. The boundary conditions corresponding to the stretching and bending were applied on the substrate. The neo Hookean model was used to represent the PPSR with the parameter C_1 =5.4 kPa. The following relationship was used to represent the piezoresistivity of the PPSR: $(\rho - \rho_0)/\rho_0 = C_\rho (I_1 - 3)^{\frac{1}{n}}$ where ρ_0 and ρ re the initial and current resistivities,

respectively, C_ρ =0.4672, and n =1.914, which were obtained by linear regression of the results in Figure 2.14a.

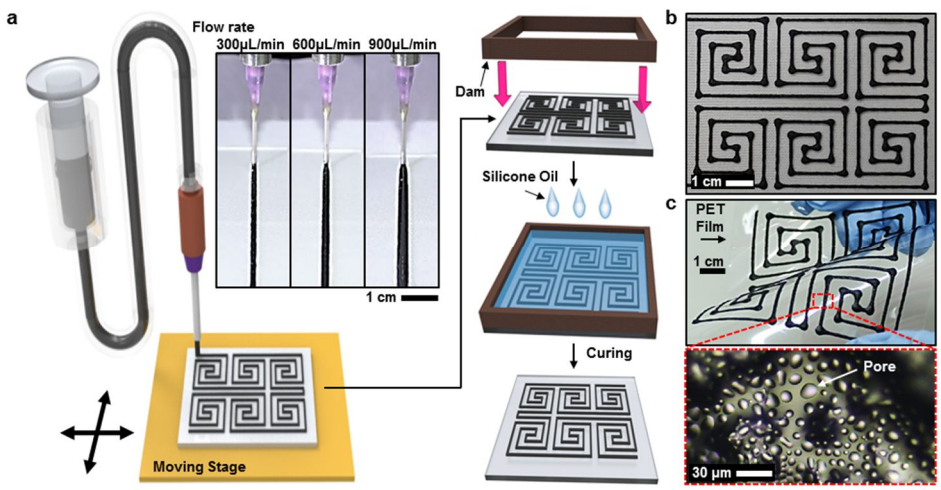

Figure 2.12. a) Schematic diagram of the nozzle jet printing process for the patterned PPSR. b) Image of the PPSR pattern printed on the flexible plastic substrate (PET film). c) Image of deformed PPSR pattern. Bottom frame shows the magnified image of the printed PPSR.

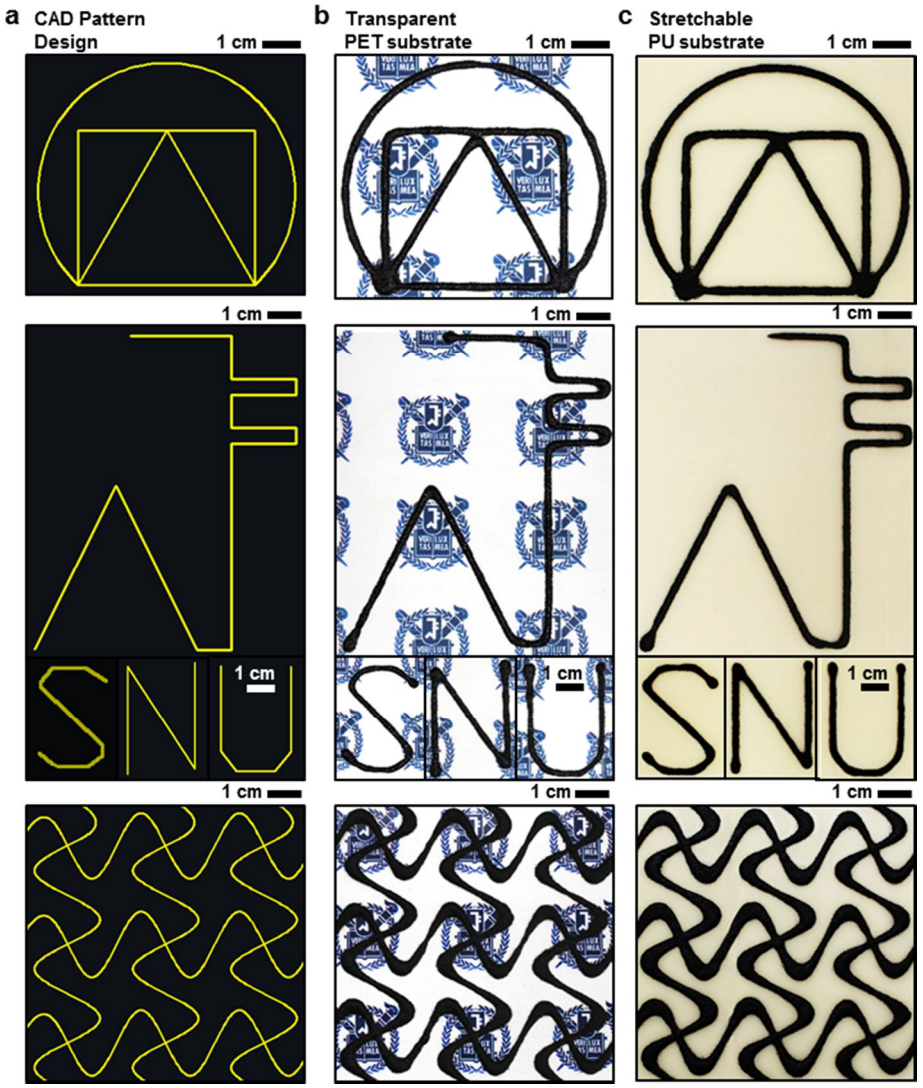

Figure 2.13. a) Images of various CAD designs. b) Corresponding images of nozzle jet printed PPSR pattern on flexible plastic substrate. c) Corresponding images of nozzle jet printed PPSR pattern on stretchable elastomeric substrate.

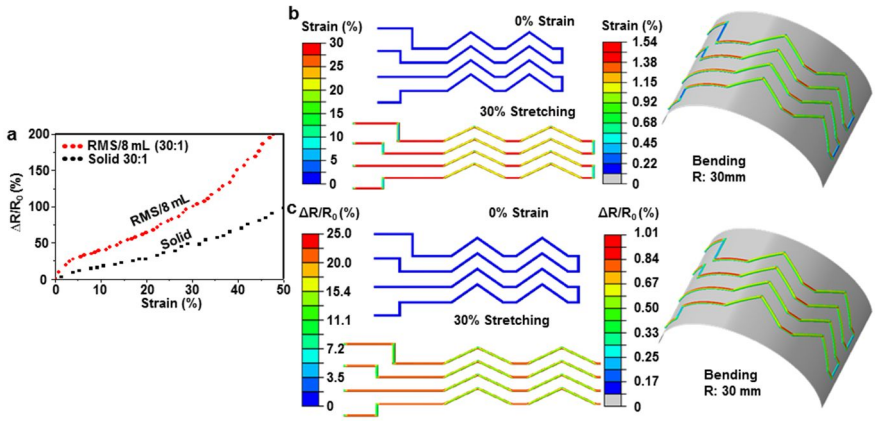

Figure 2.14. a) Percent resistance change of patterned PSR and PPSR on stretchable polyurethane substrate under external tensile strain. b) Strain distribution of the patterned PPSR on the stretchable substrate under ~30% stretching (left) and on the bent substrate with 30 mm radius of curvature (right). c) Percent resistance change distribution of patterned PPSR on the stretchable substrate at 0 % strain (left, top) and 30 % strain (left, bottom). Percent resistance change distribution of patterned PPSR on the stretchable substrate during the bending (right, 30 mm radius of curvature).

Figure 2.15. a) Monitoring the resistance change associated with deformations in

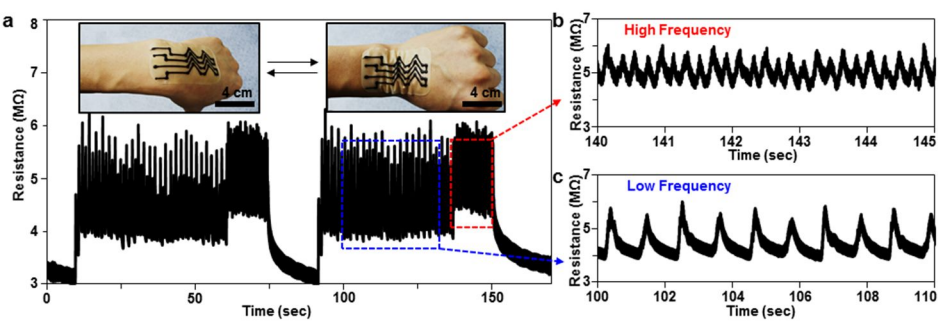

wrist movements by using skin-mounted strain gauges. The inset shows images of the patterned PPSR strain gauge laminated on the human wrist during bending. Magnified view of measured signals for b) high and c) low frequency movements.

Wearable mechanical sensors (i.e. pressure and strain sensors) were fabricated to demonstrate a human-machine interface (HMI). The wearable sensor array was used to remotely control a tank-like robot (MINDSTORMS® NXT 2.0, LEGO®, USA). Figures 2.16a and 2.16b show images of the PPSR-based pressure sensor and strain gauge, respectively, on a commercial elastomeric patch. The strain gauge was composed of two channels and was mounted on the middle (Ch 5) and index (Ch 6) fingers, which triggered acceleration (Ch 5, Figure 2.16c) and deceleration (Ch 6, Figure 2.16d), respectively. The pressure sensor consisted of four channels, each controlling a different action command of the robot: moving forward (Ch 1, Figure 2.16e), moving backward (Ch 2, Figure 2.16f), rotating counter-clockwise (Ch 3, Figure 2.16g), and rotating clockwise (Ch 4, Figure 2.16h). The skin-mounted pressure sensors and strain gauges were used to designate directions and control speeds (Figure 2.16i). Figure 2.16j shows the commands remotely delivered by mechanical motions (i.e. bending or pressing the fingers) through the six channels. Each signal measured by the pressure sensors or strain gauges (Figure 2.16j right bottom insets in the magnified view) corresponds to different motions of the robot (Figures 2.16i and j). A voltage divider circuit was constructed to convert the changes in the sensor resistance to the changes in the voltage for the data acquisition (DAQ, Figure 2.16j right top inset). The raw analogue voltage signals output from the voltage dividers were acquired using a DAQ board (NI USB-6289, National Instruments, USA). Discrete data points were sampled and processed in the custom-made LabVIEW (National Instrument, USA) program (See details of

the program algorithm (Figures 2.17 and 2.18) and the robot demonstration methods). The PPSR-based sensors showed sufficiently high linearity and sensitivity for HMIs. The robot control demonstration reported here is a significant step toward developing aid systems such as wheelchair controls for physically challenged patients.

Each skin-mounted sensor was connected in series to a 100 kΩ resistor, and the six resistor-sensor pairs were connected in parallel. When 5 V DC bias was applied to the circuit, the output signals were measured from the point between the resistor and the sensor (Figure 4j right top inset). The custom made LabVIEW program analyzes the output signal changes of the six skin-mounted sensors induced by mechanical motions (e.g. pressing or stretching) and activates a specific key pad. In this demonstration, we assigned 'W' key for forward, 'S' key for backward, 'A' key for counterclockwise rotation, 'D' key for clockwise rotation, 'T' key for acceleration, and 'G' key for deceleration. The control signal is generated by the custom made remote control program which allocates each key pads to a specific action of the robot. The robot (Mindstorms®, Lego®, USA) is composed of two servo motors, one intelligent brick (NXT 2.0) and other components, such as caterpillar tracks. As the control signal is received via the embedded Bluetooth module, the intelligent brick transmits commands to the servo motors to decide the speed and the direction of the rotation.

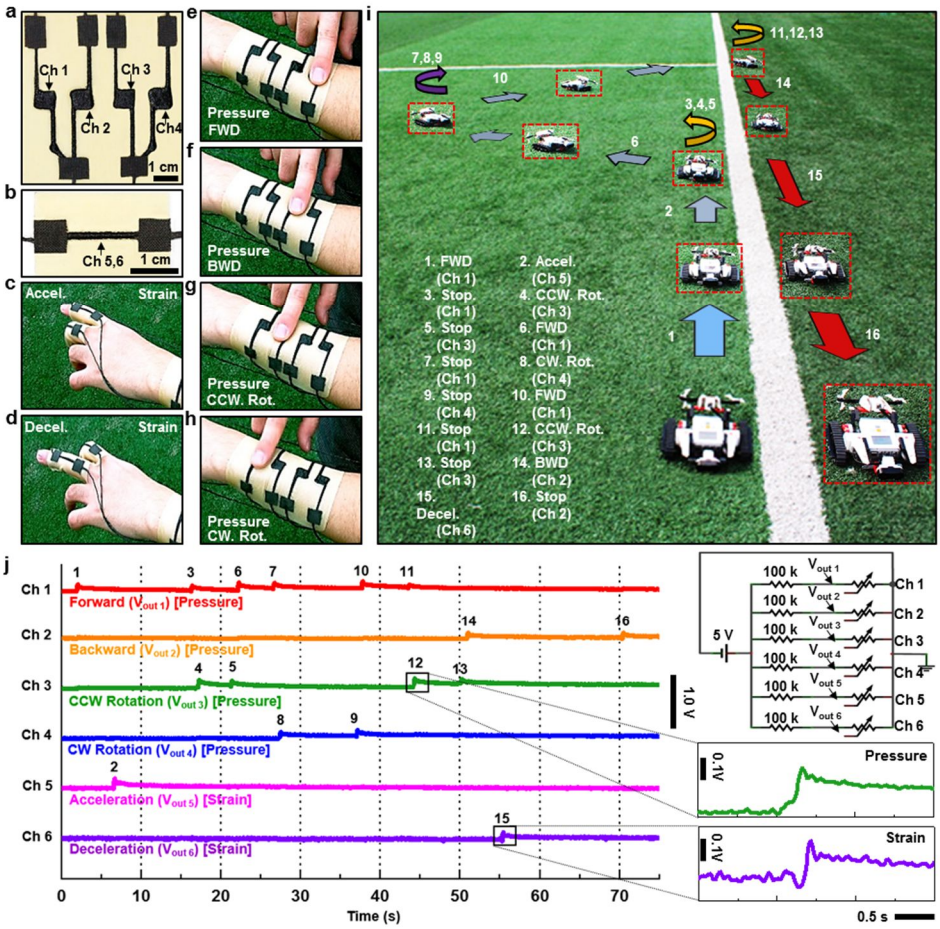

Figure 2.16. a) Image of PPSR pressure sensor printed on the commercial elastomeric patch. The sensor array is composed of four channels of pressure sensors. b) Image of PPSR train gauge. c,d) Image of triggering commands via PPSR strain gauges for the acceleration of the robot (Ch 5, c) and for the deceleration of the robot (Ch 6, d). e-h) Image of triggering commands via PPSR pressure sensors for moving forward (Ch 1, e), moving backward (Ch 2, f), rotating counterclockwise (Ch 3, g), and rotating clockwise (Ch 4, h). i) Image of robot movement traces. A series of commands were triggered. Each command is numbered on the figure. The numbers and corresponding commands are explained

on the left bottom corner of the figure. j), Voltage output signals from the array of skin-mounted mechanical sensors while controlling the robot wirelessly (Figure 2.16i). The numbers marked on the every signal of the data traces indicate the marked numbers on Figure 2.16i. The upper right inset shows a schematic diagram of the voltage dividing circuit to convert the resistance change into the voltage change. The bottom right inset shows magnified view of the signal measured from the pressure sensors and the strain gauges.

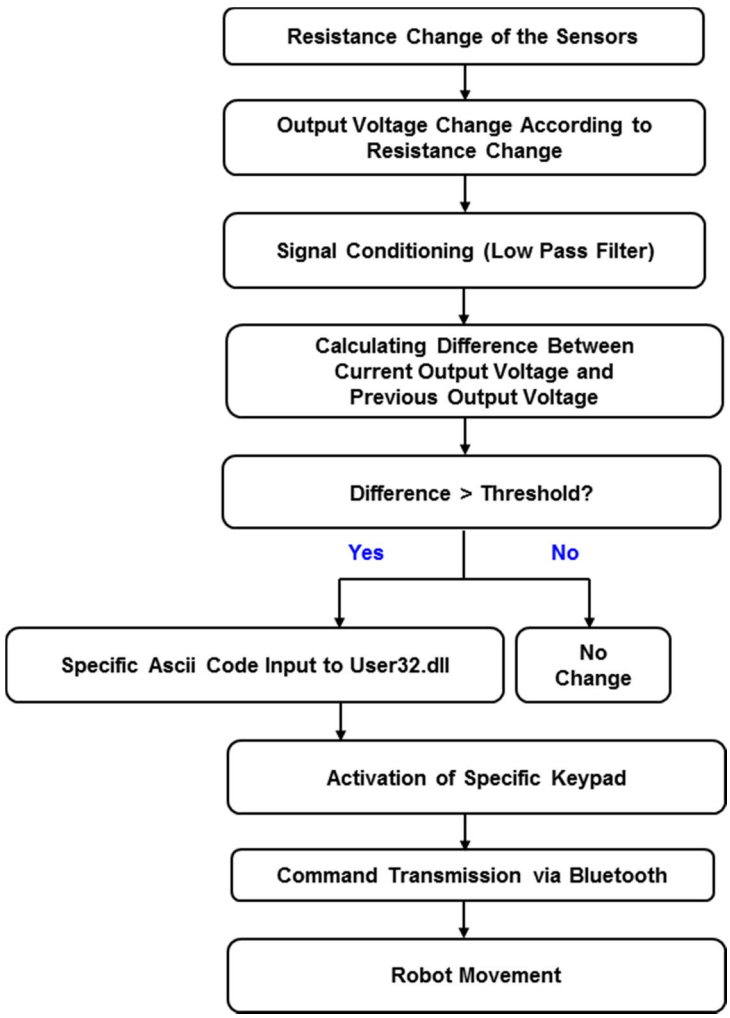

Figure 2.17. Process flow chart of the robot control.

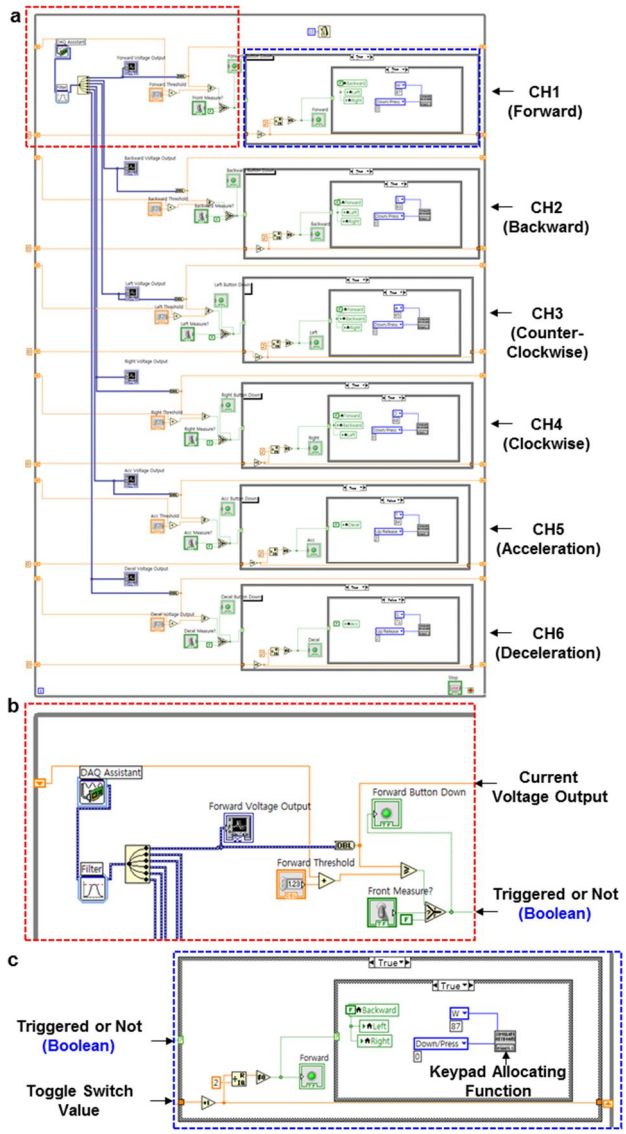

Figure 2.18. a) Block diagram of the custom-made LabVIEW program. b) Signal processing parts and comparing parts. c) Case structures of key pad allocation.

2.4 Conclusion

In summary, we used reverse micelles to develop a novel method of introducing pores into PSR. The method was used to control the pore characteristics of PPSR. The resulting PPSR-based sensors responded to external mechanical inputs with higher sensitivity than the conventional PSR-based ones, and the FEM analysis theoretically supported these experimental findings. A large-area pressure-sensitive fabric was produced by sandwiching the PPSR film with the conductive carbon fabric, which can be applied for producing pressure-sensitive clothing. The PPSR patterns produced using nozzle jet printing enabled a wearable multi-channel human-machine-interface device to be produced for wirelessly controlling robots. Further research on PPSR will provide new opportunities for developing personal wearable electronics and bio-medical device applications.

References

[1] S. C. B. Mannsfeld, B. C. -K. Tee, R. M. Stoltenberg, C. V. H. -H. Chen, S. Barman, B. V. O. Muir, A. N. Sokolov, C. Reese, Z. Bao, *Nat. Mater.* **2010**, 9, 859.

[2] D. J. Lipomi, M. Vosgueritchian, B. C. K. Tee, S. L. Hellstrom, J. A. Lee, C. H. Fox, Z. Bao, *Nat. Nanotechnol.* **2011**, 6, 788.

[3] B. C. -K. Tee, C. Wang, R. Allen, Z. Bao, *Nat Nanotechnol* **2012**, 7, 825.

[4] G. Schwartz, B. C. K. Tee, J. G. Mei, A. L. Appleton, D. H. Kim, H. L. Wang, Z. Bao, *Nat. Commun.* **2013**, 4.

[5] K. Takei, T. Takahashi, J. C. Ho, H. Ko, A. G. Gillies, P. W. Leu, R. S. Fearing, A. Javey, *Nat. Mater.* **2010**, 9, 821.

[6] C. Wang, D. Hwang, Z. Yu, K. Takei, J. Park, T. Chen, B. Ma, A. Javey, *Nat. Mater.* **2013**, 12, 899.

[7] T. Someya, T. Sekitani, S. Iba, Y. Kato, H. Kawaguchi, T. Sakurai, *Proc. Natl. Acad. Sci. USA* **2004**, 101, 9966.

[8] D.-H. Kim, N. Lu, R. Ma, Y.-S. Kim, R.-H. Kim, S. D. Wang, J. Wu, S. M. Won, H. Tao, A. Islam, K. J. Yu, T.-I. Kim, R. Chowdhury, M. Ying, L. Xu, M. Li, H.-J. Chung, H. Keum, M. McCormick, P. Liu, Y.-W. Zhang, F. G. Omenetto, Y. Huang, T. Coleman, J. A. Rogers, *Science* **2011**, 333, 838.

[9] J. A. Fan, W. -H. Yeo, Y. Su, Y. Hattori, W. Lee, S. -Y. Jung, Y. Zhang, Z. Liu, H. Cheng, L. Falgout, M. Bajema, T. Coleman, D. Gregoire, R. J. Larsen, Y. Huang, J. A. Rogers, *Nat. Commun.* **2014**, 5, 3266.

[10] N. Lu, C. Lu, S. Yang, J. Rogers, *Adv. Funct. Mater.* **2012**, 22, 4044.

[11] T. Someya, Y. Kato, T. Sekitani, S. Iba, Y. Noguchi, Y. Murase, H. Kawaguchi, T. Sakurai, *Proc. Natl. Acad. Sci. USA* **2005**, 102, 12321.

[12] M. Kaltenbrunner, T. Sekitani, J. Reeder, T. Yokota, K. Kuribara, T. Tokuhara, M. Drack, R. Schwodiauer, I. Graz, S. Bauer-Gogonea, S. Bauer, T. Someya, *Nature* **2013**, 499, 458.

[13] C. Pang, G. -Y. Lee, T. -I. Kim, S. M. Kim, H. N. Kim, S. -H. Ahn, K. -Y. Suh, *Nat. Mater.* **2012**, 11, 795.

[14] T. Yamada, Y. Hayamizu, Y. Yamamoto, Y. Yomogida, A. Izadi-Najafabadi, D. N. Futaba, K. Hata, *Nat. Nanotechnol.* **2011**, 6, 296.

[15] S. Gong, W. Schwalb, Y. Wang, Y. Chen, Y. Tang, J. Si, B. Shirinzadeh, W. Cheng, *Nat. Commun.* **2014**, 5, 3132.

[16] T. Sekitani, U. Zschieschang, H. Klauk, T. Someya, *Nat. Mater.* **2010**, 9, 1015.

[17] D.-H. Kim, N. Lu, R. Ghaffari, Y.-S. Kim, S. P. Lee, L. Xu, J. Wu, R.-H. Kim, J. Song, Z. Liu, J. Viventi, B. de Graff, B. Elolampi, M. Mansour, M. J. Slepian, S. Hwang, J. D. Moss, S. -M. Won, Y. Huang, B. Litt, J. A. Rogers, *Nat. Mater.* **2011**, 10, 316.

[18] L. Pan, A. Chortos, G. Yu, Y. Wang, S. Isaacson, R. Allen, Y. Shi, R. Dauskardt, Z. Bao, *Nat. Commun.* **2014**, 5, 3002.

[19] X. Gui, A. Cao, J. Wei, H. Li, Y. Jia, Z. Li, L. Fan, K. Wang, H. Zhu, D. Wu, *ACS Nano* **2010**, 4, 2320.

[20] H. -B. Yao, G. Huang, C. -H. Cui, X. -H. Wang, S. -H. Yu, *Adv. Mater.* **2011**, 23, 3643.

[21] H. Vandeparre, Q. Liu, I. R. Minev, Z. Suo, S. P. Lacour, *Adv. Mater.* **2013**, 25, 3117.

[22] M. H. Oh, N. Lee, H. Kim, S. P. Park, Y. Piao, J. Lee, S. W. Jun, W. K. Moon, S. H. Choi, T. Hyeon, *J. Am. Chem. Soc.* **2011**, 133, 5508.

[23] W. Bauhofer, J.Z. Kovacs, Compos. Sci. Technol. 2009, 69, 1486.

[24] Alamusi, N. Hu, H. Fukunaga, S. Atobe, Y. Liu, J. Li, Sensors 2011, 11, 10691.

[25] N. Hu, Y. Karube, C. Yan, Z. Masuda, H. Fukunaga, Acta. Mater. 2008, 56, 2929.

[26] B. Hu, N. Hu, Y. Li, K. Akagi, W. Yuan, T. Watanabe, Y. Cai, Nanoscale Res. Lett. 2012, 7, 402.

[27] W. Xu, M.G. Allen , J. Polym. Sci. Pol. Phys. 2013, 51, 1505.

Chapter 3. Fabric-based Integrated Energy Devices for Wearable Activity Monitors

3.1 Introduction

Wearable electronics have attracted great attention along with the development of flexible and stretchable electronics[1-7] as well as the rapid propagation of mobile devices[8]. Those devices are of a particular interest for the collection of physiological and electrophysiological information from the human body, with application examples including: epidermal electronics based on inorganic semiconductors[1,2], organic electronic devices laminated on the skin[3,4], highly sensitive pressure and strain sensors that can emulate human skin[5], active-matrix mechanical sensor arrays for electronic skins[6], and multifunctional electronic patches for the diagnosis and therapy of movement disorders[7]. However, most of the flexible electronics developed thus far have relied on the connection to external power sources through long wires, which often limits their mobile applications. Consequently, there is a pressing need to develop integrated power generation and storage devices that are readily incorporated into either implantable[9] or wearable devices.

A triboelectric generator (TEG) is one of the promising options for an energy harvesting device that can be used with wearable electronics. Compared to other wearable power generators, TEGs are sensitive to humidity, exposed to mechanical damage by friction, and discontinuous in power generation. Meanwhile, its fabrication is simple and cost-effective and thereby suitable for large area wearable systems.[10-18] Wang et al. have previously demonstrated that TEGs convert mechanical friction to electrical energy[10], with both contact/release[11-13] and sliding[14-18] movements. Contact/release type friction is most prevalent during vertical movement. In the contact state, electrons are transferred between the surfaces of two different materials. On transition to the release state, air gaps created between the two surfaces act to balance the electrical potential, thereby generating an electrical current through external wires by electrostatic induction[11-13]. On the other hand, the friction more commonly occurs during horizontal movements. Recent efforts to utilize horizontal friction have therefore focused on generating corrugated structures by patterning polymer arrays to create vacant air gaps[14-16]. However, maintaining these structures (i.e. air gaps) requires the use of rigid materials, which is clearly incompatible with flexible devices. A new type of TEG, which is both not reliant on air gaps[17] and flexible,[18] is therefore needed to utilize horizontal friction as an energy source in wearable electronics.

To ensure the fully independent operation, the power generated by a TEG also needs to be stored within the wearable system itself, for which an all-solid-state flexible energy storage device[19-21] is needed. Supercapacitors (SCs) appear to be

one of the most suitable energy storage devices for this purpose, because they offer a high power density, fast charging/discharging speed, and a long cycle life.[22] Furthermore, SCs are safe and environment-friendly.[23] Indeed, their energy density has been greatly improved over recent years, reaching a level comparable with lead-acid batteries.[24] We therefore herein present a wearable integrated energy device, consisting of TEGs combined with SCs, which can be utilized either as an activity monitor or as power supply for other wearable sensors.

* The contents of this chapter was published on Advanced materials (2014, 26, 6329-6334)

3.2 Experimental Section

Fabrication of the Flexible Triboelectric Generator on CF: To fabricate TEG I, a piece of CF (W0S1002, CeTech, Japan) was pattered by using a 5 mm wide polyimide (PI, DuPont Kapton, France) tape spaced at 5 mm intervals. Polyurethane acrylate (PUA, MINS-311RM, Minuta Tech, South. Korea) was then poured over the CF, and a 3M-magic-tape-covered PET fi lm was placed over the top and pressed to ensure uniform thickness of the PUA fi lm. After solidifying the PUA by irradiating it for 12 h under an ultra-violet (UV) lamp (ca. 365 nm, 40 W, BL lamp, Minuta tech, South Korea), the PI tapes were removed. Additional PI tapes were then stacked on the exposed area of CF until the surface was made level.

To fabricate TEG II, a second piece of CF was pattered by 5 mm Al tape (3M, USA) with 5 mm intervals. The Al lines were then covered by PI tape, and PDMS (10 : 1 mixture of prepolymer : curing agent; Sylgard 184, Dow Corning, USA) was poured over the CF. A PI-covered PET film was then placed over the PDMS and pressed by a 3 kg stainless steel plate to ensure a uniform PDMS fi lm thickness. After curing the PDMS in a convection oven at 90 °C for more than 12 h, the PI tapes were removed. Additional layers of Al tape were then stacked on the Al lines to create a level surface.

These fabricated layers, each measuring 0.75 cm^2 in area (L: 1.5 cm, W: 0.5 cm), were attached to a commercial fabric by a fabric bonding agent. A parallel

connection between each TEG was then created by sewing a conductive carbon thread (Panex30, Zoltek, USA).

Fabrication of the Supercapacitor on CF: To synthesize the vertical single-wall CNTs, a 10 nm thick aluminum layer was first deposited on the CF using a thermal evaporator (Selcos, South Korea), onto which a 3.5 nm thick Fe layer was deposited by an e-beam evaporator (Scien tech. Co., Ltd, South Korea) to act as a catalyst. The water-assisted synthesis of CNTs was performed at atmospheric pressure by first placing the catalyst-coated CF on a quartz plate, and then loading it into a 1-in diameter CVD quartz cylinder. The temperature was then ramped to 730 °C under a 100 sccm flow of 99.999% pure Ar and 50 sccm of Ar containing H_2O. When the target temperature was reached, 75 sccm of ethylene and 100 sccm H_2 were introduced to the reactor for 10 minutes as the precursor and carrier gas, respectively. The RuO_2 electroplating solution was prepared using 5 mM ruthenium (III) chloride hydrate (Sigma-Aldrich, USA), 0.1 M KCl (Sigma-Aldrich, USA), and 0.01 M HCl (Sigma-Aldrich, USA) in DI water. A 3 M NaOH solution was then slowly added, until the pH of the plating solution reached 2.0. Prior to plating, the CNTs were hydrophilized by O_2 plasma using a reactive ion etcher (Scien tech. Co., Ltd, South Korea). The plating solution was then heated to 50 °C in a water bath, and a cyclic voltammetry of between -0.2 V and 1.0 V was applied at a 0.05 mV/s scan rate using a potentiostat (600E Potentiostat/Galvanostat, CH Instruments, USA) with a Pt counter electrode and an Ag/AgCl reference electrode

in NaCl. The electrolyte for the SCs was prepared by adding 6 g of PVA (MW: 14,600–18,600 g/mol, Sigma-Aldrich, USA) to 60 mL of DI water containing 9 g of H_3PO_4 (Sigma-Aldrich, USA). The resulting mixture was then heated to 104 °C in a mineral oil bath with constant stirring until a clear solution was obtained. This was then poured into a petri dish and dehydrated at room temperature to obtain a gel film

3.3 Result and Discussion

The structure and principle of operation of the wearable energy supply system is depicted schematically in Figure 3.1. Note that all devices were fabricated on a conductive carbon fabric (CF), which allows them to be woven onto designated locations of conventional clothing, and interconnected by conductive threads. As shown in Figure 3.1a, the TEGs were positioned in the armpit region to maximize friction[25], whereas the SC was located on the chest section, a region that is safe from friction damage, yet still close to the TEGs. The typical swinging motion generated during walking and the corresponding electricity generation and storage are also shown. A circuit diagram of the integrated energy supply devices is provided in Figure 3.1b, wherein multiple TEGs are connected in parallel to generate sufficient electrical current to charge the SCs. The rectifier positioned between the TEGs and SCs converts the generated alternating current (AC) into the direct current (DC) to charge the SCs.

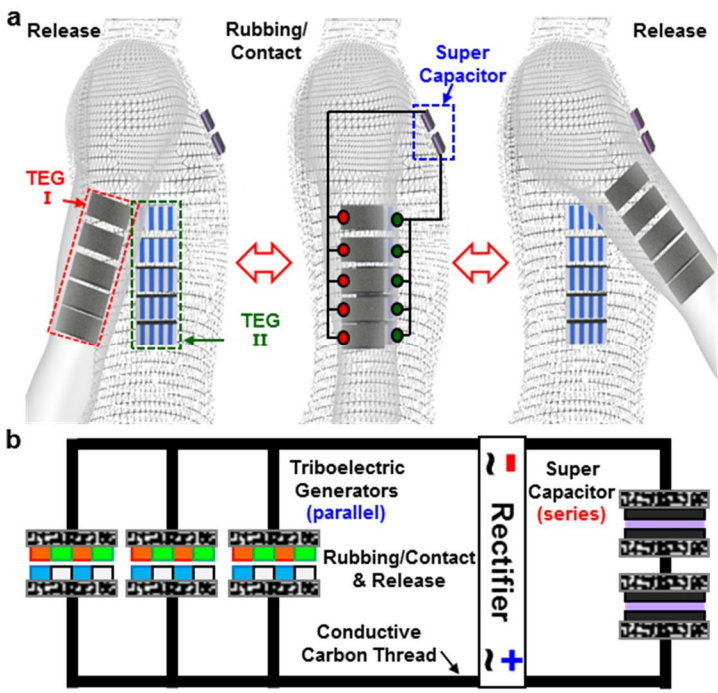

Figure 3.1 Schematic descriptions and morphology of the TEG and SC. a) Schematic illustration of arm swings with TEG and SC equipped. b) Circuit diagram of the integrated energy supply devices.

The design of the TEGs is based on a controlled alignment of four complementary materials, which allows them to utilize both the vertical and horizontal friction generated between the arm and the torso. For the inner side of the arm, polyurethane (PU, roughness quadratic mean (Rq) = 158 nm) and polyimide (PI, Rq = 23.5 nm) were alternatingly patterned on CF to form what is hereafter referred to as TEG I (Figures 3.2a). On the opposite surface, a similar patterning of polydimethylsiloxane (PDMS, Rq = 49.4 nm) and aluminum (Al, Rq = 200 nm) was used to create TEG II (Figures 3.2b). Each of these materials has its own relative degree of triboelectric polarity, with Al connected to the circuit as a conducting material which transfers electrons to the polymer surfaces. The generated electricity is stored in the integrated fabric-based SC, which has a symmetric structure (CF/carbon nanotube (CNT)/RuO2 electrode - polyvinyl alcohol (PVA)/H3PO4 gel electrolyte - CF/CNT/RuO2 electrode) as shown in Figure 3.2c.

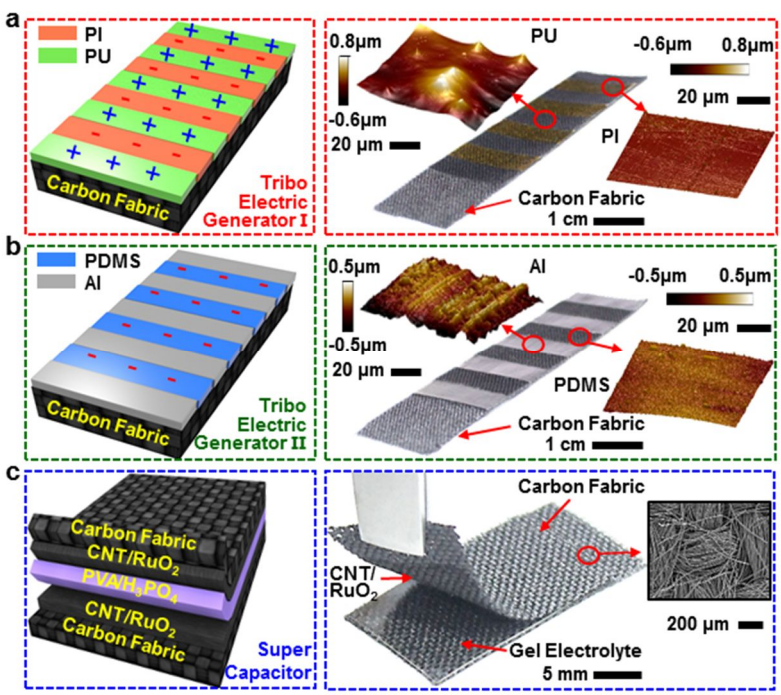

Figure 3.2 Schematic illustrations of individual components and digital photos of individual components: a) TEG I, b) TEG II, and c) SC. Insets showing AFM images.

The most notable advantage of this design is that unlike TEGs developed previously[10-16], it allows TEGs to generate electricity without the need for air gaps. From the schematic diagrams of the TEG structures and their relative triboelectric strengths shown in Figure 3.3a, it is apparent that the polarity of the induced current is determined by the relative position of each material. The proposed mechanism for this is shown in Figures 3.3b, in which positive and negative peaks are observed as Al is aligned with PU and PI, respectively. This can be explained by the combined effect of two phenomena: the dynamic electrification between insulators and the electron transfer between the conductor and the insulator (Figure 3.3b). Moreover, given that the Al conducting layer always transmit electrons to the electrode, it plays an important role as a charge reservoir. The electrical current output was monitored by connecting TEG I and TEG II to the ground and signal lines, respectively. When Al is dragged toward PU, it tends to neutralize the positively charged PU surface by supplying electrons (the upper peaks of Figure 3.3c). When the Al then moves toward PI, it withdraws electrons from the negatively charged PI layer (bottom peaks of Figure 3.3c). A positively charged PU and negatively charged PI surfaces are therefore formed through their frictional contact with PDMS, and due to the triboelectric series (Figure 3.3a), the PDMS and PU become fully saturated

with electrons and holes, respectively. Consequently, as the electron-saturated PDMS slides toward PI, they share electrons (i.e. electrons move from PDMS to PI), but it still remains more negative. The amount of charge transferred remains much the same regardless of the direction of flow (Figure 3.3d).

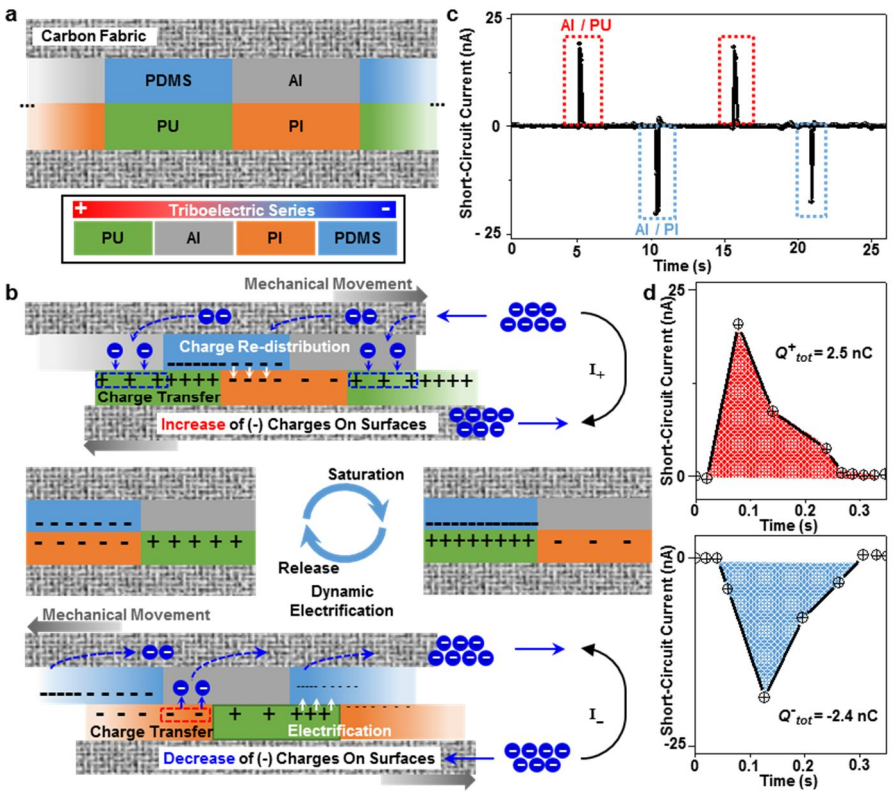

Figure 3.3 Overview of the TEG mechanism. a) Schematic illustration of the side of a TEG (top) and the triboelectric series of its four constituent materials according to their tendency to gain or lose electrons through the triboelectric effect (bottom). b) Schematic diagram of the electricity generation process by rubbing. Al is employed to neutralize charged surfaces of polymers (PU and PI), and PDMS is utilized for electrification of polymers (PU and PI). c) The electrical current generated by rubbing a TEG at 5-second intervals. d) Enlarged views of the positive (top) and negative (bottom) current peaks in Figure 3.3b.

This was confirmed through control experiments, in which only the height of the materials, and therefore the distance between the two fabrics, was varied (Figures 3.4 and 3.5).

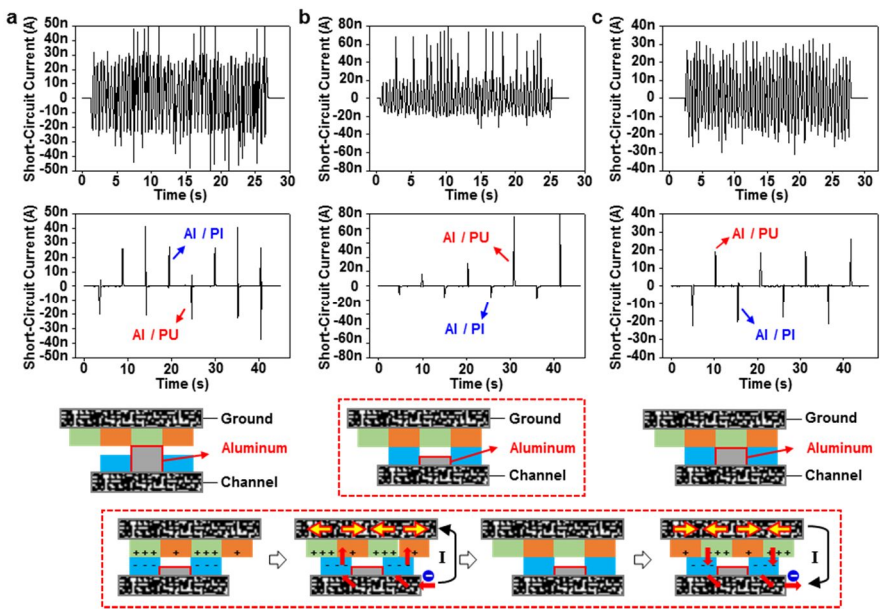

Figure 3.4 Short-circuit current generated by continuous rubbing (top row) or discrete rubbing (mid row) of TEGs with an Al layer thickness of: a) 0.4 mm, b) 0.1 mm, and c) 0.2 mm. All other polymers (PDMS, PU and PI) have a thickness of ~0.2mm. The bottom row depicts schematic illustrations of the control experiment. For convenience, the upper and lower TEGs are named as TEG I and TEG II, respectively

The height of the Al layer was manipulated to control the intimate contact between it and the polymer layers of PU or PI. As shown in Figure 3.4, this inmate contact proved to be a key factor in determining the polarity of the current output, and therefore cannot be fully explained by previously described working mechanisms that rely solely on electrostatic induction[10,11,15]. In the case of Figure 3.4a, in which only the Al makes contact with the polymers of TEG I during rubbing, the Al tends to deliver or withdraw electrons onto PI and PU, respectively, by the triboelectric effect. The PDMS covered area of the carbon fabric also drives electrons back and forth by electrostatic induction, along with the electrification of Al. Note that unusual current outputs with both positive and negative peaks were frequently observed, which can be explained by free electrons in Al. Thus, when the Al induces a triboelectric charge in the polymers in TEG I, it may also give or take back electrons. The resultant short-period between electrification and neutralization may in turn result in ambipolar current peaks.

When it is only PDMS that contacts with the polymers of TEG I (Figure 3.4b), the polarity of the current output is inversed. This can be explained by the sum of two kinds of current induction. 1) Electrostatic induction, which is induced by contact/release behaviors of PDMS during rubbing. When the negatively charged PDMS is dragged from PU to PI, PU that expose to the air lose the negative circumstances (release) while PI gain the negative circumstances (contact). Due to this contact/release is induced by same PDMS, the amount of induced current is equal and the direction of induced currents are contrary to each other which made

the total zero output current. 2) Dynamic electrification, which is induced by friction between PDMS and polymers of TEG I as shown in Figure S2b bottom. When PDMS electrified by PU which causes electrons to flow back in the bottom fabric while PI caused electrons to flow forward in the upper fabric. Sudden peaks in Figure 3.4b explained by a discharge of saturated charges on the polymer surface and the unstable structure of the TEG due to the air gap generated by the flexible substrate.

Finally, when both the PDMS and Al make intimate contact with the polymers of TEG I (Figure 3.4c), the current peaks show an identical flow regardless of the direction, as was previously mentioned at Figure 3.3.

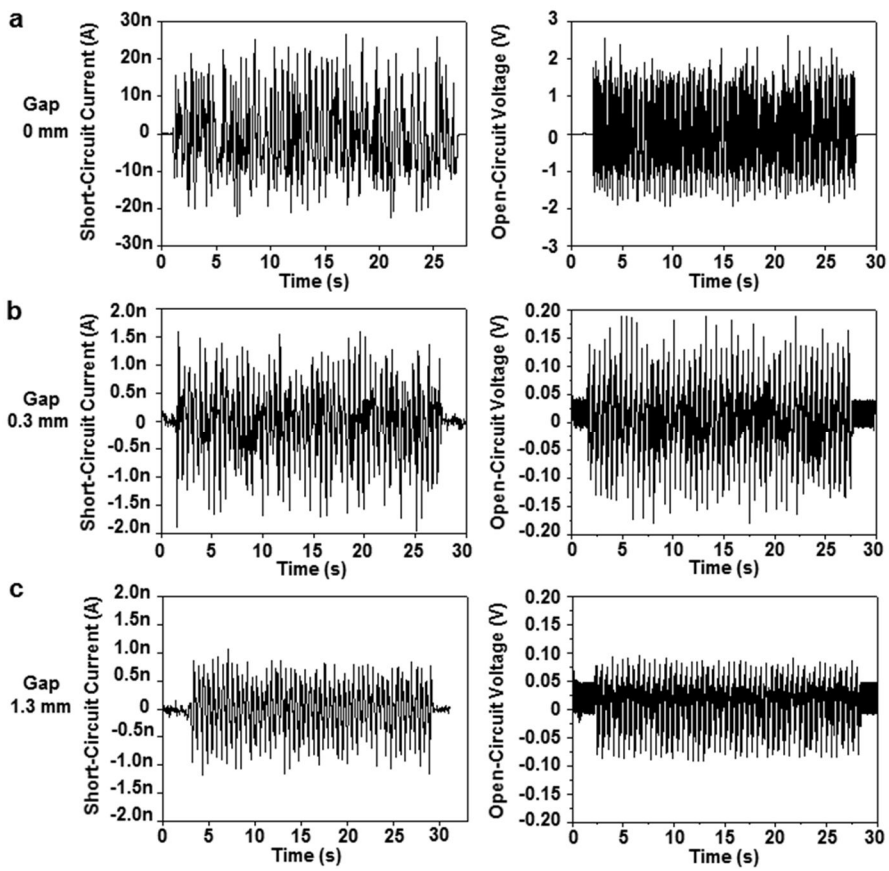

Figure 3.5 Overview of the TEG mechanism. a) Schematic illustration of the side of a TEG (top) and the triboelectric series of its four constituent materials according to their tendency to gain or lose electrons through the triboelectric effect (bottom). b) Schematic diagram of the electricity generation process by rubbing. Al is employed to neutralize charged

The distance between the two TEGs was adjusted to set values of 0 mm (intimate contact, Figure 3.5a), 0.3 mm (Figure 3.5b) and 1.3 mm (Figure 3.5c). The fact that both the short-circuit current (I_{sc}) and the open-circuit voltage (V_{oc}) were dramatically reduced with increasing gap indicates that the dynamic electrification of PDMS and neutralization of Al played significant roles in this structure. It therefore may not be explained solely by previously reported electrostatic induction mechanisms.

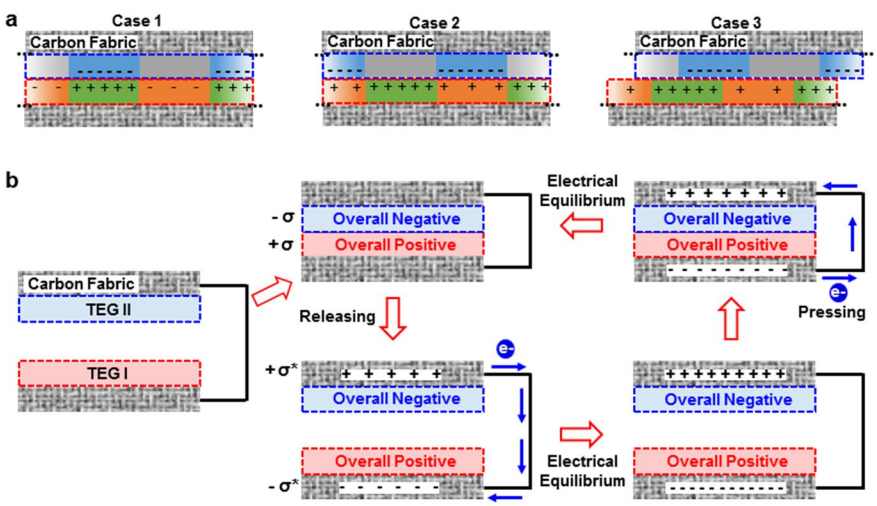

Figure 3.6 a) Case 1: PDMS contacts only with PU. Case 2: PDMS contacts only with PI. Case 3: PDMS contacts with both PU and PI. b) Schematic diagram showing the process by which electricity is generated through contact/release.

TEG I and II consisted of two different pairs of material, giving four different materials in total. This means that random human motions have the potential to generate three distinct combinations of contact between different materials: PDMS with PU, PI, or both (Figure 3.6a). According to the triboelectric series, the TEG I layer should always be positively charged, and the TEG II layer negatively charged, although the amount charge is not constant. Given that Al is conductive and directly adhered to the CF electrode, it can be assumed that it plays a limited role at most in inducing static electricity. Consequently, in Case 1, the PDMS of TEG II gains electrons, the PU of TEG I loses electrons and the PI of TEG II gain electrons. Although the electron transfer in PU conflicts with that in PI, the number of electrons lost from PU is still greater than those gained from PI. In Case 2, the PDMS of TEG II gains electrons, while both the PU and PI of TEG I lose electrons. Finally, in Case 3, the PDMS of TEG II gains electrons from both PU and PI, the PU of TEG I loses electrons to PDMS and Al, and the PI of TEG II both loses electrons to PDMS and gains them from Al. Thus, although PI loses and gains electrons from different materials at the same time, the overall change in PU remains greater than that of PI. Each individual layer of the TEG can therefore have either a positive or a negative charge, regardless of the overall surface charge.

Figure 3.6b schematically depicts the sequence of operation in relation to vertical friction. In the initial state, no charge has yet been induced, and so there is zero electric potential (EP) difference between the top and the bottom TEG surface. The two TEGs are then brought into contact with each other, and their surface

charges are transferred due to the triboelectric effect. At this state, the net EP change (-σ + +σ) is zero, but when the TEGs are separated, the mechanical contact is effectively eliminated between the surfaces and it creates an EP difference between the two electrodes. This causes an electrical current to flow, until each layer reaches electrical equilibrium. Finally, the TEGs are again brought into contact, generating an EP difference between the two electrodes and creating a current flow until a new electrical equilibrium is reached (i.e., a return to the initial state)[10,11,15].

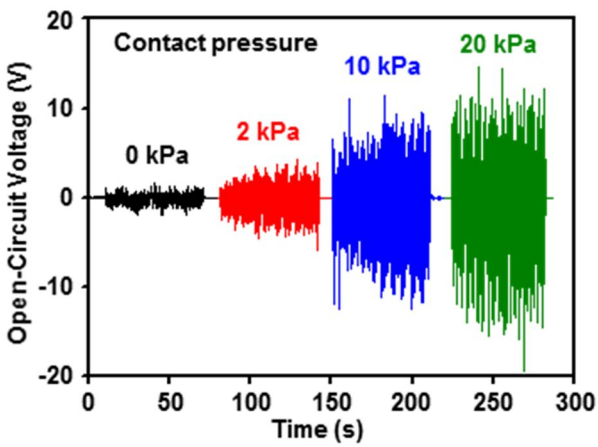

Figure 3.7 Open-circuit voltage generated by continuous rubbing of TEGs with applied pressure for making intimate contact between TEGs.

To characterize the performance of the TEG, I_{sc} and V_{oc} were measured at the moderate rubbing speed of 3 cm/s, which is analogous to the swing speed of the upper part of the arm near the armpit at normal walking pace. A weight of 200 g was placed on top of the TEG in sliding operation to make the intimate contact between TEG I and II (Figure 3.7). PDMS whose mixing ratio of prepolymer : curing agent is 10 : 1 was used to prevent friction damages (Figure 3.8). The dimension of each stripe was determined as 0.14 mm thick, 5 mm wide, and 15 mm long for high performances (Figures 3.9 and 3.10). As shown in Figures 3.11a and b, I_{sc} exhibits a proportional relationship to the number of repeated lines of material used in fabricating the TEG (6 line: 23 nA, 12 line: 43 nA, 18 line: 55 nA). Furthermore, although V_{oc} increases up to 6 V, it becomes stagnant as the area increases beyond 12 lines possibly due to the input impendence of the measurement system. When subjected to contact/release friction, all TEGs with the same surface area generated an electrical current of ~130 nA and a voltage output of ~15 V (Figures 3.11c and d). This AC output was converted to DC via the rectifying diode, and the accumulated current during rubbing (Figure 3.12a) and contact/release (Figure 3.12b) were plotted. This shows that although the peak value of I_{sc} induced by rubbing is not as regular as that of contact/release friction, the accumulated current exhibits a linear increase under both modes due to the similarity of the integrated area of each peak (Figures 3.12c and d).

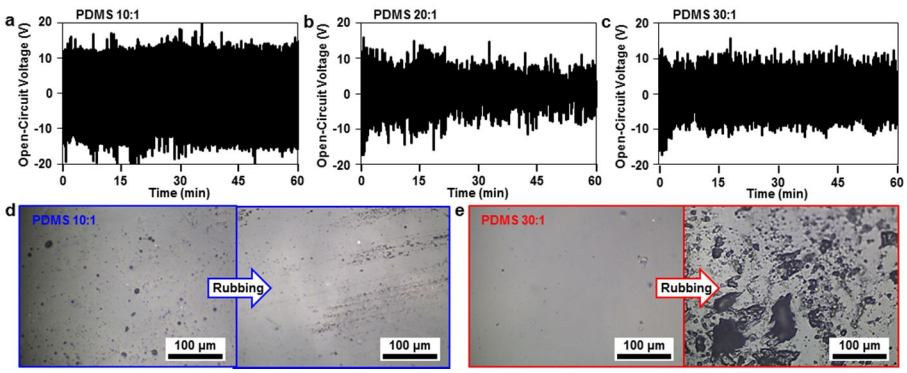

Figure 3.8 Open-circuit voltages obtained with varying the ratio of PDMS a) 10:1, b) 20:1, c) 30:1. Optical images of the surface of PDMS d) 10:1 and e) 30:1 (left: before rubbing, right: after rubbing).

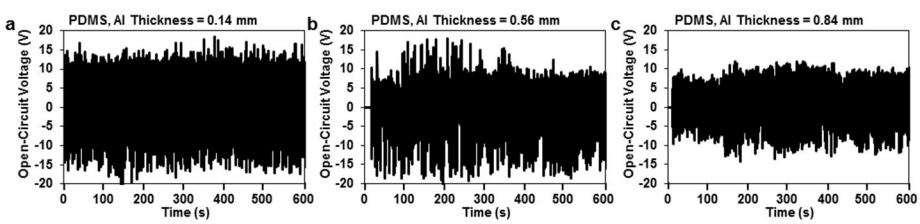

Figure 3.9 Open-circuit voltage generated by different thickness of the PDMS and Al of TEG II. a) 0.14 mm, b) 0.56 mm, and c) 0.84 mm.

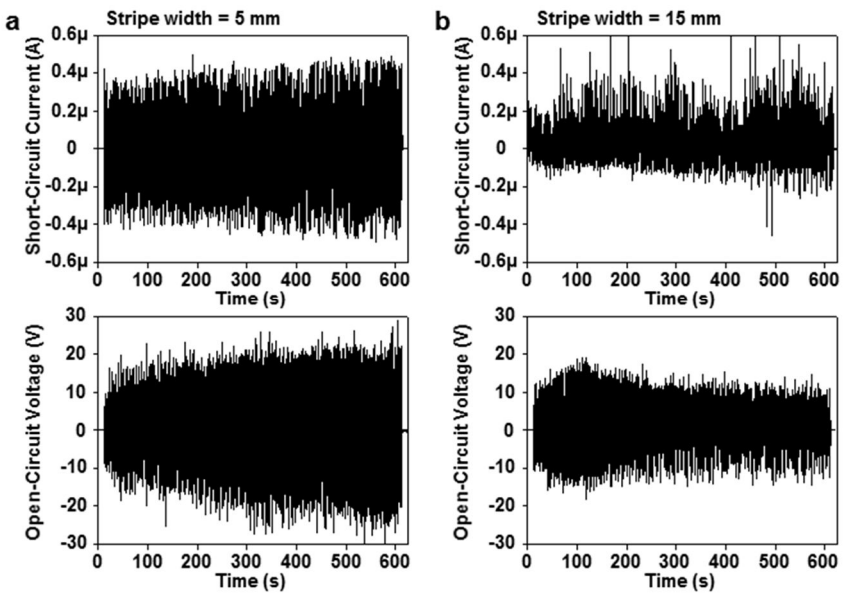

Figure 3.10 Short-circuit current and open-circuit voltage generated by different stripe width of TEGs. Each line have a) 5 mm width and b) 15 mm width.

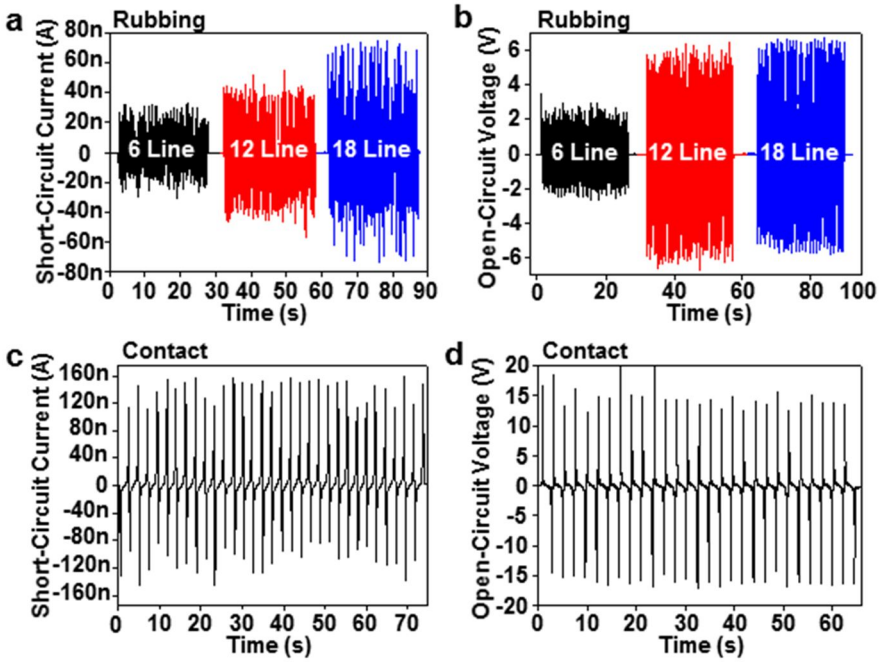

Figure 3.11 a) Short-circuit current, and b) open-circuit voltage generated by different working areas of the TEG (1.5 cm × 3 cm, 1.5 cm × 6 cm, and 1.5 cm × 9 cm, respectively). c) Short-circuit current, and d) open-circuit voltage induced by contact.

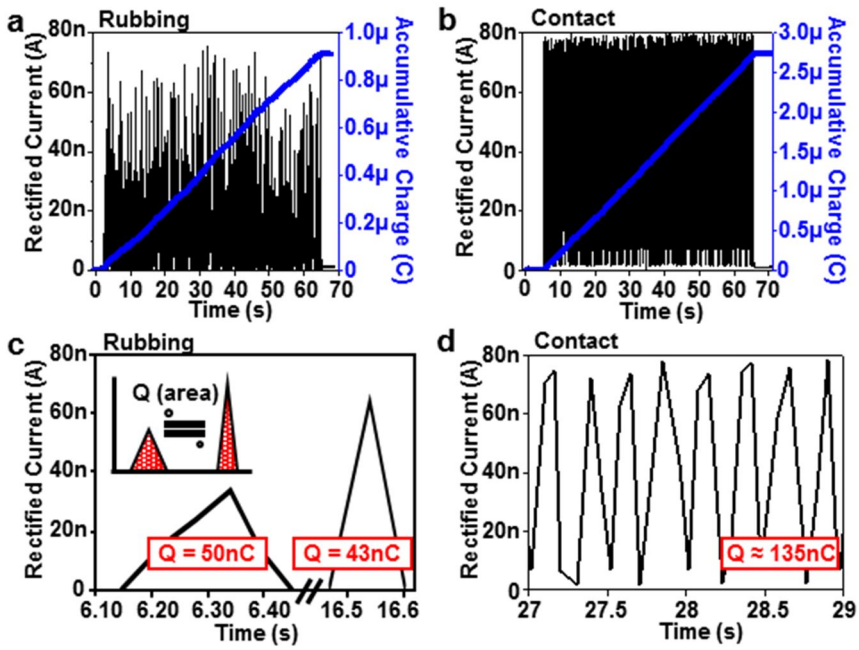

Figure 3.12 Rectified current and accumulative charge generated by a) rubbing and b) contact. c) Enlarged view of the peaks from Figure 3.12a and d) Figure 3.12b. (Note: The TEG has a size of 9 cm × 1.5 cm).

Figures 3.13 show a schematic illustration (left) and series of scanning electron microscopy (SEM) images (right) of the fabrication procedure used to create these SC electrodes. In this, single-wall CNTs are first synthesized on a woven fabric of carbon fibers through chemical vapor deposition, using an electron-beam-evaporated iron catalyst layer (Figure 3.13a). The vertical growth of the CNTs (Figure 3.13b) creates a 30–40 μm high CNT forest that maximizes the surface area for the electrical double-layer. Subsequent electrochemical deposition of RuO_2 nanoparticles onto these CNTs creates a pseudocapacitive effect (Figures 3.13c and d)[23,24], with these RuO_2 particles examined by transmission electron microscopy (TEM, Figure 3.13d right) and energy dispersive spectroscopy (EDS, Figure 3.14c).

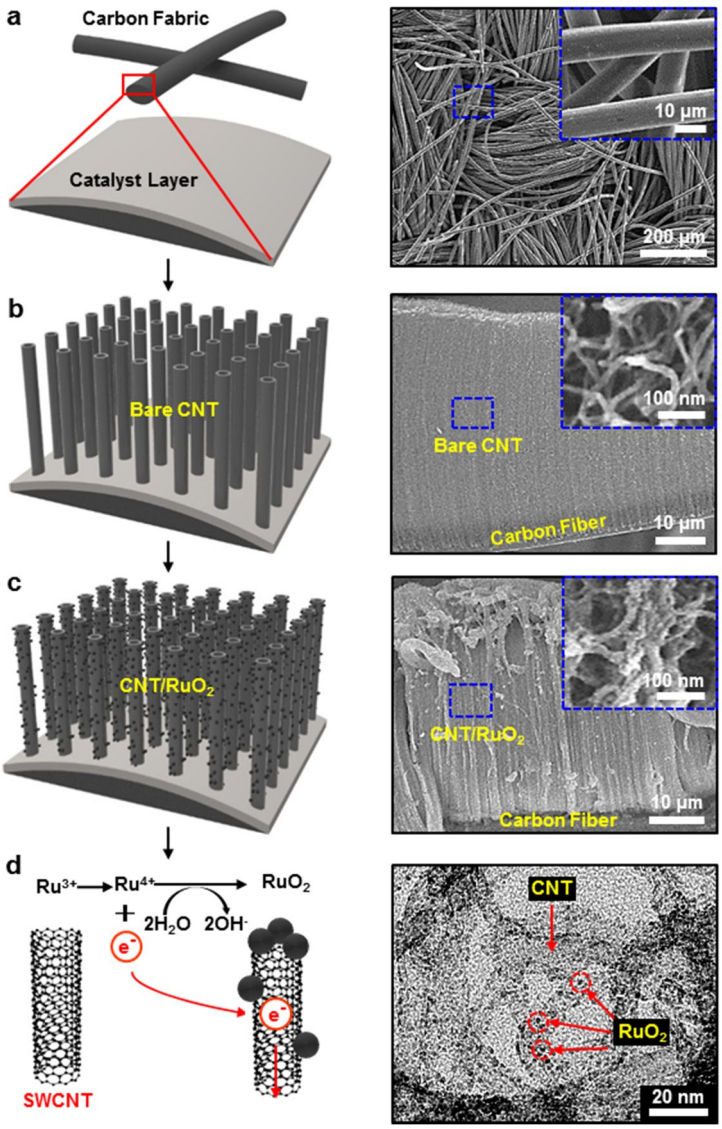

Figure 3.13 Structure of the SC. Schematic illustrations and SEM images of a) CF, b) vertically aligned CNT grown on CF, and c) RuO_2 electroplated CNT. d) Schematic illustration and TEM image of the RuO_2 electroplating.

The areal capacitance of the SC was found to be proportional to both the CNT length (Figure 3.14a), and the amount of RuO_2 electroplating (Figure 3.14b). Furthermore, the CV curves obtained at scan rates of between 5 and 100 mV/s (Figure 3.15a) reveal a quasi-rectangular shape of typical SCs. From the Galvanostatic charge-discharge (GV) curves shown in Figure 3.15b, the areal capacitances at current densities of 10, 5, 2, and 1 mA/cm^2 were calculated to be 74.6, 80.0, 85.2, and 87.9 mF/cm^2, respectively. Note that since the gel electrolyte used was water-based, the potential window was limited to 0.8 V to prevent any damage being incurred by H_2 generation. Both the potential window (in series) and the total capacitance (in parallel) could be easily controlled by connecting multiple SCs (Figure 3.16a); Figure 3.16b demonstrates two SCs in series or in parallel double either the potential limit or capacitance, respectively. The performance of the SC can be seen to remain unchanged up to 135° of bending (Figures 3.17a-d), and 70 kPa of external pressure (Figure 3.18), which is attributed to the high flexibility and mechanical durability of its individual components. Furthermore, only very minor variation is observed in the areal capacitance, even after four thousand charge-discharge cycles (Figure 3.17d).

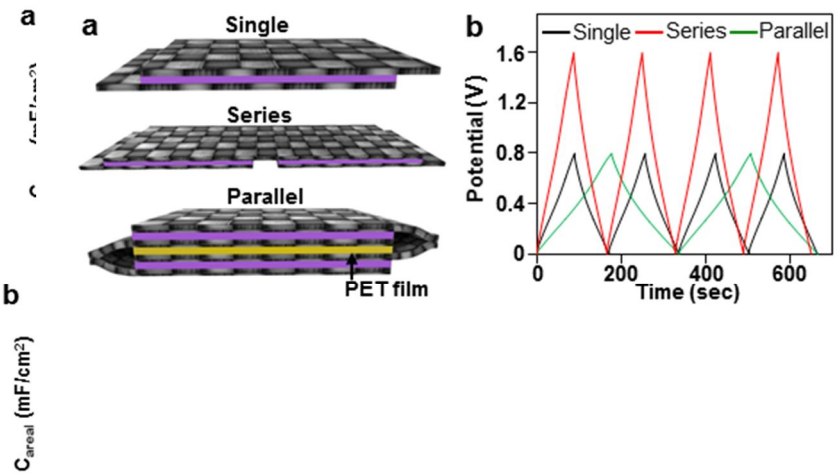

Figure 3.14 The dependence of areal capacitance on a) CNT length and b) RuO_2 electroplating amount. c) EDS measurement of RuO_2 plated CNT.

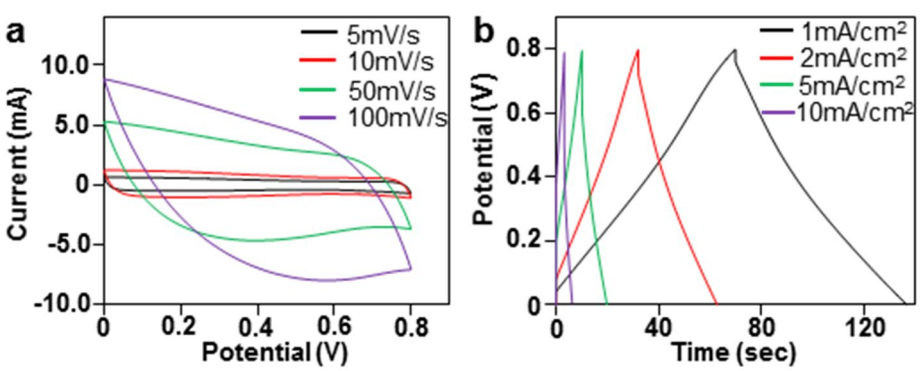

Figure 3.15 a) Cyclic voltammetry curves at different scan rates. b) GV curves at different current densities.

Figure 3.16 a) Schematic illustrations of SCs with different connections, and b) their GV curves.

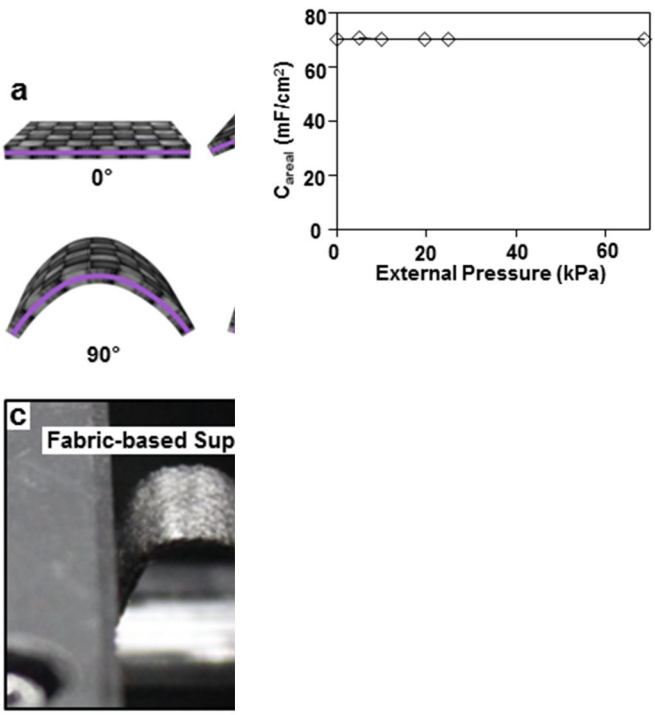

Figure 3.17 a) Schematic illustrations of SCs at different bending angles, b) their GV curves, and c) a digital photo. d) Cycle life test results.

Figure 3.18 External pressure was applied to the wearable SC by placing a weight

on top of it during its capacitance measurement.

The fully integrated wearable energy device is shown in Figure 3.19. In this, the fabric-based TEGs (5 cm x 9 cm, 18 lines) and SCs are easily sewn into commercial clothing items, such as a shirt, and then connected by conductive carbon threads (Figure 3.19a). The energy harvest through regular daily activities such as running and walking was simulated by rubbing the TEGs at various speeds. At a speed of 1.5 Hz, the average output voltage and the rectified current were measured as 33 V and 0.25 μA (Figures 3.19b and c, respectively); the generated electricity stored in SCs was powerful enough to light up a LED (Figure 3.20). The frequency of rubbing determines the slope of charge accumulation, exhibiting a proportional relationship within a range of 0.67–4 Hz (Figures 3.19d and 3.21). This allows the device to function as a wearable self-powered human activity monitor. Figure 3.22 shows the rectified output current (black, left axis) and the charge accumulation (red, right axis) recorded from a subject simulating normal jogging procedures of stretching, walking, running, sprinting, and a cool-down walk. Thus, if the slope of the charge accumulation is monitored, then the activity of the subject wearing the integrated devices can be tracked. For instance, the slope associated with stretching, walking, running, sprinting, and cool-down are 0.48, 8.4, 22, 53 and 9.6 nC/s, respectively. Figure 3.25 shows voltage versus time plots of three different capacitors with capacitances of 1, 10 and 100 nF. Although a fast charging/discharging capacitor (1 nF) offers the better sensitivity for human

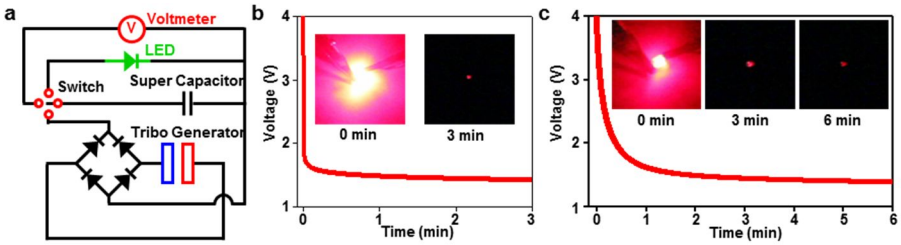

activity monitoring, a high-capacitance capacitor (100 nF) is well suited to long-term monitoring.

Figure 3.19 Demonstration and measurement of electrical signals of the energy supply devices. a) Image of the devices applied to a knit shirt and connected by

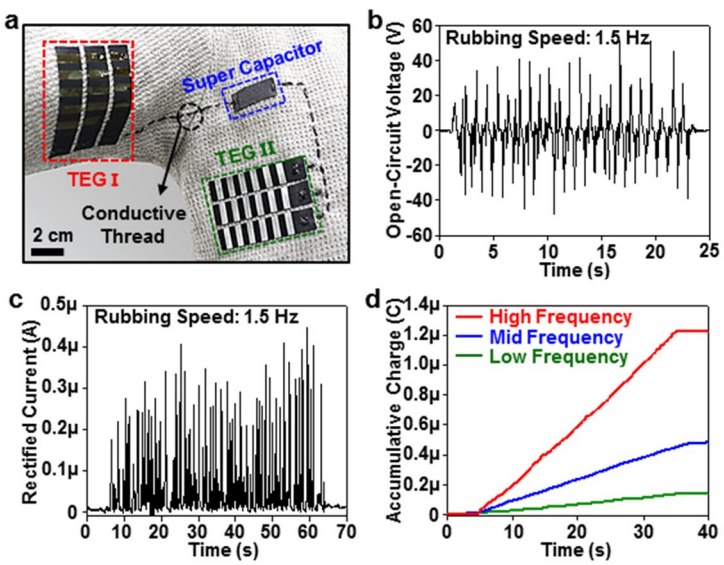

conductive thread (TEG size: 1.5 cm x 6 cm). b) Open-circuit voltage, and c) rectified current generated by the TEG from arm swings. d) The generated charge accumulation from TEG at different frequencies

Figure 3.20 a) Schematic diagram of an electric circuit in which the SC is fully charged by the TEG and is used to power a commercial LED: b) without a resistor,

or c) with a 1 kΩ resistor. The two graphs show the voltage change in the SC over time.

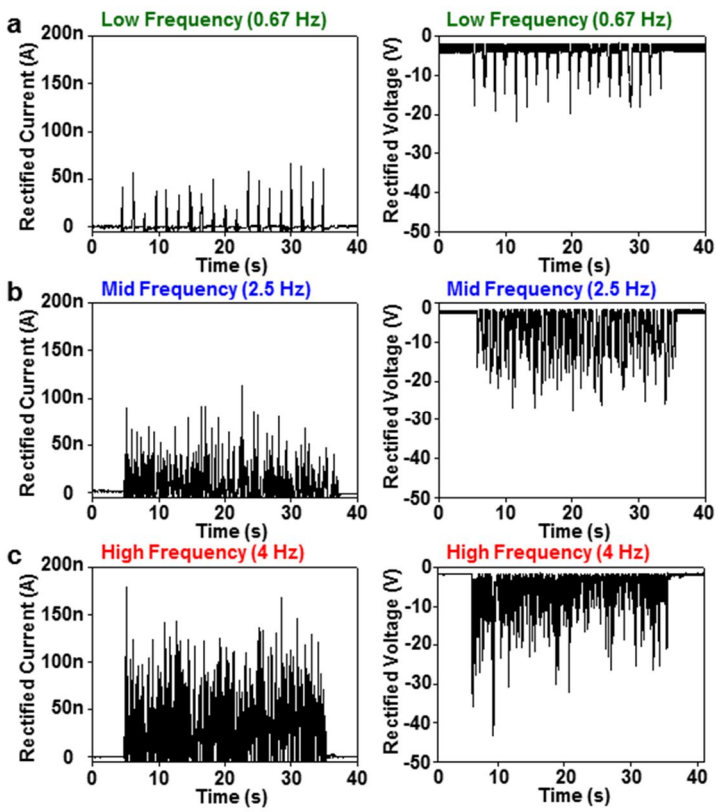

Figure 3.21 Rectified current and rectified voltage at a) low frequency (0.67 Hz), b) mid frequency (2.5 Hz), and c) high frequency (4 Hz)

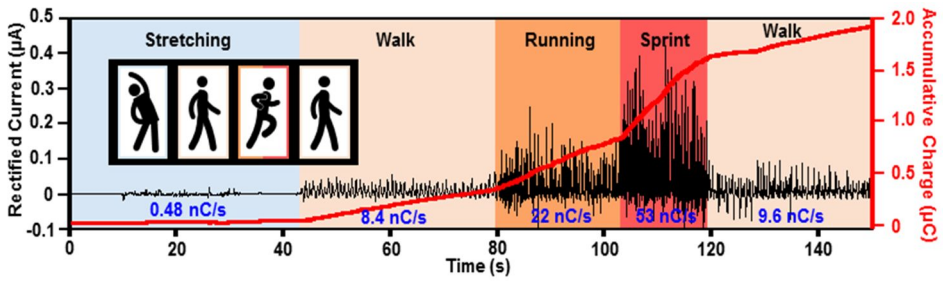

Figure 3.22 Demonstration of the human activity sensor. The generated electricity was recorded during the illustrated jogging procedures.

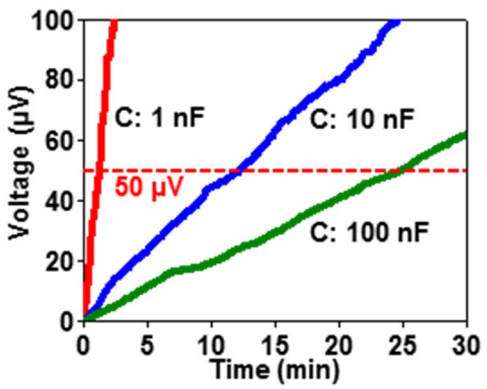

Figure 3.23 Charging of capacitors with various capacitances by TEG.

In addition to monitoring the activity, the SCs charged by TEGs can also supply power to other sensors. To demonstrate this, SCs charged by the TEGs were used to provide the necessary current to a pressure sensor (Figure 3.24a). This pressure sensor consists of a porous pressure-sensitive rubber (PPSR) sandwiched between CFs (Figures 3.24b-g).[28] Its resistance changes linearly with applied pressure (Figures 3.25a and b). In the PPSR, a random network of multi-wall CNT forms electrically conducting paths. The applied pressure changes the morphology of the rubber and disconnects part of conducting paths. By measuring the change in current, it is possible to determine the applied pressure. This was demonstrated by placing 20, 50, 100 and 200 g weights on the sensor (Figure 3.25c). The baseline drift due to the gradual decrease in current supplied by the SC was adjusted by the software (Figures 3.25d and e).

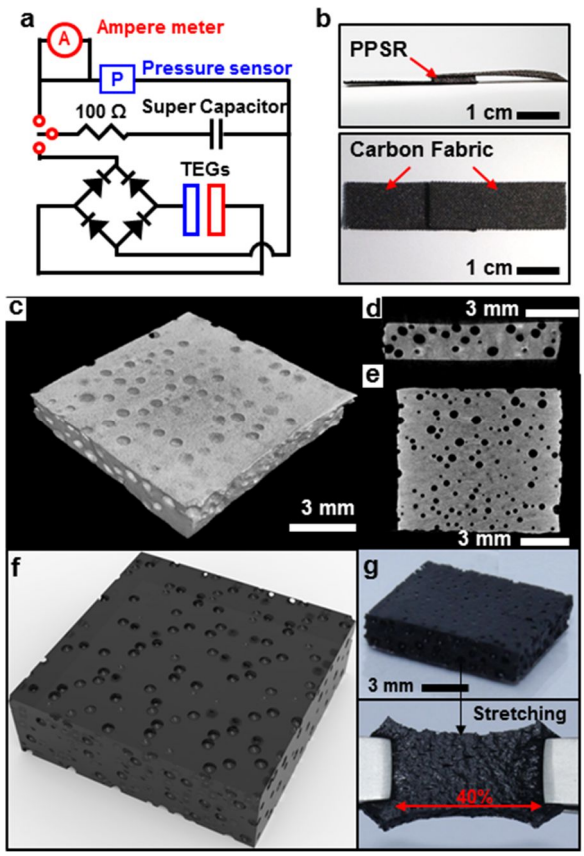

Figure 3.24 a) Electric circuit diagram for the pressure sensor. b) Digital photo of the pressure sensor. Side view (top), top view (bottom). Micro-computed tomography (μ-CT) images. c) 3D view, d) side view and e) top view. f) Schematic illustration of PPSR film. g) Images of PPSR film (top) and stretched PPSR film (bottom).

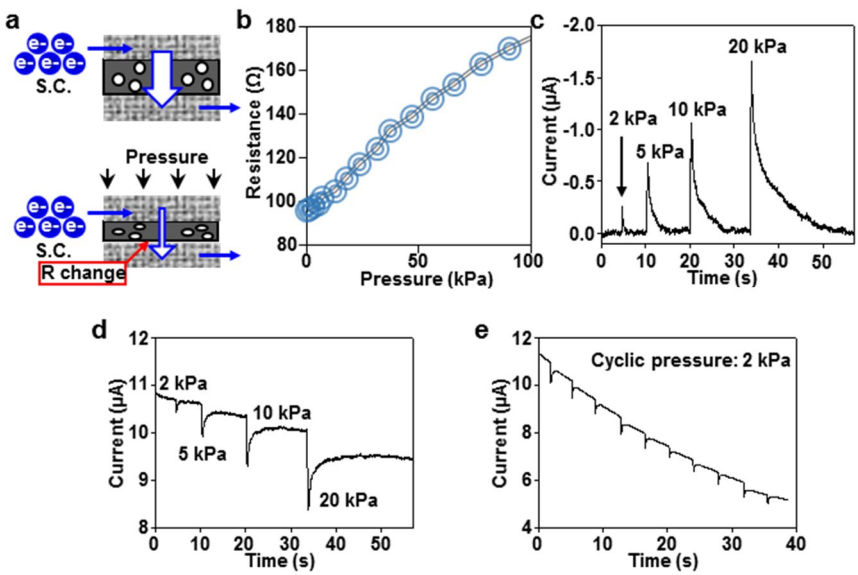

Figure 3.25 a) Schematic diagram of the pressure sensing mechanism. Original state (top), under pressure (bottom). b) Resistance change of the pressure sensor. c) Change Current in the SC as a function of the pressure applied to the pressure sensor. d) Pre-processed current change graph of Figure 3.25c. e) Current change from SC under cyclic pressure (2 kPa) on pressure sensor.

3.4 Conclusion

The wearable integrated energy device proposed by this study is capable of harvesting and storing the energy generated through human activity. This can be used not only to monitor such activity but also to provide power to external sensors or devices. The TEG component has a unique structure made from four different materials that eliminates the need for air gaps. Furthermore, it is capable of generating electricity through both horizontal and vertical friction, with an average output power density of ~0.18 $\mu W/cm^2$ at 1.5 Hz (typical conditions of running). Compared to other TEGs that used electrostatic generation, the wearable TEGs show the low output power because its power generation depends on the dynamic electrification. Therefore, its performance can be improved by further studies in developing novel fabrication processes and structures that employ the electrostatic generation. The performance of the SC is enhanced by using vertical CNTs/RuO_2 nanoparticles on CF electrodes with the resulting capacitance of 85.2 mF/cm^2 at the discharging current of 1 mA/cm^2. Also the excellent durability (stable up to 4,000 charge-discharge cycles) matches well with the wearable power generation through TEGs. These provide new insight into the future development of wearable electronic systems.

References

[1] D.-H. Kim, N. Lu, R. Ma, Y.-S. Kim, R.-H. Kim, S. Wang, J. Wu, S. M. Won, H. Tao, A. Islam, K. J. Yu, T. Kim, R. Chowdhury, M. Ying, L. Xu, M. Li, H.-J. Chung, H. Keum, M. McCormick, P. Liu, Y.-W. Zhang, F. G. Omenetto, Y. Huang, T. Coleman, J. A. Rogers, *Science* **2011**, *333*, 838.

[2] W.-H. Yeo, Y.-S. Kim, J. Lee, A. Ameen, L. Shi, M. Li, S. Wang, R. Ma, S.H. Jin, Z. Kang, Y. Huang, J.A. Rogers, *Adv. Mater.* **2013**, *25*, 2773.

[3] M. Kaltenbrunner, T. Sekitani, J. Reeder, T. Yokota, K. Kuribara, T. Tokuhara, M. Drack, R. Schwodiauer, I. Graz, S. B.-Gogonea, S. Bauer, T. Someya, *Nature* **2013**, *499*, 458.

[4] T. Someya, Y. Kato, T. Sekitani, S. Iba, Y. Noguchi, Y. Murase, H. Kawaguchi, T. Sakurai, *Proc. Natl. Acad. Sci. USA* **2005**, *102*, 12321.

[5] D. J. Lipomi, M. Vosgueritchian, B. C-K. Tee, S. Hellstorm, J. A. Lee, C. H. Fox, Z. Bao, *Nat. Nanotechnol.* **2011**, *6*, 788.

[6] C. Wang, D. Hwang, Z. Yu, K. Takei, J. Park, T. Chen, B. Ma, A. Javey, *Nat. Mater.* **2013**, *12*, 899.

[7] D. Son, J. Lee, S. Qiao, R. Ghaffari, J. Kim, J. E. Lee, C. Song, S. J. Kim, D. J. Lee, S. W. Jun, S. Yang, M. Park, J. Shin, K. Do, M. Lee, K. Kang, C. S. Hwang, N. Lu, T. Hyeon, D.-H. Kim, *Nat. Nanotechnol.* **2014**, *9*, 397.

[8] S. Feng, R. Caire, B. Cortazar, M. Turan, A. Wong, A. Ozcan, *ACS Nano* **2014**, *8*, 3069.

[9] C. Dagdeviren, B. D. Yang, Y. Su, P. L. Tran, P. Joe, E. Anderson, J. Xia, V. Doraiswamy, B. Dehdashti, X. Feng, B. Lu, R. Poston, Z. Khalpey, R. Ghaffari, Y. Huang, M. J. Slepian, J. A. Rogers, *PNAS* **2014**, *111*, 1927.

[10] C. Zhang, W. Tang, C. Han, F. Fan, Z. L. Wang, *Adv. Mater.* **2014**, 26, 3580.

[11] J. Chen, G. Zhu, W. Yang, Q. Jing, P. Bai, Y. Yang, T.-C. Hou, Z. L. Wang, *Adv. Mater.* **2013**, *25*, 6094.

[12] J. Zhong, Y. Zhang, Q. Zhong, Q. Hu, B. Hu, Z. L. Wang, *ACS Nano* **2014**, 8, 6273

[13] S. Kim, M. K. Gupta, K. Y. Lee, A. Sohn, T. Y. kim, K.-S. Shin, D. Kim, S. K. Kim, K. H. Lee, H.-J. Shin, D.-W. Kim, S.-W. Kim, *Adv. Mater.* **2014**, 26, 3918

[14] S. Wang, L. Lin, Yannan Xie, Q. Jing, S. Niu, Z. L. Wang, *Nano Lett.* **2013**, *13*, 2226.

[15] G. Zhu, J. Chen, Y. Liu, P. Bai, Y. S. Zhou, Q. Jing, C. Pan, Z. L. Wang, *Nano Lett.* **2013**, *13*, 2282.

[16] P. Bai, G. Zhu, Y. Liu, J. Chen, Q. Jing, W. Yang, J. Ma, G. Zhang, Z. L. Wang, *ACS Nano* **2013**, *7*, 6361.

[17] G. Zhu, J. Chen, T. Zhang, Q. Jing, Z. L. Wang, *Nat. Commun.* **2014**, *5*, 3426.

[18] G. Zhu, Y. S. Zhou, P. Bai, X. S. Meng, Q. Jing, J. Chen, Z. L. Wang, *Adv. Mater.* **2014**, *26*, 3788.

[19] L. Hu, M. Pasta, F. L. Mantia, L. Cui, S. Jeong, H. D. Deshazer, J. W. Choi, S. M. Han, Y. Cui, *Nano Lett.* **2010**, *10*, 708.

[20] Y. J. Kang, S.-J. Chun, S.-S. Lee, B.-Y. Kim, J. H. Kim, H. Chung, S.-Y. Lee, W Kim, *ACS Nano* **2012**, *6*, 6400.

[21] X. Xiao, T. Li, P. Yang, Y. Gao, H. Jin, W. Ni, W. Zhan, X. Zhang, Y. Cao, J. Zhong, L. Gong, W.-C. Yen, W. Mai, J. Chen, K. Huo,Y.-L. Chueh, Z. L. Wang, J. Zhou, *ACS Nano* **2012**, *6*, 9200.

[22] P. Simon, Y. Gogotsi, *Nat. Mater.* **2008**, *7*, 845.

[23] J. R. Miller, P. Simon, *Science* **2008**, *321*, 651.

[24] X. Yang, C. Cheng, Y. Wang, L. Qiu, D. Li, *Science* **2013**, *341*, 534.

[25] Y. Qi, M. C. McAlpine, *Energy Environ. Sci.* **2010**, *3*, 1275.

[26] J.-S. Ye, H. F. Cui, X. Liu, T. M. Lim, W.-D. Zhang, F.-S. Sheu, *Small.* **2005**, *1*, 560.

[27] H. Zhang, G. Cao, Z. Wang, Y. Yang, Z. Shi, Z. Gu, *Nano Lett.* **2008**, *8*, 2664.

[28] S. Jung, J. H. Kim, J. Kim, S. Choi, J. Lee, I. Park, T. Hyeon, D.-H. Kim, *Adv. Mater.* **2014,** 26, 4825.

Chapter 4. Stretchable Triboelectric Generators for Integrated Wearable Fall Detector.

4.1 Introduction

Falls often cause severe health-risking consequences particularly for elder generations. Impacts due to falls fracture bones and sometimes cause the internal bleeding. Unconsciousness that possibly accompanies with falls may place fatal risks. Therefore needs to detect falls and send immediate alarms wirelessly to nearest emergency clinics exist. However, conventional automatic fall detection systems are featured with rigid, bulky, and heavy power supply systems. These impede the mobility of users during daily lives and give immense discomfort. Recently, wearable devices have received great attentions. Numerous related researches have been reported, such as wearable human-machine-interfaces[1-3], skin-based biomedical devices[4-8], and high sensitivity sensors for artificial skins[9-11]. For high performances, the combination of electronics fabricated on commercial chips[12,13] with stretchable components is efficiently used. Therefore shifting platforms of fall detectors from rigid to soft, stretchable ones enables progresses in the wearability, mobility, and comfort, as well as effective point-of-

care of patients/users. However, the development of stretchable and light-weight wearable power supply systems for fall detectors is still challenging. Even though the stretchable battery for the wearable device has been developed to be wrapped upon the complex curvilinear surfaces of human body conformally, that has not provided enough actuation time due to its thin and small structure. Continuous charging would lengthen the actuation time.[14]

An average-sized human body stores as much chemical energy as a 1000-kg battery, and about 25% of the energy is possibly exploited mechanically[15] that generates friction. This unlabored energy is sufficient enough to operate the wearable devices when it is converted to electrical energy.[16-18] Therefore, triboelectric generator (TEG) which generates electrical energy through friction is regarded as the suitable energy supplier to the wearable batteries[16]. For this purpose, TEGs, a wearable electrical generator, have been integrated on clothes.[17,18] However, those TEGs consist of metals and polymers which have different mechanical properties from clothes. In this paper, we fabricated a wrist-band type TEG with Ag-coated conductive Nylon (C-Nylon), which had high stretchability and mechanical properties (e.g., stiffness) of fabrics. Thus, it could be easily stretched and worn on a wrist or integrated on clothes without causing any discomforts. Furthermore, we showed the triboelectric power generation performance is affected by the work function (WF) modification. The electricity that is generated from the TEG steadily charges the commercial micro-battery to elongate its working hours. Furthermore, we demonstrate the wearable fall

detection system incorporated with a 3-axis accelerometer and a wireless communication module which is powered by the wearable power supply system.

4.2 Experimental Section

Fabrication of the TEGs*:* To fabricate TEG I, a piece of C-Nylon (Meditex 130, Sparkfun, Germany) was coated with polyethylenimine ethoxylated (PEIE, Sigma-Aldrich, 80 % ethoxylated solution) solution which was diluted in ethanol (Samchum, 99.9 % anhydrous, Korea) with concentration of 4 ~ 20 % (weight percent). The solution was spread on the C-Nylon and blown by N2 gas, and then dried in the convection oven at 55 °C for 6 hr. The repetition was made up to 6 times. The PEIE coated fabric was tailored and equipped on the clothes by weaving. To fabricate TEG II, Ecoflex (0030 Ecoflex®, Smooth-On, Inc) was coated on a piece of C-Nylon and cured in the convection oven over 4 hr at 70 °C. The Ecoflex coated C-Nylon was bent and then the two ends were pasted up with each other to form the wrist-band shape.

Optical and electrical characterizations methods: The morphologies of the products were characterized by using a digital single-lens reflex camera (Cannon EOS 600D, Japan) and SEM (S-3400N, Hitachi, Japan). The work function of the bare C-Nylon, C-Nylon/PEIE, C-Nylon/Ecoflex, and C-Nylon/PDMS were measured by theta probe base system. All measurements were conducted in the X-ray Photoelectron Spectroscopy (theta probe base system, Thermo Fisher Scientific Co.). Each component was examined at least three times

with different samples. The triboelectricity was measured by following the Korea standard test procedure (KSK 0555) and the stiffness was measured by heart loop test procedure (KSK 0538). The electrical measurements for charging/discharging character were performed with a potentiostat (600E Potentiostat/ Galvanostat, CH Instruments, USA). The electrical current and voltage output were monitored by connecting TEG I and TEG II to the ground line and the signal line, respectively, and by applying contact friction (0.7 Hz).

Acquisition of the vector sum trends for various motions: The detection of fall was realized by a commercial 3-axis accelerometer (LIS344ALH, STMicroelectronics). It featured ± 2 g (gravity) measurement range, low power consumption (~ 700 μA), and 2.4 ~ 3.6 V single supply operation. The accelerometer was powered by the battery charged from the fabricated TEGs. The voltage changes of the signal output terminal representing each axis were recorded by a commercial MCU (Arduino pro mini, Sparkfun). The recorded voltage changes were analyzed and the value of the vector sum was calculated by using the custom-made software embedded in the MCU. This value simultaneously transferred to the external computer via Bluetooth module (BlueSMiRF HID, Sparkfun) connected to the MCU using serial communication protocols. The custom-made LabView based program embedded in the computer received the transferred values. Based on these values, the program plot the graph and save the result for the post processing.

4.3 Result and Discussion

The structural features of the fall detection system and its components are represented in Figure 4.1. As shown in Figure 4.1a, the fall detection system was fabricated by integrating with 3-axis accelerometer and wrist-band type TEG devices. The wearable TEG was fabricated using conductive nylon fabric (C-nylon, Meditex 130, Sparkfun) enabling biaxial stretching. TEG composed of two different electrodes, polyethylenimine ethoxylated (PEIE, Sigma-Aldrich, 80 % ethoxylated solution) coated C-nylon as top electrode and bottom electrode, ecoflex-coated C-nylon. PEIE-coated C-nylon was woven inside of the shirt band in order to allow friction with bottom counterpart Ecoflex-coated C-Nylon by the typical movement of arm. Energy harvesting mechanism of the wrist-band type triboelectric generator depicted schematically in Figure 1b. Top and bottom electrode of TEG are repeatedly contacted and separated by swinging motion of arms. The electrical network diagram of whole fall detection system is shown in Figure 4.1c. The detection of fall is realized by commercial 3-axis accelerometer (LIS344ALH, STMicroelectronics). It features ±2 g, ±6 g measurement range, low power consumption (~700 μA) and 2.4~3.6 V single supply operation. To operate the fall detection system without external power source, the power generated by TEG and stored in battery. The rectifier converts the generated alternating current (AC) into the direct current (DC) to charge the battery. And it supply the power to the accelerometer, microcontroller unit (MCU, Arduino pro mini, Sparkfun) board,

and Bluetooth module (BlueSMiRF HID, Sparkfun), simultaneously. The output voltages representing acceleration of x, y, z direction are applied to the analog input terminals of the MCU board. The custom made software embedded in the MCU calculates vector sum of the 3-axis acceleration and transport these data to the external computer using Bluetooth module via serial communication.

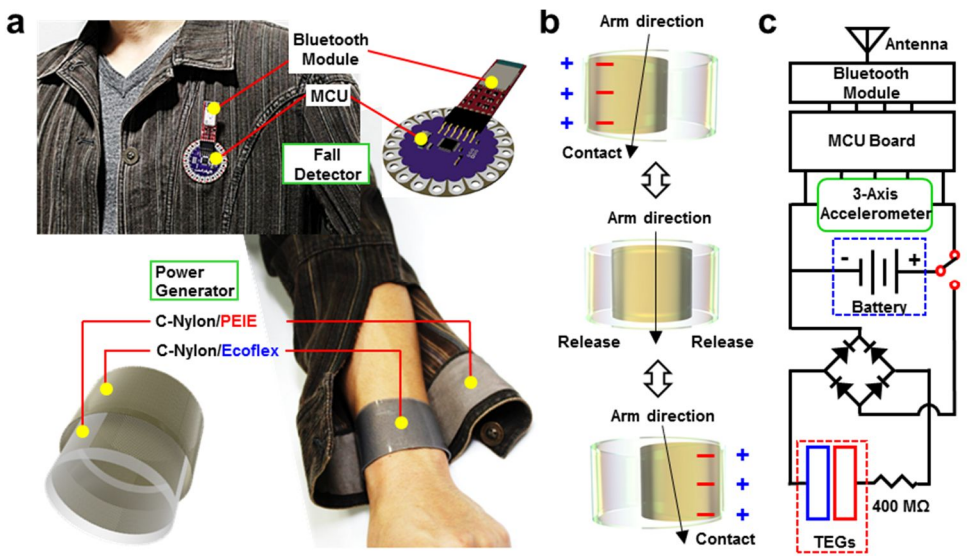

Figure 4.1 Schematic descriptions and morphology of the wearable energy supply system for fall detector. a) Digital photo image of the wrist type C-Nylon/Ecoflex that is worn on the body and C-Nylon/PEIE and the fall detector are equipped upon a jacket. Inset shows the schematic illustration of individual devices. b) Schematic description of the process of electric power generation by TEG. c) Circuit diagram of the wearable fall detect system.

A detailed schematic illustration of TEG is provided in Figure 4.2a. The surface of a pair of TEGs obtains the opposite charge through friction and the quantity of charge is determined by their WF gap (Figure 4.3).[19] To increase the WF gap, one of the C-Nylons was coated with highly negative material (i.e., Ecoflex). Ecoflex is a material having higher WF level (14.07 eV) than PDMS (13.2 eV) thereby Ecoflex-coated C-Nylon generates more triboelectric power than PDMS-coated C-Nylon (Figure 4.4), even though, the PDMS is known as one of the best negative materials as the triboelectric series show. Furthermore, the Ecoflex-coated C-Nylon shows lower modulus and stretchability than the PDMS-coated C-Nylon (Figure 4.5), which makes the Ecoflex a proper material for wearable devices. The other C-Nylon was modified by PEIE which reduced the WF of conductors including metals and polymers due to its intrinsic molecular dipole moments of the neutral amine groups (Figure 4.2b) and the charge-transfer characteristics.[20] The reduction of the WF is caused by physisorption of PEIE and is affected by the coating procedure. To maximize the triboelectricity, the various coating conditions such as the coating cycle number and PEIE concentration (diluted in ethanol) were tested. As shown in Figure 4.6, the thicker coating layer showed a better performance. Sample #1 (single coating with 4 % solution) showed V_{oc} = 47.33 V and I_{sc} = 95.70 nA while sample #5 (6 times of coating with 20 % solution) showed V_{oc} = 65.94 V and I_{sc} = 163 nA. The result of the ultraviolet photoemission spectroscopy (UPS, Figure 4.7) revealed the WF of sample # 6 yielded lower WF (from 9.25 eV to 6.99 eV). The simplified band diagram is

illustrated in Figure 4.7b.

The differences of morphological, chemical and mechanical properties are shown in Figure 4.8a-c. As Figure 4.8a and 4.8b show, C-Nylon has the twisted mesh structure which has the capacity to adsorb and to withstand the stretch by consuming the extra space. The structure ends up minimizing harmful strain on the C-Nylon. Thereby, it can be stretched up to 125 % without any damage and 170 % with minor damage which can be recovered by heat treatment. As the highly magnified SEM images (Figure 4.8b) show, the gaps between the nylon strings (the building unit of C-Nylon) are modified with PEIE. The water contact angle test revealed that the surface property of C-Nylon was changed from hydrophobic to superhydrophilic, which meant the surface was chemically modified (higher surface energy, Figure 4.8c). The triboelectricity was measured by the Korean standard triboelectric voltage measurement test.[21] C-Nylon and C-Nylon/PEIE were rubbed with wool, and their surface voltage were measured. The result revealed that the surface modification increased the triboelectric voltage of C-Nylon up to 3 times (Figure 4.9, left axis). The mechanical property was measured by the Korean standard stiffness measurement test (heart loop method)[22] which revealed that the surface stiffness of C-Nylon was barely changed after the surface modification (Figure 4.9, right axis). To sum up, the surface modification with PEIE enhanced the triboelectric effect without changing the mechanical property of the modified material; it remained soft and fluttery.

As shown in Figures 4.10a and 4.10b, the surface modification increased the

triboelectric power generation performance; V_{oc} increased from 29 V to 66 V, and I_{sc} increased from 78 nA to 159 nA. The electrical current and voltage output were monitored by connecting TEG I and TEG II to the ground line and the signal line, respectively, and by applying contact friction (0.7 Hz). The contact pressure also affected the triboelectric performance which had proportionally increased from 36 V (0.3 kPa) to 104 V (6.7 kPa) with increasing contact pressure (Figure 4.10c). However, the fixed contact pressure of 1.1 kPa, which was analogous to the pressure between the sleeve and the wrist during activities, was applied for the rest of the experiment. The thickness of the Ecoflex layer was fixed to 2 mm because it showed the optimum performance as shown in Figure 4.10d. In Figure 4.10e, the peak power (10.2 μW) was achieved at the load resistance of 400 MΩ. The rectified current and voltage were measured as ~ 190 nA and ~ 75 V, respectively, and the accumulated charge was also plotted (Figure 4.11).

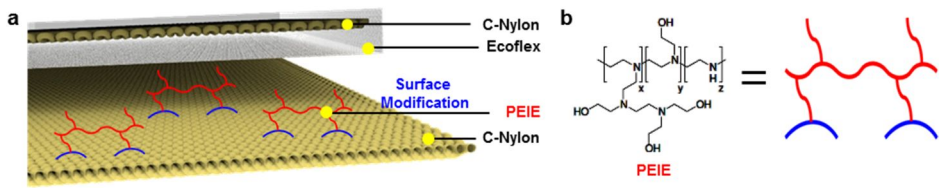

Figure 4.2 The chemical structure of the surface modifier (PEIE) and the Photoemission cutoff obtained via UPS for C-Nylon, C-Nylon/PEIE, and C-Nylon/Ecoflex are shown in the right and left top insets, respectively. The schematic illustration of TEG is shown in the bottom.

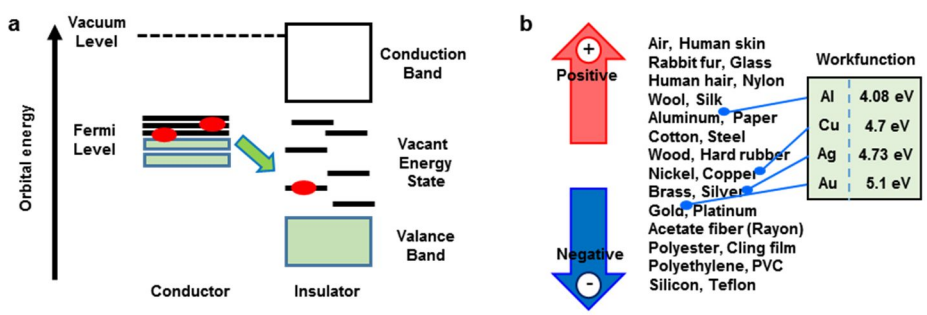

Figure 4.3 a) Contact charge between conductor and insulator. b) Triboelectric series (left) and work function (WF) series (right).

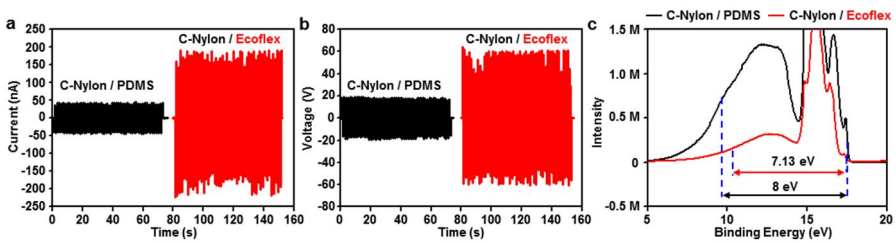

Figure 4.4 The electric power generation comparison of C-Nylon/PDMS with C-Nylon/Ecoflex. a) Short-circuit current and b) open-circuit voltage c) UPS spectrum of C-Nylon/PDMS and C-Nylon/Ecoflex.

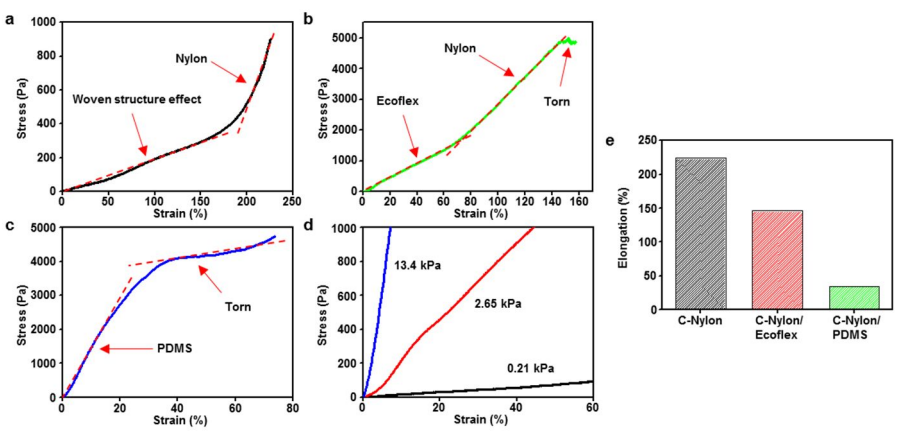

Figure 4.5 The mechanical properties compared bare C-Nylon, C-Nylon/Ecoflex, and C-Nylon/PDMS. The stress–strain curves of a) bare C-Nylon, b) C-Nylon/Ecoflex, c) C-Nylon/PDMS, and its d) Young's modulus. e) Elongation

limitation which determined by the torn point.

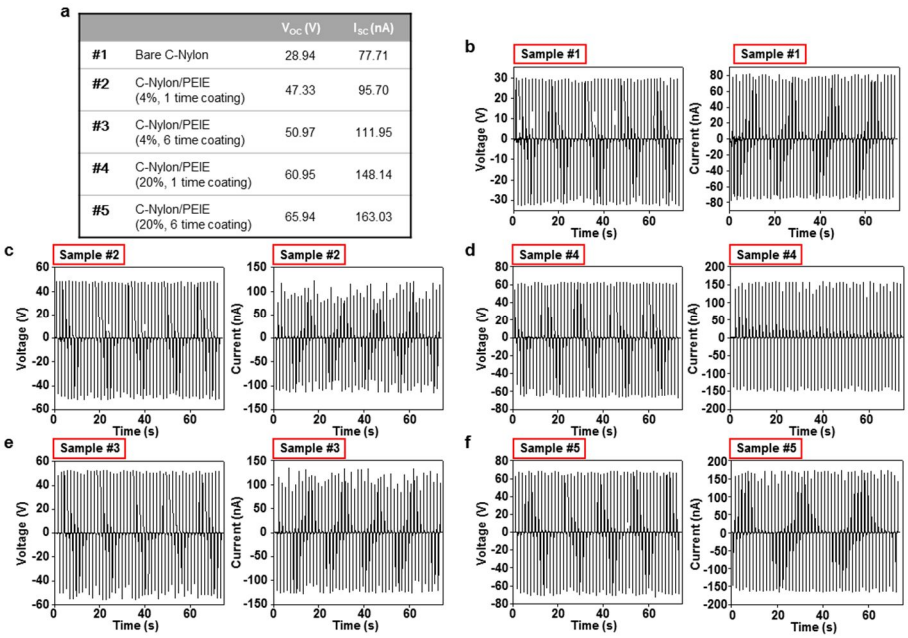

		V_{OC} (V)	I_{SC} (nA)
#1	Bare C-Nylon	28.94	77.71
#2	C-Nylon/PEIE (4%, 1 time coating)	47.33	95.70
#3	C-Nylon/PEIE (4%, 6 time coating)	50.97	111.95
#4	C-Nylon/PEIE (20%, 1 time coating)	60.95	148.14
#5	C-Nylon/PEIE (20%, 6 time coating)	65.94	163.03

Figure 4.6 Surface modification effect. a) The table of sample preparation conditions with power generation performance values. Open-circuit voltage (left) and short-circuit current (right) of b) sample #2, c) sample #3, d) sample #4 and f) sample #5.

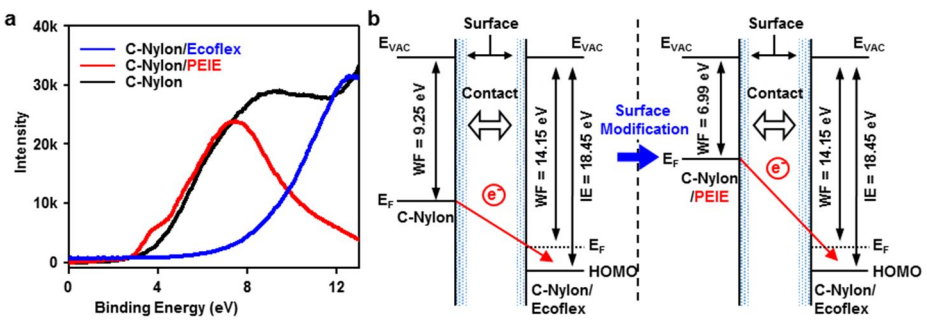

Figure 4.7 a) The Photoemission cutoff obtained via UPS for C-Nylon, C-Nylon/PEIE, and C-Nylon/Ecoflex. b) Corresponding, energy level diagram of

each samples.

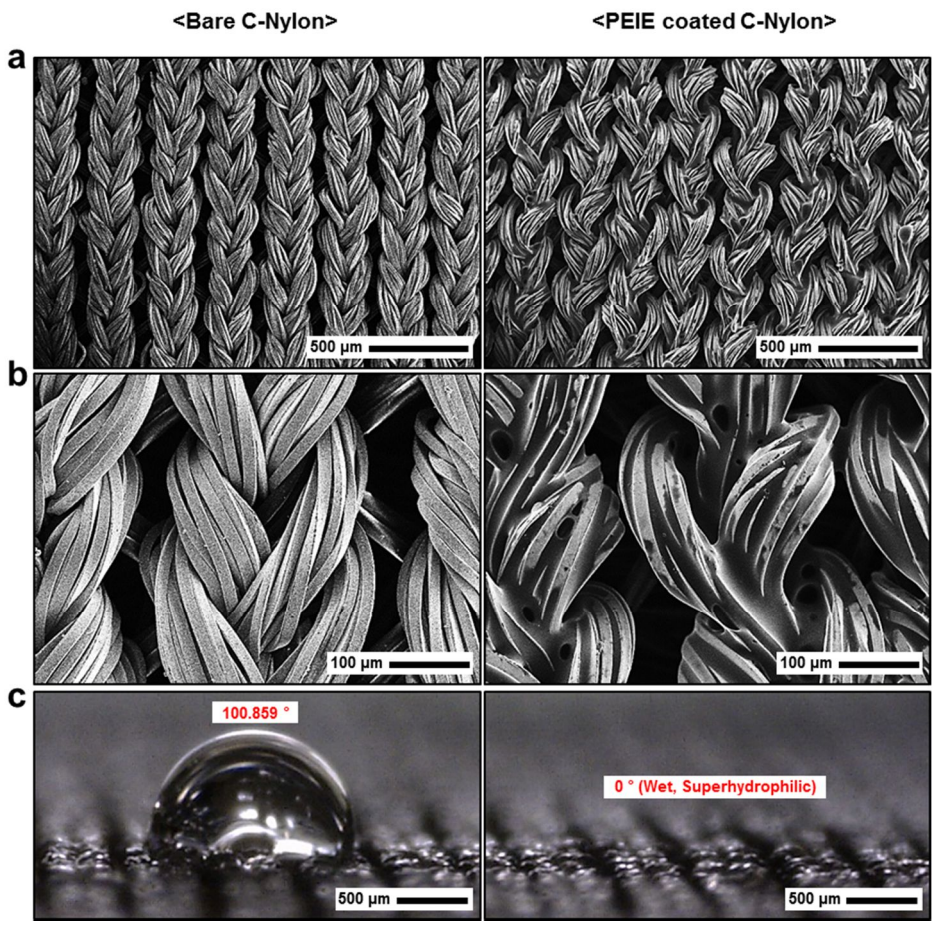

Figure 4.8 The comparison of the morphological difference between bare C-Nylon (left axis) and PEIE-coated C-Nylon (right axis) a) Low magnification SEM images b) and its expanded images. c) The surface energy difference is verified by the water contact angle test of bare C-Nylon (left) and PEIE modified C-Nylon (right).

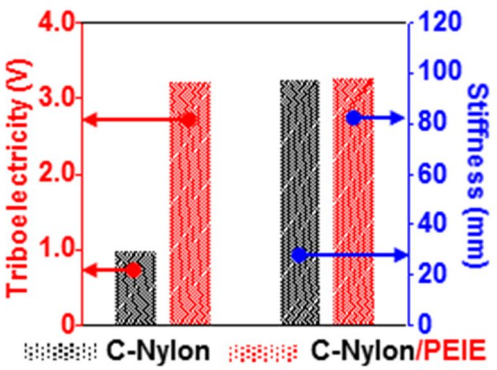

Figure 4.9 The electrical (left: triboelectricity) and mechanical (right: stiffness) property changes by PEIE modification are shown.

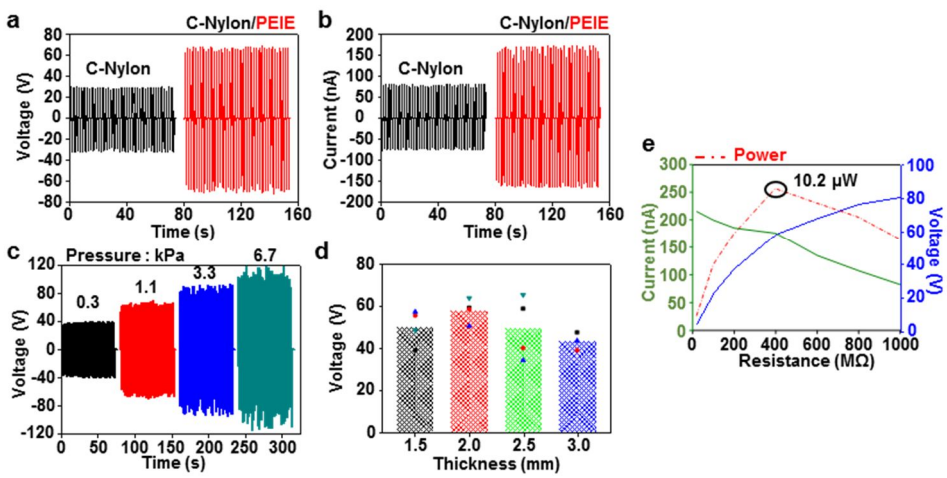

Figure 4.10 a) Open-circuit voltage and b) short-circuit current induced by contact/release of C-Nylon (left), C-Nylon/PEIE (right). c) Open-circuit voltage generated by different applied contact pressure (0.3 kPa, 1.1 kPa, 3.3 kPa, 6.7 kPa, respectively). d) Ecoflex thickness optimization. Ecoflex layer was coated on C-Nylon with varied thickness from 1.5 mm to 3.0 mm and its open-circuit voltage was expressed. e) Dependence of the I_{SC} (left axis) and V_{oc} (right axis) output on the external resistance. The results represent average value of electric signals and it indicating maximum power output was achieved when R = 400 M Ω.

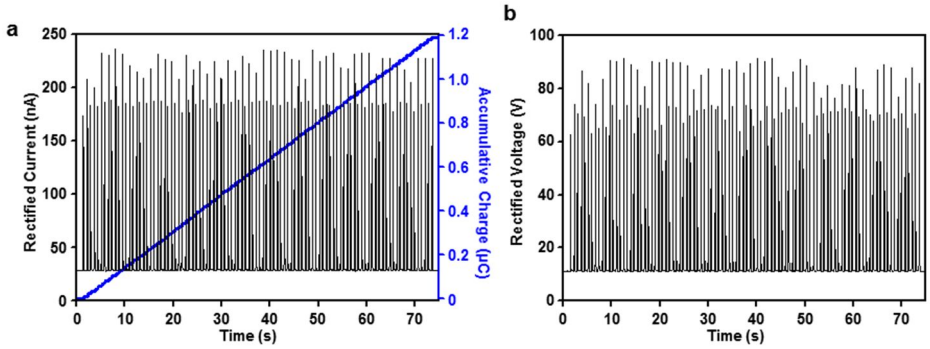

Figure 4.11 Rectified a) current, accumulative charge and b) voltage generated from the optimized sample (Ecoflex thickness: 2 mm, PEIE modification: 5times with 20 % solution.)

Figure 4.12 shows the working results of the wearable devices which are equipped on the body and clothes. The TEG generates the electricity through motions such as walking and running. As shown in Figure 4.12b, running makes higher and more frequent current peaks than walking. The generated electricity charges the integrated battery which is connected with TEG by conductive thread and extends the plateau region of the battery (Figure 4.12c), which is an indication of longer battery life. Energy supplied from the wearable battery runs the sensor (accelerometer) and wireless unit. The accelerometer detects moving directions by differentiating x, y, and z components (Figure 4.13).

In the demonstration shown in the cartoon, the wearable fall detecting system tells the difference between various motions (sit-down, stand-up, walk, step-up/down, run, and fall; Figure 4.14a). As the motion is more active, the signal intensity increases. A fall shows the largest signal peak-to-peak amplitude. Repeated measurements show similar patterns discriminating different motions (Figure 4.15). The sensing data is processed in MCU for the in situ transmission of data to external devices wirelessly via the Bluetooth module. In contrast to other motions, the fall has a distinctive signal pattern; i.e., a free fall (slightly increased signal), hitting the ground (large impact signal), and then no motion (flat, motionless signal) as shown in Figure 4.14b. By detecting this characteristic pattern, the custom-made software/algorithm recognizes the fall (Figures 4.14c and 4.16) and the external device sends alerting email to the emergency medical facility (Figure 4.14d).

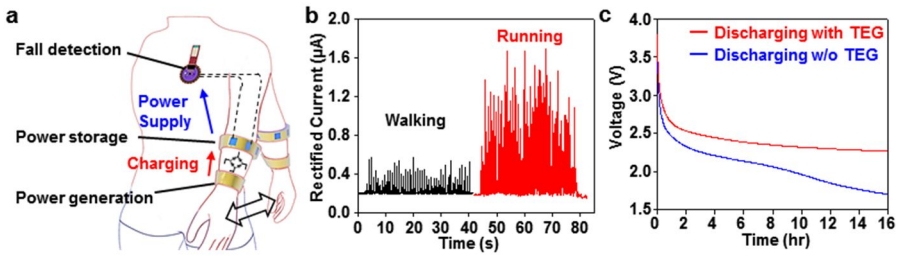

Figure 4.12 a) Schematic descriptions of the wearable fall detection system. b) The electric power generation by TEG from the living activities (walking, running) c) The discharge process of charged battery with and without operation of TEG.

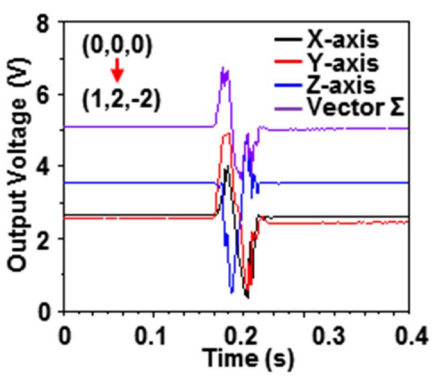

Figure 4.13 The representative moving direction of the 3-axis accelerometer (left), and its temporal response (black : x-axis, red : y-axis, blue : z-axis, pink : (vector sum)).

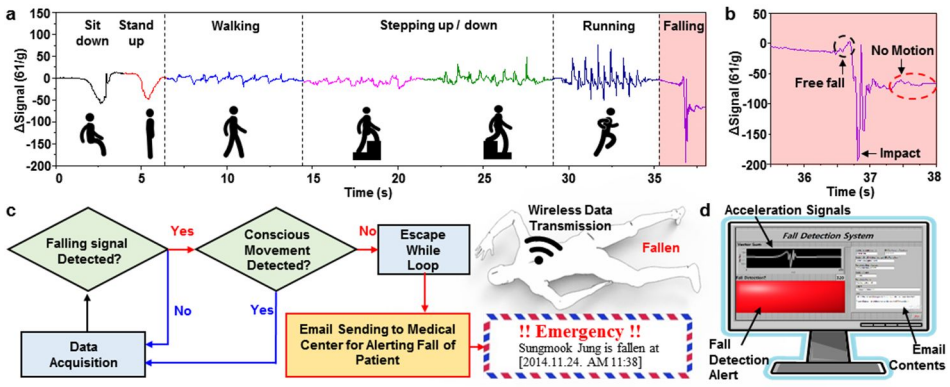

Figure 4.14 a) The temporal change of vector sum during various motion of the subject. b) Enlarged view of the vector sum during fall; three main indicators of fall are freefall signal, subsequent impact signal and certain period of movelessness after impact. c) A flow chart of the fall detection system. It includes algorithm of event monitoring and alerting via email in case of fall detection. Inset shows the illustration of fallen wearer. d) A front panel of fall detection program. It includes a graph indicator for plotting wirelessly transmitted signal of the accelerometer, a LED for fall detection alert, and user interface for modifying email contents.

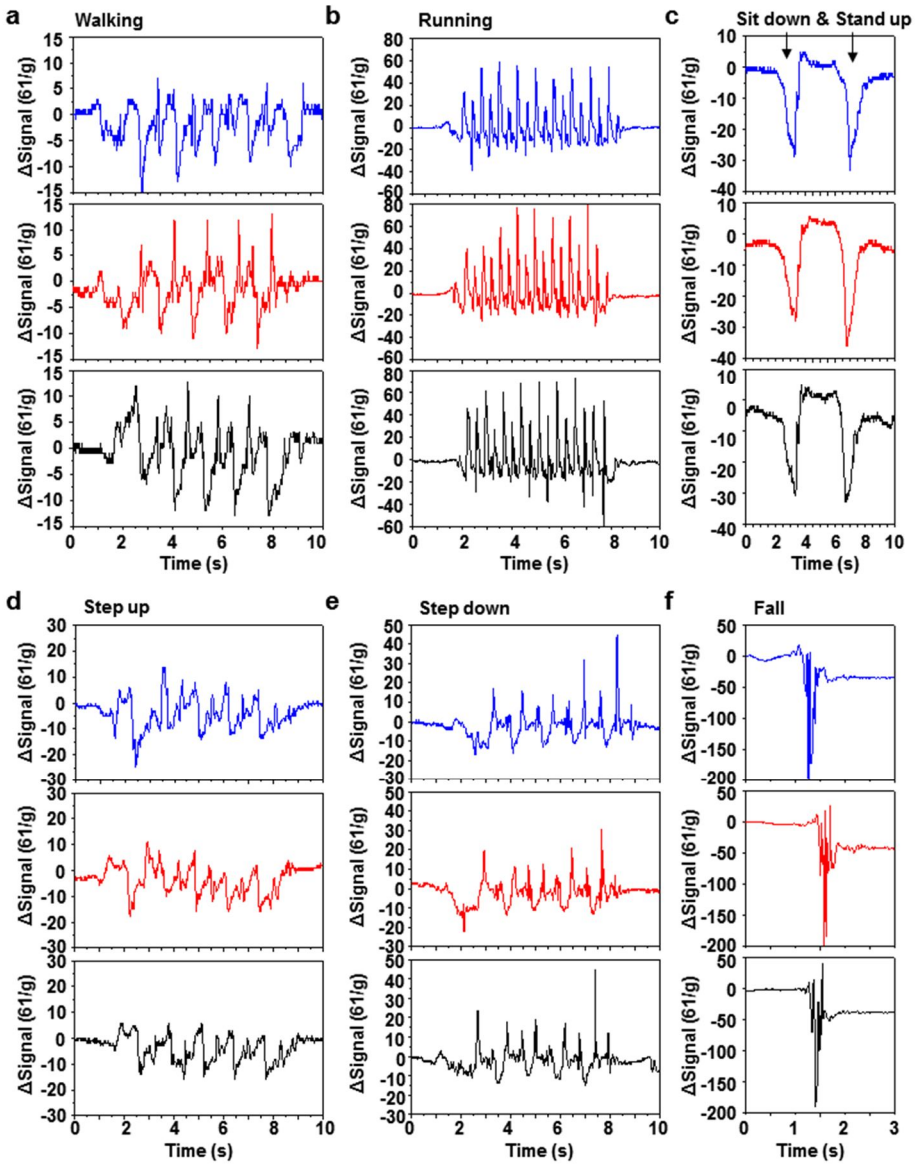

Figure 4.15 The vector sum acquired by three different experiments (blue, red, black graphs) in case of a) walking, b) running, c) sitting up/down, d) stepping up the stair, e) stepping down the stair, and f) falling.

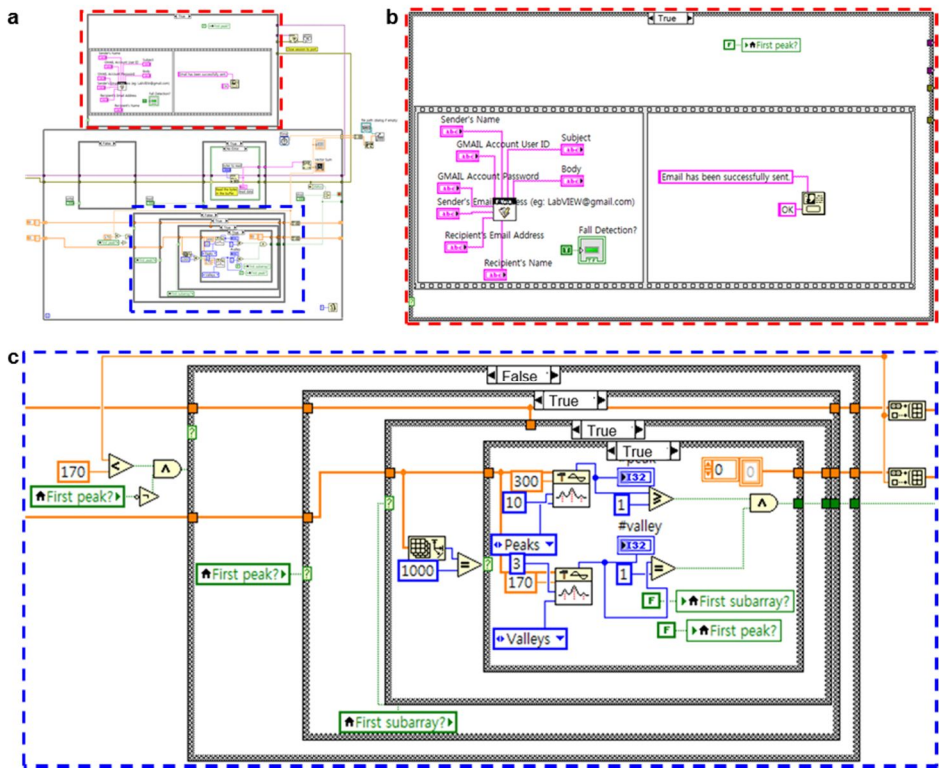

Figure 4.16 a) A part of program code including algorithm for email sending (red dotted box) and fall detection (blue dotted box). b) Enlarged view of the code for email sending. c) Enlarged view of the code for fall detection

4.4 Conclusion

In summary, stretchable TEGs and commercial micro batteries integrated with acceleration sensors and wireless communication units are developed for the wearable fall detection system. The energy devices share stretchable conductive substrates (C-Nylon) modified for purposes of device components. Modified C-Nylons are easily integrated on commercial fabrics by using conductive threads. Stretchable characteristics provide the extreme comfort to the user. Soft, wearable and light-weight power supply system maximizes the mobility of wearers. With these wearable energy devices, the fall detection system monitors the subject's condition in the extended period of time. The current wearable power supply devices opens opportunities to be integrated with other kinds of high performance devices for novel wearable electronics.

References

[1] J.-W. Jeong, W.-H. Yeo, A. Akhtar, J.J.S. Norton, Y.-J. Kwack, S. Li, S.-Y. Jung, Y. Su, W. Lee, J. Xia, H. Cheng, Y. Huang, W.-S. Choi, T. Bretl, J.A. Rogers, *Adv. Mater.* **2013**, 25, 6839.

[2] S. Jung, J.H. Kim, J. Kim, S. Choi, J. Lee, I. Park, T. Hyeon , D.-H. Kim, *Adv. Mater.* **2014**, 26, 4825.

[3] S. Lim, D. Son, J. Kim, Y.B. Lee, J.-K. Song, S. Choi, D.J. Lee, J.H. Kim, M. Lee, T. Hyeon, D.-H. Kim, *Adv. Funct. Mater*. **2014**, DOI: 10.1002/adfm.201402987

[4] L. Gao, Y. Zhang, V. Malyarchuk, L. Jia, K.-I. Jang, R.C. Webb, H. Fu, Y. Shi, G. Zhou, L. Shi, D. Shah, X. Huang, B. Xu, C. Yu, Y. Huang, J.A. Rogers, *Nat. Commun.* **2014**, 5, 4938.

[5] W. H. Yeo, Y. S. Kim, J. Lee, A. Ameen, L. Shi, M. Li, S. Wang, R. Ma, S. H. Jin, Z. Kang, Y. Huang, J. A. Rogers, *Adv. Mater.* **2013**, 25, 2773.

[6] M. Kaltenbrunner, T. Sekitani, J. Reeder, T. Yokota, K. Kuribara, T. Tokuhara, M. Drack, R. Schwodiauer, I. Graz, S. Bauer-Gogonea, S. Bauer, T. Someya, *Nature* **2013**, 499, 458.

[7] H. Fuketa, K. Yoshioka, Y. Shinozuka, K. Ishida, T. Yokota, N. Matsuhisa, Y. Inoue, M. Sekino, T. Sekitani, M. Takamiya, T. Someya, T. Sakurai, *IEEE ISSCC*, **2013**, DOI: 10.1109/ISSCC.2013.6487656

[8] D. Son, J. Lee, S. Qiao, R. Ghaffari, J. kim, J. E Lee, C. Song, S. J. Kim, D. J. Lee, S. W. Jun, S. Yang, M. Park, J. Shin, K Do, M. Lee, K. Kang, C. S. Hwang, N. Lu, T. Hyeon, D.-H Kim, *Nat. Nanotech.* **2014**, 9, 397.

[9] G. Schwartz, B.C.-K. Tee, J. Mei, A. L. Appleton, D.H. Kim, H. Wang, Z. Bao, *Nat. Commun.* **2013**, 4, 1859.

[10] K. Takei, T. Takahashi, J.C. Ho, H. Ko, A.G. Gillies, P.W. Leu, R.S. Fearing, A. Javey, *Nat. Mater.* **2010**, 9, 821.

[11] J. Kim, M. Lee, H.J. Shim, R. Ghaffari, H.R. Cho, D. Son, Y.H. Jung, M. Soh, C. Choi, S. Jung, K.Chu, D. Jeon, S.-T. Lee, J.H. Kim, S.H Choi, T. Hyeon, D.-H. Kim, *Nat. Commun.* **2014**, 5, 5747.

[12] S. Xu, Y. Zhang, L. Jia, K.E. Mathewson, K.-I. Jang, J. Kim, H. Fu, X. Huang, P. Chava, R. Wang, S. Bhole, L. Wang, Y.J. Na, Y. Guan, M. Flavin, Z. Han, Y. Huang, J.A. Rogers, *Science* **2014**, 344, 70

[13] M. Drack, I. Graz, T. Sekitani, T. Someya, M. Kaltenbrunner, S. Bauer, *Adv. Mater.* **2014**, DOI: 10.1002/adma.201403093

[14] X. Xue, P. Deng, B. He, Y. Nie, L. Xing, Y. Zhang, Z. L. Wang, Adv Energy Mat 2014, 4, 1301329.

[15] J. M. Donelan, Q. Li, V. Naing, J. A. Hoffer, D. J. Weber, A. D. Kuo, Science 2008, 319, 807.

[16] C. Zhang, W. Tang, C. Han, F. Fan, Z.L. Wang, Adv Mat 2014, 26, 3580.

[17] S. Wang, Z.-H. Lin, S. Niu, L. Lin, Y. Xie, K. C. Pradel, Z. L. Wang, ACS Nano 2013, 7, 11263.

[18] H. Zhang, Y. Yang, T-C. Hou, Y. Su, C. Hu, Z.L. Wang, Nano energy 2013, 2, 1019

[19] J. Lowell, A.C. Rose-Innes, Adv. Phys., **1980**, 29, 947-1023.

[20] Y. Zhou, C. Fuentes-Hernandez, J. Shim, J. Meyer, A.J. Giordano, H. Li, P. Winget, T. Papadopoulos, H. Cheun, J. Kim, M. Fenoll, A. Dindar, W. Haske, E. Najafabadi, T.M. Khan, H. Sojoudi, S. Barlow, S. Graham, J.-L. Brédas, S.R. Marder, A. Kahn, B. Kippelen, *Science*, **2012**, 336, 327.

[21] The triboelectricity was measured by followed the Korea standard test procedure (KSK 0555). C-Nylon and C-Nylon/PEIE were rubbed with wool, and their surface voltage was measured.

[22] The stiffness was measured by followed the Korea standard test procedure (heart loop test procedure, KSK 0538)

요약 (국문초록)

사람동작 감지기들과 마찰전기 발전기를 통합해 구현한 입을 수 있는 전자기기 시스템

최근 기존의 딱딱한 디바이스를 부드럽게 만들어 사람 몸에 부착한 상태로 사용하고자 하는 연구가 각광을 받고 있다. 의료 목적으로 사용될 수도 있고, 운동을 돕는다거나 외부 기기 조종기로 사용될 수 있는 이 입을 수 있는 디바이스를 통해 사람들은 더욱 나은 삶을 만들 수 있기를 기대한다. 그러기 위해서는 3가지 기술적인 요소들이 해결되어야 한다. 이 디바이스는 신축성이 있어 입은 사람이 크게 불편함을 느끼지 않아야 하며, 스마트하여 다양한 신호들을 자동으로 감지하여 외부 기기와 정보를 주고 받아야 한다. 마지막으로 항상 작동 되어야 하는 기기이므로 오랜 시간 동작하는 게 중요하다. 하지만 입어야 한다는 제약 때문에 배터리의 부피 또한 작을 수 밖에 없어서 문제점으로 지적되어 왔다. 이 학위 논문에서는 이러한 문제점들을 해결하고자 생활을 하며 발생되고 낭비되는 마찰력을 이용하여 전기를 발전하고 배터리에 충전하였다. 또한 이렇게 충전된 전기가 피부에 부착 할 수 있는 센서들을 구동시키는데 사용할 수 있음을 증명하기 위해 우리는 에너지 장치와 웨어러블

센서들이 통합된 시스템을 구현하고자 하였다.

이 시스템은 늘어나는 에너지 제공 장치들(트라이보 일렉트릭 제너레이터 그리고 슈퍼캐퍼시터 혹은 리튬 이온 배터리)과 연결된 센서들, 무선 통신 유닛 그리고 기타 전자 기기들(가속도 센서, 블루투스 모듈, 마이크로 콘트롤러)로 이뤄져 있다. 모든 기기들은 몸 위에 착용되어나 옷 위에 실로 꿰매어 부착되어 있고 각 기기들은 모두 전도성 실로 연결되어 있다. 걷거나 뛸 때 흔드는 팔의 움직임이 트라이보 일렉트로 제너레이터를 동작시켜 마찰을 전기로 바꾸게 되고 이 전기는 에너지 저장장치에 충전된다. 충전된 전기는 압력 감지 센서나 낙상 감지 센서 그리고 기타 전자 기기들에 공급이 된다. 압력 감지 센서는 사람의 의식적인 신호인 특정 버튼을 누르는 것을 감지할 수 있어 휴먼-머신 인터페이스로 사용되었다. 낙상 감지 센서는 사람의 낙상 사고로 인한 응급 상황을 감지하여 자동으로 병원에 응급 요청을 보내는데 사용되었다. 여기서 만든 압력 감지 센서와 전기 발전 장치들은 모두 천을 기반으로 한 기기로, 플렉서블하거나 스트레쳐블하며 옷과 비슷한 기계적 성질을 갖고 있어 손쉽게 옷에 부착하거나 몸 위에 입은 상태로 사용할 수 있었다.

주요어: 입을 수 있는 전자기기, 압력 감지 고무, 트라이보 제너레이터, 휴먼-머신 인터페이스, 유비쿼터스

학번: 2010-31328